Project THEMIS
Technical Report No. 8

AIR FLOW OVER ROUGHNESS DISCONTINUITY

by

Fei-Fan Yeh

and

E. C. Nickerson

Prepared Under
Office of Naval Research
Contract No. N00014-68-A-0493-0001
Project No. NR 062-414/6-6-68(Code 438)
U.S. Department of Defense
Washington, D. C.

Fluid Dynamics and Diffusion Laboratory
College of Engineering
Colorado State University
Fort Collins, Colorado

July 1970

CER70-71FFY-ECN6

ABSTRACT

AIR FLOW OVER ROUGHNESS DISCONTINUITY

Measurements of mean velocity, mean-square turbulent velocity, turbulent shear stress, one-dimensional spectrum, and mass concentration distributions following a step increase in surface roughness of a wind-tunnel boundary-layer flow are presented. The mean velocity distributions agree well with Nickerson's (1968) numerical calculations for a small roughness change. The mixing-length distribution in the "transitory" region is not experimentally consistent with that established for fully-developed turbulent boundary layer. Turbulent intensity and shear stress are generated progressively towards the upper layer as one moves downstream from the roughness discontinuity. The high frequency end of the spectra in the "transitory" region can be exactly represented by the high frequency shape of the undisturbed turbulent boundary layer. Self-preserving mass concentration profiles are in general possible for both the vertical and horizontal distributions. The adjustment of the mean motion to the roughness change is more rapid than that of the turbulence.

TABLE OF CONTENTS

Chapter		Page
	LIST OF TABLES	v
	LIST OF FIGURES	vi
	LIST OF SYMBOLS	ix
I	INTRODUCTION	1
II	THEORETICAL AND EXPERIMENTAL BACKGROUND	3
	2.1 Statement of the Problem	3
	2.1.1 Basic equations	3
	2.1.2 Possibility of wall variable similarity.	6
	2.1.3 The effect of roughness change on turbulence	8
	2.2 Literature Review	10
	2.2.1 Clauser's qualitative argument	10
	2.2.2 Theories of internal boundary layer	11
	2.2.3 Numerical simulation	16
	2.2.4 Laboratory simulations and field observations	19
	2.2.5 Review of the related diffusion studies.	20
III	EXPERIMENTAL EQUIPMENT AND MEASUREMENT PROCEDURE	23
	3.1 Wind Tunnel and Equipments for the Flow Setup	23
	3.2 Measurements of Mean Velocity and Pressure Gradient.	25
	3.3 Measurements of Turbulence	26
	3.3.1 Hot-wire anemometer and associated instrumentations	26
	3.3.2 Calculations of turbulent intensities and shear stress	28
	3.4 Measurements of Mass Concentration	30
IV	RESULTS AND DISSCUSSION	32
	4.1 Description of the Results	33
	4.1.1 Mean velocity distributions and streamlines	33
	4.1.2 Mean velocity structure of internal boundary layer	35
	4.1.3 Turbulent results.	40
	4.1.4 Momentum transfer.	44
	4.1.5 Mass diffusion results	46

TABLE OF CONTENTS - Continued

Chapter		Page
	4.2 Application of Results to Theoretical Models	49
	4.2.1 Development of internal boundary layer.	49
	4.2.2 Mean velocity distributions compared with Nickerson's model	52
V	CONCLUSIONS	54
	5.1 Mean Velocity Field	54
	5.2 Turbulence Field	55
	5.3 Mass Transfer	55
	REFERENCES	57
	APPENDIX I	62
	APPENDIX II - Tables	66
	APPENDIX III - Figures	81

LIST OF TABLES

Table		Page
I	Mean Velocity Data for Case I	67
II	Mean Velocity Data for Case II.	68
III	Mean Velocity Data for Case III	69
IV	δ, δ^*, θ, U_* and z_o for All Cases.	70
V	(a) $\overline{u^2}$, $\overline{w^2}$ and $-\overline{uw}$ Data for Case I.	71
	(b) $\overline{v^2}$ Data for Case I.	72
	(c) $-\overline{uw}$ Data for Case II.	72
VI	Data on One-Dimensional Spectra for Case I	73
VII	Parameters Used in Spectral Calculations for Case I . .	77
VIII	Mass Diffusion Data for Case I.	78

LIST OF FIGURES

Figure		Page
1	Coordinate system and flow features	82
2	Plan view of wind tunnel	83
3	Flat plate and pressure taps	84
4	Non-dimensional plot of wall pressure distributions on the flat plate	85
5	Mean velocity distributions at x = 3 ft to check the two-dimensionality of the flow	86
6	$\overline{u}^2$ distributions at x = 3 ft to check the two-dimensionality of the flow	87
7	Test section geometry	88
8	False wind tunnel ceiling to obtain zero pressure gradient over flat plate	89
9	Non-dimensional plot of static pressure distribution at the free stream along the flat plate (p_{ref} = wall pressure at x = - 3 ft)	90
10	Comparison of mean velocity distributions measured by the hot wire and the pitot tube at x = 2 in.	91
11	Block diagram for turbulence measurements	92
12	Coordinates of the single and the crossed hot wires	93
13	Mean velocity, streamline and $-\overline{uw}$ distributions in the x-z plane for Case I	94
14	Mean velocity and streamline distributions in the x-z plane for Cases II and III	95
15	Longitudinal velocity distributions for Case I	96
16	Longitudinal velocity distributions for Case II	97
17	Longitudinal velocity distributions for Case III	98

LIST OF FIGURES - Continued

Figure		Page
18	A semi-log plot of non-dimensional velocity distributions for Case I	99
19	Shear velocity distributions for Case I	100
20	U/U_* vs. $\log_{10}\left(\frac{zU_*}{\nu}\right)$ for Case I	101
21	Karman constant and wall pressure measurements for Case I.	102
22	Karman constant and wall pressure measurements for Case II	103
23	$\overline{u^2}$, $\overline{v^2}$, and $\overline{w^2}$ distributions for Case I	104
24	Normalized spectra of longitudinal velocity fluctuations at x = - 12 in. for Case I	105
25	Normalized spectra of longitudinal velocity fluctuations at x = 4 in. for Case I	106
26	Normalized spectra of longitudinal velocity fluctuations at x = 6 in. for Case I	107
27	Normalized spectra of longitudinal velocity fluctuations at x = 12 in. for Case I	108
28	u'-spectra in the similarity coordinates at x = - 12 in. for Case I	109
29	u'-spectra in the similarity coordinates at x = 4 in. for Case I	110
30	u'-spectra in the similarity coordinates at x = 6 in. for Case I	111
31	u'-spectra in the similarity coordinates at x = 12 in. for Case I.	112
32	Distributions of the vertical turbulent diffusivity for Case I	113
33	Distributions of the mixing length for Case I	114
34	Distributions of $a_1 = \frac{\tau}{\rho\overline{q}^2}$ at x = 4 in. and x = 6 in. for Case I.	115

LIST OF FIGURES - Continued

Figure		Page
35	Non-dimensional distributions of $L = \frac{(\tau/\rho)^{3/2}}{\xi}$ at x = 4 in. and x = 6 in. for Case I	116
36	Non-dimensional distributions of $L_\xi = \frac{(\overline{q^2})^{3/2}}{\xi}$ at x = 4 in. and x = 6 in. for Case I	117
37	Typical profiles of the vertical mass concentration for Case I	118
38	Typical profiles of the horizontal mass concentration for Case I	119
39	Non-dimensional plot of the vertical concentration profiles	120
40	Non-dimensional plot of the horizontal concentration profiles	121
41	Decrease of C_{max} with x for Case I	122
42	Growth of λ and η with x for Case I	123
43	Growth of the surface of the internal boundary layer, compared with that of the critical surface	124
44	Non-dimensional plot of the velocity defect law for Case I.	125
45	Mean velocity distributions for Case I compared with Nickerson's model	126
46	Mean velocity distributions for Case II compared with Nickerson's model	127
47	Mean velocity distributions for Case III compared with Nickerson's model	128

LIST OF SELECTED SYMBOLS

Symbol	Definition	Dimension
A_1, A_2, A_3, A_z	Constant	---
A(z)	Change of velocity due to the flow acceleration	LT^{-1}
a	Constant	---
a_1	Empirical function as defined in Eq. (2-32)	---
B_1, B_2	Constant	---
b	Constant	---
C	Mass concentration	ppm
C_{max}	Maximum mass concentration	ppm
c	Constant	---
D_{ij}	Eddy diffusivity tensor	L^2T^{-1}
D_x, D_y, D_z	Eddy diffusivities in x,y,z directions	L^2T^{-1}
d(x)	Thickness of the internal boundary layer	L
E_1, E_2, E_3	Mean voltage output across the hot wire	L
E(k)	Three-dimensional energy spectrum function	L^3T^{-1}
e_1, e_2, e_3	Fluctuating voltage across the hot wire	L
$F(k_1)$	One-dimensional spectrum function	L^3T^{-1}
$F(\frac{z}{d})$, $f(\frac{z}{d})$	Universal function	---
f	Frequency	T^{-1}
G	Empirical function as defined in Eq. (2-34)	---
H	Ratio of δ^+ to θ	---

LIST OF SELECTED SYMBOLS - Continued

Symbol	Definition	Dimension
$I(t)$	An impulse input function	---
K	Kármán Constant	---
k	Three-dimensional wave number	L^{-1}
k_1	One-dimensional wave number	L^{-1}
k_s	Kolmogorov's wave number	L^{-1}
k_*	A roughness characteristic length	L
L	Stability length, also defined as in eq. (2-33)	L
ℓ_x, ℓ_y, ℓ_z	Mixing-length components in x,y,z directions	L
M	Nondimensional function	---
m	Constant	---
N	Nondimensional function	---
n	Constant	---
p	Mean pressure	$ML^{-1}T^{-2}$
p_{ref}	Reference pressure	$ML^{-1}T^{-2}$
Q_{cp}	Strength of a continuous point source	ML^{-3}
$\frac{\overline{q_2}}{2}$	Total turbulent kinetic energy per unit mass	L^2T^{-2}
R_{ij}	Velocity correlation function	L^2T^{-2}
t	Time	T
U,V,W	Mean velocity components in x,y,z directions	LT^{-1}
U_∞	Free-stream velocity	LT^{-1}
U_*	Shear velocity	LT^{-1}
U_{*_o}	Shear velocity downwind of the roughness discontinuity	LT^{-1}

LIST OF SELECTED SYMBOLS - Continued

Symbol	Definition	Dimension
U_{*1}	Shear velocity upwind of the roughness discontinuity	LT^{-1}
u,v,w	Velocity fluctuations in x,y,z directions	LT^{-1}
x,y,z	Distance along longitudinal, lateral and vertical direction	L
x_s	Coordinate of x axis of the diffusion source	L
Z_1, Z_2	Heights	L
z_o	Roughness length downwind of the roughness discontinuity	L
z_1	Roughness length upwind of the roughness discontinuity	L
α	Constant	---
$\alpha(\frac{z}{L})$	A dimensionless function	---
β	Angle of velocity vector	---
γ	Exponential constant	---
δ	Boundary layer thickness	L
δ^*	Displacement thickness	L
δ^+	A characteristic thickness	L
$\delta(z)$	Change of velocity due to the streamline displacement	LT^{-1}
ε	Angle deviation of hot wire	---
ξ	Turbulent energy dissipation	L^2T^{-3}
θ	Momentum thickness	L
θ_1, θ_2	Angle of hot wire to velocity vector	---
$\eta(x)$	One-half of the plume-spreading width, at which the local mass concentration is one-half of the value at ground level	L

LIST OF SELECTED SYMBOLS - Continued

Symbol	Definition	Dimension
$\lambda(x)$	Height at which the local mass concentration is one-half of the value at ground level	L
ν	Coefficient of dynamic viscosity	L^2T^{-1}
ρ	Mean mass density of the air	ML^{-3}
σ_{ij}	Mass diffusivity tensor	L^2T^{-1}
$\sigma_{xx},\sigma_{yy},\sigma_{zz}$	Mass diffusivity in x,y,z direction	L^2T^{-1}
τ	Shear stress	$ML^{-1}T^{-2}$
τ_w	Wall shear stress	$ML^{-1}T^{-2}$
τ_{max}	Maximum shear stress	$ML^{-1}T^{-2}$
ϕ_{ij}	Energy spectrum function	L^3T^{-2}
ψ	Dimensional stream function	L^2T^{-1}

Chapter I

INTRODUCTION

The surface layer in the lower 1000 meters of the atmosphere over a homogeneous terrain has been extensively investigated and successfully simulated by the boundary layer along a flat plate in wind tunnels. In reality, however, homogeneous terrain exists only over a limited area. Very little is known about the effect of surface non-homogeneity on boundary layer flows, and neither wind-tunnel data nor field data are available in sufficient quantity to deduce a general analytical model.

The effect of an abrupt increase in surface roughness is felt in the turbulent wind field downstream in two ways: a modified mean flow pattern develops according to the theory of the internal boundary layer (Elliott, 1958) and a "disturbed" turbulence mechanism is set into action which later is responsible for returning the flow to another relaxed state. Therefore, the existing semi-empirical models based on the present knowledge of so-called "pure" turbulence in calculating the mean flow distribution are highly questionable. Among many of the theoretical investigators the self-preservation approach of Townsend (1965a, 1965b, 1966) is certainly useful but still requires some assumptions about the interaction between the velocity field and the turbulent motion, in order to give quantitative results. The main requirement at this stage would appear to be an accurate and comprehensive experimental study of these flows which will perhaps throw further light on the mechanism involved.

In short, the principal aims of the present work were:

(1) to investigate systematically the mean flow field upstream and downstream from the roughness discontinuity and to compare the existing theories with the experiments;

(2) to study the turbulence structure of the internal boundary layer by means of extensive hot-wire surveys, and

(3) to measure the spread of diffusing matter and compare the spread rate with that obtained in a fully developed boundary layer over homogeneous terrain, since the effect of roughness discontinuity could cause significant difference in the convective force of the mean motion and the rate of eddy flux.

And finally, the suggested means of improving existing theories will be outlined.

It is also felt that the present investigation might, enhance the understanding of general boundary layer turbulence, since the turbulence mechanism could only be closely observed when its asymptotic state is perturbed (Clauser, 1956).

Chapter II

THEORETICAL AND EXPERIMENTAL BACKGROUND

The historical development of the calculation of internal boundary layers is characterized by the fact that the system of equations governing turbulent flow is not closed. Thus, solutions to the problem can only be obtained with the aid of empirical and hypothetical relationships. Since the results established to date are not fully satisfactory, many different approaches to the problem have been advanced. In this chapter, a comprehensive discussion of this problem in connection with the present experiment will be stated, and a summary of existing theoretical models, as well as most of the related measurements, will be given.

2.1 Statement of the Problem

2.1.1 Basic equations - Let us consider a steady, two-dimensional, turbulent boundary layer in neutral hydrostatic stability. Only the case of the flow moving from the aerodynamically smooth to the aerodynamically rough with negligible pressure gradient outside of the layer is treated. All the physical interpretations of the results should also be applicable to flows for which the aerodynamic roughness changes from rough to smooth.

As an introduction to the more general problem, the roughness is homogeneously distributed over the rough surface, but the corresponding roughness length z_o is not necessarily small in comparison with the boundary layer thickness is extremely large compared with the step change in the characteristic roughness dimension, i.e., the condition

$$z_o \ll \delta \qquad (2\text{-}1)$$

is not necessarily satisfied. Such a condition would possibly be satisfied in the atmospheric boundary layer for small roughness heights, but would be extremely unfeasible in the laboratory for perhaps an immeasurable change in roughness.

The approaching turbulent boundary layer over the smooth surface is assumed to be fully developed so that a universal quasi-stationary state is reached and certain similarity profiles are attained. The step increase of surface roughness will serve to perturb this asymptotic state, and as this results, the flow in the region immediately downstream (and very likely upstream) of the roughness discontinuity will be in a "transitory" state before relaxing to a new asymptotic state. The present investigation will concentrate on the development of the turbulent boundary layer in this "transitory" region.

A Cartesian coordinate system (Fig. 1) is used in which U,V,W denote the components of the mean velocity, and u,v,w the corresponding fluctuations in x,y,z directions. The Navier-Stokes equations in the x-z plane, after averaging in the y direction, reduce to

$$U \frac{\partial U}{\partial x} + W \frac{\partial U}{\partial z} + \frac{\partial \overline{u^2}}{\partial x} + \frac{\partial \overline{uw}}{\partial z} = - \frac{1}{\rho} \frac{\partial p}{\partial x} + \nu \left(\frac{\partial^2 U}{\partial x^2} + \frac{\partial^2 U}{\partial z^2} \right) \tag{2-2}$$

$$U \frac{\partial W}{\partial x} + W \frac{\partial W}{\partial x} + \frac{\partial \overline{uw}}{\partial x} + \frac{\partial w^2}{\partial z} = - \frac{1}{\rho} \frac{\partial p}{\partial z} + \nu \left(\frac{\partial^2 W}{\partial x^2} + \frac{\partial^2 W}{\partial z^2} \right) - g \quad , \tag{2-3}$$

in which the ordinary viscous terms are negligible in comparison with the eddy stress terms except in the wall region. Together with the continuity equation

$$\frac{\partial U}{\partial x} + \frac{\partial W}{\partial z} = 0 \tag{2-4}$$

they form the basic system of equations that must be solved. The closure of the system of equations in solving for U,W, and p requires that all the statistical quantities of turbulence be specified. The boundary conditions to which this system is subjected can be readily prescribed in the usual sense of boundary layer calculations.

A closure of the system of equations in the light of analogy with "mixing-length" hypothesis can be formulated, if it is assumed that the components of turbulent flux tensor relative to the axes oxyz are related in a simple homogeneous linear fashion to the gradient of mean velocity vector, i.e.,

$$-\overline{u_i u_j} = (D_T)_{ij}\left[\frac{\partial U_i}{\partial x_j} + \frac{\partial U_j}{\partial x_i}\right] \tag{2-5}$$

in which the second order tensor $(D_T)_{ij}$ is, in general, a function of position (not of time) since the relation between $-\overline{u_i u_j}$ and $\left[\frac{\partial U_i}{\partial x_j} + \frac{\partial U_j}{\partial x_i}\right]$ will be defined at every point of the flow field. Physically, $(D_T)_{ij}$ must be strictly a property of the turbulent motion, and we should not here complicate the analysis to discuss the fourth-order $(D_T)_{ij}$ as Hinze (1959) pointed out. For two-dimensional flow, Eq. (2-5) becomes

$$\begin{pmatrix} -\overline{u^2} & -\overline{uw} \\ -\overline{uw} & -\overline{w^2} \end{pmatrix} = \begin{pmatrix} D_{xx} & D_{xz} \\ D_{zx} & D_{zz} \end{pmatrix} \begin{pmatrix} 2\frac{\partial U}{\partial x} & \frac{\partial U}{\partial z} + \frac{\partial W}{\partial x} \\ \frac{\partial U}{\partial z} + \frac{\partial W}{\partial x} & 2\frac{\partial W}{\partial z} \end{pmatrix} \tag{2-6}$$

in which

$$\begin{pmatrix} D_{xx} & D_{xz} \\ D_{zx} & D_{zz} \end{pmatrix} = \begin{pmatrix} -\overline{u\ell}_x & -\overline{u\ell}_z \\ -\overline{w\ell}_x & -\overline{w\ell}_z \end{pmatrix} , \tag{2-7}$$

and, in turn, ℓ_x and ℓ_z are the components of a hypothetically vectorial mixing-length $\vec{\ell}$ in the x and z directions. Thus, the solution of the basic equations requires the information of three empirical problems; that is, certain factors must be found:

(1) Whether or not w is of the same order of magnitude as u, such that $|-\overline{w\ell}_x| = \text{const} \times |-\overline{u\ell}_x|$ and $|-\overline{w\ell}_z| = \text{const} \times |-\overline{u\ell}_z|$ can be used as in mixing-length theory.

(2) Whether or not the eddy coefficient $-\overline{u\ell}_z$, which governs the vertical mixing, can assume a functional form of the Wall law as a lower boundary condition in the "transitory region".

(3) Whether the order of magnitude of $-\overline{u\ell}_z$, which governs the horizontal mixing, can be estimated, as well as its role in solving the basic equations.

2.1.2 Possibility of wall variable similarity - Based on the above-mentioned resolution difficulties, the similarity arguments will naturally lead us to examine the experimental data in the context of the functional hypotheses of Clauser (1956) and Coles (1956).

Near the surface but outside the viscous sublayer, the only important length variable for the mean motion is the normal distance from the wall z, and the only important velocity scale is $U_* = (\tau_w/\rho)^{1/2}$, thus, immediately, by the dimensional argument,

$$\frac{\partial U}{\partial z} = \frac{U_*}{Kz} \tag{2-8}$$

in which K is the Karman's constant, known to be approximately 0.4 in the wall region of the fully developed turbulent boundary layer. Whether K should be a constant or not in the "transitory" region is not known.

However, it can easily be deduced that K will at least be a function of x by introducing the vertical mean velocity component $V(x)$ into the conventional Karman's similarity analysis, which was based on the assumption of a parallel flow (Schlichting, 1960), and

$$K = \text{constant} \left| \frac{\frac{dU}{dz}}{\frac{d^2W}{dx^2}} \right| \times \left| \frac{\frac{d^2U}{dz^2}}{\frac{dU}{dz}} \right| . \tag{2-9}$$

The derivation of this relation is shown in detail in Appendix I. Integration of (2-8) for a given x gives

$$\frac{U}{U_*} = \frac{1}{K} \ln \frac{z}{z_o} \tag{2-10}$$

in which z_o is the characteristic roughness length of the surface, introduced as the result of integration constant.

The wind profile expressed by Eq. (2-10) has received a great deal of experimental support, but only for flows over homogeneous surfaces. Here, we would expect that both the smooth and rough surfaces should correspondingly possess a horizontal uniform z_o except near the discontinuity. Physically, the z_o should be assumed to have a rapid change, but still in a certain continuous fashion over the step change of surface roughness. Thus, we have to obtain adequate knowledge concerning the functional form of the horizontal variation of z_o in order to justify the similarity law existing in the "transitory" region. In fact, the z_o could serve as another vital scaling parameter.

According to theoretical arguments (Rotta, 1962), the assumption of similarity of the wall flow is only justified, if it includes the turbulence terms. Hence, the application of the similarity relation to

double velocity correlation functions $R_{ij}(\vec{x},\vec{r},t)$ and spectrum functions $\phi_{ij}(\vec{x},k)$ in the direction of mean flow requires forms like

$$R_{ij}(\vec{x},\vec{r},t) = U_*^2 \, G_{ij}\left(\frac{zU_*}{\nu} \;,\; \frac{\vec{r}}{z} \;,\; \frac{tU_*}{z}\right) \tag{2-11}$$

$$\phi_{ij}(\vec{x},k) = U_*^2 \, z \, H_{ij}\left(\frac{zU_*}{\nu} \;,\; kz\right) \tag{2-12}$$

in which G_{ij} and H_{ij} are respectively dimensionless universal double velocity correlation functions and spectrum functions, and k is the wave number.

Though there exists experimental evidence for a subrange near the wall within which the one-dimensional spectrum function varies in accordance with a theoretical prediction by Tchen (1953), it is well-known--Townsend (1961) comments--that the turbulent motion does not scale on U_* and z, and it is difficult to reconcile the experimental observations without supposing that the motion at any point in the wall region consists of (i) an "active" part, which is responsible for turbulent transfer and determined by the stress distribution, and (ii) and "inactive" part determined by the turbulence in the outer layer. The effect of an "inactive" part is supported by measurements taken by Bradshaw (1967b) of frequency spectra in a strongly retarded boundary layer. A noticeable increase of dissipation of kinetic energy into heat supplied by turbulent diffusion from the outer layer was observed. Consequently, we might expect such an effect on the retarding fluid near the wall in the "transitory" region.

2.1.3 The effect of roughness change on turbulence - From the turbulence-energy equation (Hinze, 1959),

$$\frac{d}{dt}\left(\frac{\overline{q^2}}{2}\right) = -\overline{u_i u_j}\frac{\partial U_j}{\partial x_i} - \frac{\partial}{\partial x_i}\overline{u_i\left(\frac{p}{\rho} + \frac{q^2}{2}\right)} + \nu\frac{\partial}{\partial x_i}\overline{u_j\left(\frac{\partial u_i}{\partial x_j} + \frac{\partial u_j}{\partial x_i}\right)}$$

$$- \nu\overline{\left(\frac{\partial u_i}{\partial x_j} + \frac{\partial u_j}{\partial x_i}\right)\frac{\partial u_j}{\partial x_i}} \qquad (2\text{-}13)$$

rate of change of kinetic energy of turbulence = production + Convective Diffusion + Viscous Work + Dissipation

it is seen that, if all the terms but $\overline{u^2}\frac{\partial U}{\partial x}$ are kept unchanged, the total turbulent kinetic energy tends to be increased (at the expense of the mean flow energy), as soon as the velocity of a flow decreases (or is retarded) in the x direction, i.e., $\partial U/\partial x < 0$. Many theoretical workers, such as Townsend (1965a, 1965b, 1966) states that the effect of roughness change is initially restricted to an "internal boundary layer" with thickness $d(x)$. Far above $d(x)$, the streamline is displaced vertically without a charge in shape of the velocity profile. On these grounds, the following inferences may be drawn.

Upon encountering the rough surface, the fluid near the wall is retarded by the increased wall shear stress. In accordance with the continuity equation, a vertical mean velocity is created to convect the lower momentum fluid away from the wall. Since the fluid far above the $d(x)$ is not affected, the fluid at the height of order of $d(x)$ must be accelerated to maintain an incompressible flow, and then retarded in the downstream direction as the $d(x)$ grows. As a result of this retarded motion, the relative turbulent intensities tend to be increased by the negative velocity gradient in the flow direction and by the higher velocity gradient due to the presence of the lower momentum fluid. The total turbulent energy is, thus, progressively

generated outward from the wall as one moves downstream from the roughness discontinuity. As a consequence, the higher turbulent shear stress will tend to reduce the velocity gradient through intense vertical mixing, and in turn, the turbulent intensity and shear stress would decrease farther downstream to approach another asymptotic state over the rough surface.

A thorough understanding of these intrinsic turbulence mechanisms, together with their interaction with the mean flow, will largely depend on the direct measurement of the individual terms of the turbulent energy equation in the present study.

2.2 Literature Review

In order to show the relevance for the study of the behavior of boundary layers to roughness changes, many previous predictions will be summarized and briefly reviewed. Their limitations or the range of validity will be indicated as well.

2.2.1 Clauser's qualitative argument - A qualitative understanding of the response of a boundary layer to a roughness change began earlier with Clauser's (1956) demonstration of his black box analogy in viewing the response of the layer to an impulse input as

$$I(t) = \left(\frac{\delta^\dagger}{\tau_w}\right) \frac{d\tau_w}{dx} \qquad (2\text{-}14)$$

in which $\delta^\dagger$ is an appropriate thickness which expresses the effect of the shear gradient in the universal scheme without dependence on wall shear stress τ_w. The experiment was performed in a constant pressure turbulent boundary layer from a smooth plate to corrugated paper. The

variable $(\delta^{\dagger}/\tau_w)\ d\tau_w/dx$ experienced an impulse resembling the Dirac function because of the abrupt change of τ_w.

Three results turned out to be of particular importance in the later development of all the theoretical models.

(i) The abrupt change of skin friction was felt immediately by the fluid nearest the wall. It propagated rapidly through the inner layers and then more slowly through the outer layer.

(ii) Even though $(\delta^{\dagger}/\tau_w)\ d\tau_w/dx$ was nearly zero after the disturbance, the layer was in a "transitory" state for a considerable distance behind the disturbance.

(iii) A longitudinal shear gradient $d\tau_w/dx$ has an important influence on the behavior of turbulent layers, an influence that has not been taken into account in previous work, such as Jacob (1939).

2.2.2 Theories of internal boundary layer - To make the flow field in the "transitory" state analytically tractable, the effect of the roughness change is assumed to be confined to a so-called "internal boundary layer" of thickness $d(x)$ within which the velocity or shear stress profiles may be represented by an assumed form. The flow above the boundary $d(x)$ is moving with the speed and shear stress that it had upwind of the roughness discontinuity. Most hypotheses on the internal boundary layer simplify the mathematics by requiring only that the continuity equation and the boundary layer equation in their integral forms are satisfied, that is

$$W = \int_{o}^{d(x)} - \frac{\partial U}{\partial x}\, dz \tag{2-15}$$

and

$$\int_{o}^{d(x)} \left(U \frac{\partial U}{\partial x} + W \frac{\partial U}{\partial z} \right) dz = U_{*o}^2 - U_{*1}^2 \tag{2-16}$$

loss of momentum by advection = net gain of momentum due to vertical flux

where one assumes that below $d(x)$ near the wall, the velocity distribution is given by

$$U = \frac{U_{*o}(x,z)}{K} \ln \frac{z}{z_o} \tag{2-17}$$

in which K and z_o are independent of x, U_{*1} and U_{*o} are the surface friction velocities upwind and downwind of the roughness discontinuity, respectively, and z_1 and z_o are the corresponding roughness lengths.

Following Elliott's initial work (1958), a number of other investigators, including Panofsky and Townsend (1964), Townsend (1965a, 1965b), Taylor (1967), and Blom and Wartena (1969), have investigated essentially the same model with different assumptions on stress distribution. Elliott's (1958) model contained a physically unrealistic discontinuity in stress at the interface $d(x)$ which was implied in his assumption that

$$U_{*o}(x,z) = U_{*o}(x,o) \quad \text{for} \quad z < d(x) \quad . \tag{2-18}$$

Panofsky and Townsend (1964) removed this difficulty by assuming a linear variation of stress,

$$U_{*o}(x,z) = U_{*o}(x,o) - \left[U_{*o}(x,o) - U_{*1} \right] \frac{z}{d} \quad , \tag{2-19}$$

and were able to derive an expression for the ratio d/x for various roughness, which was on the order of 1/10 and agreed favorably with Elliott's simple dimensional argument:

$$\left(\frac{d}{z_o}\right)\left(\ln\frac{d}{z_o}\right)^{0.2} \propto \left(\frac{x}{z_o}\right)^{0.8} . \tag{2-20}$$

The interesting conclusion from both predictions at this point is that the growth of $d(x)$ is independent of wind speed, U_∞, and viscosity, which are usually important in the development of a boundary layer over a flat plate. The question has also been examined from a slightly different point of view, namely, as a problem in small-scale convection. R. J. Taylor (1962) reported a ratio d/x to be 1/100-150 on his wind-tunnel experiments.

P. A. Taylor (1967), based on an application of the Karman-Pohlhausen technique (Goldstein, 1938), was able to obtain a stress distribution in the form of

$$U_{*_o}(x,z) = U_{*_o}(x,o) + (U_{*_o}-U_{*_1})\left[10\left(\frac{z}{d}\right)^2-15\left(\frac{z}{d}\right)^4+6\left(\frac{z}{d}\right)^5\right] \tag{2-21}$$

which was later found to be less suitable than the form of Eq. (2-19), in comparison with his numerical model (1968). Townsend (1965a, 1965b) tried to summarize the previous work and introduced, in a strictly theoretical manner, a self-preserving development of the change of the velocity profile downwind of the roughness discontinuity. It appears that the desired quantities can be then found by applying similarity arguments, given only in terms of the length scale $d(x)$ and a velocity scale $U_{*_o}(x)$. A brief review of this similarity theory is necessary before realizing its range of validity.

Townsend distinguished the change of the velocity profile due to flow acceleration $A(z)$ from the change due to streamline displacement $\delta(z)$, then

$$U_o - U_1 = A(z) - [U_{*1}\delta(z)/Kz] \tag{2-22}$$

in which U_1 represents the original velocity profile, given by

$$U_1 = \frac{U_{*1}}{K} \ln\left(\frac{z}{z_1}\right) . \tag{2-23}$$

Using the continuity equation, it is possible to derive a relation between $\delta(z)$ and $A(z)$. Then, Townsend assumed the following self-preserving forms for $A(z)$ and the stress distribution τ

$$A(z) = U_* K^{-1} f(\tfrac{z}{d}) \tag{2-24}$$

$$\tau = U_{*1} + (U_{*o}^2 - U_{*1}^2) F(\tfrac{z}{d}) \tag{2-25}$$

in which $f(\frac{z}{d})$ and $F(\frac{z}{d})$ are universal functions, independent of x owing to the assumed self-preservation. Substituting Eqs. (2-24) and (2-25) into the boundary layer equation

$$U \frac{\partial U}{\partial x} + W \frac{\partial U}{\partial z} = \frac{\partial \tau}{\partial z} \tag{2-26}$$

gives an ordinary differential equation for large $\ln(\frac{d}{z_o})$ values:

$$-\eta f'(\eta) = F'(\eta) \tag{2-27}$$

where $\eta = z/d$. An explicit form for $f(\eta)$ and $F(\eta)$ can be obtained only by making an assumption about the interaction between the velocity field and the turbulent motion. Townsend employed a simple assumption, namely, the "mixing length" or "eddy viscosity" assumption, and ended up with the stress distribution:

$$U_{*o}(x,z) = U_{*1} + U_{*o}(x,o)\left[1 + \left(\ln\frac{d}{z_1} - \ln\frac{z_o}{z_1} + \ln\frac{z}{d}\right)\right] \quad . \qquad (2\text{-}28)$$

For the exact form of $F(\eta)$, one must look at the energy equation. In his conclusions, Townsend also remarked the self-preserving development is possible only if $|U_{*o}/U_{*1}|$ is small, and if $U_{*o} >> U_{*1}$. For changes of friction velocities that are not small, the dynamics of the self-preserving flow will change slowly with x. In order to compare the laboratory results of an experiment in which air flowed from a smooth surface onto a water surface, Plate and Hidy (1967) added advection to Elliott's techniques and incorporated Townsend's analysis in a modified form, such that the result can be extended to calculate the velocity distribution for the cases in which

(i) $\delta(z)$ is not negligibly small compared with $d(x)$,

(ii) the effect of non-uniform shear at the surface must be considered, and

(iii) a pressure gradient, independent of z exists in the x direction.

Blom and Wartena (1969) corrected a minor discrepancy between Townsend's resulting velocity profile and his inner boundary condition, and further extended Townsend's theory to the case of two subsequent abrupt changes of surface roughness. By means of a numerical example, they found that the growth of $d(x)$ downwind of the second abrupt change is of the same order as that behind the first one.

In conclusion, it is fair to state that, because of the agreement of the results of various theoretical investigators using internal-boundary-layer theory, one finds that velocity changes are relatively insensitive to

the assumptions on the turbulent exchange process provided the velocity profile remains logarithmic close to the surface. And quite obviously, the internal boundary layer hypothesis can hardly go beyond the boundary layer equation (Eq. 2-26) to include more significant terms that might be relevant in the study of non-homogeneous terrain, also, the interface d(x) is, by all means, an ill-defined length scale from a practical point of view.

2.2.3 Numerical simulation - Numerical integration permits inclusion of terms that are difficult to be treated by internal boundary layer models. It should therefore lead to a broader insight into the physics of the problem.

Onishi (1966) and Wagner (1966) were the first to attempt a numerical simulation of atmospheric boundary layer flow over terrain with a roughness discontinuity. Their models were all based on the two-dimensional Navier-Stokes equations, Eqs. (2-2) and (2-3). With the eddy diffusivity assumption, Eqs. (2-2) and (2-3) become

$$\frac{\partial U}{\partial t} + U \frac{\partial W}{\partial x} + W \frac{\partial U}{\partial x} = - \frac{1}{\rho} \frac{\partial p}{\partial x} + \frac{\partial}{\partial x} \left(D_x \frac{\partial U}{\partial x} \right) + \frac{\partial}{\partial z} \left(D_z \frac{\partial U}{\partial z} \right) , \qquad (2\text{-}29)$$

and

$$\frac{\partial W}{\partial t} + U \frac{\partial W}{\partial x} + W \frac{\partial W}{\partial z} = - \frac{1}{\rho} \frac{\partial p}{\partial z} + \frac{\partial}{\partial x} \left(D_x \frac{\partial W}{\partial x} \right) + \frac{\partial}{\partial z} \left(D_z \frac{\partial W}{\partial z} \right) . \qquad (2\text{-}30)$$

Both Onishi and Wagner did not consider the horizontal mixing terms because D_x is not theoretically given. However, Wagner examined the relative magnitudes of these terms in a numerical scheme for roughness change from 1 cm to 10 cm, and showed that the difference on solutions was very small between two arbitrarily specified form: $D_x = 0$ and $D_x = 5D_z$.

Onishi obtained solutions to the steady state equations and took into account the dynamic pressure force near the roughness discontinuity. He also introduced a linear variation of z_o instead of the step change of z_o at the roughness discontinuity. Wagner's model was designed for an initial-value problem in an unsteady state. The condition for computational stability in his case is

$$\Delta t \leq \frac{1}{\left[\frac{\bar{U}}{\Delta x} + \frac{2D_z}{(\Delta z)^2}\right]} \tag{2-31}$$

which was derived originally for two linearized equations with forms similar to Eqs. (2-29) and (2-30). This relation proved to be usually a good approximation for the more general non-linear equations with variable coefficients. The condition in Eq. (2-31) can also be necessary and sufficient for convergence if the initial-value problem is properly posed, as was shown by Richtmyer (1957). At about the same time, Nickerson (1967), followed by Taylor (1968), also applied the initial value approach to integrate numerically the boundary layer equation (Eq. 2-26). Together with the continuity equation and the "mixing-length" assumption, their results near the discontinuity were found to be significantly larger than the predictions of internal-boundary-layer theories. It turns out that agreement can be attained if the effects of vertical motion are neglected in the numerical calculations. This discrepancy from those of internal boundary layer theories was also supported by the results of Onishi and Wagner. There is no doubt that numerical techniques should be of great value in modeling non-uniform boundary layer flows that are beyond the scope of similarity solutions. It is

for this reason that the present wind-tunnel observations compared with the numerical results such as those obtained by Nickerson (1967) are considered more significant.

Bradshaw et al. (1966), following Townsend (1961), defined three simple empirical functions relating the turbulent intensity, diffusion, and dissipation to the shear stress profile as follows,

$$a_1 = \frac{\tau}{\rho \overline{q^2}} \tag{2-32}$$

$$L = \frac{(\tau/\rho)^{3/2}}{\xi} \tag{2-33}$$

$$G = \left(\frac{\overline{pw}}{\rho} + \frac{1}{2}\overline{q^2 w}\right) \Big/ \left(\frac{\tau_{max}}{\rho}\right)^{\frac{1}{2}} \frac{\tau}{\rho} \tag{2-34}$$

in which $\overline{q^2} = \overline{u^2} + \overline{v^2} + \overline{w^2}$, $\tau = -\rho\overline{uw}$, and $\xi = \nu(\partial u_i/\partial x_j)^2$ so that the turbulent energy equation for a two-dimensional incompressible boundary layer,

$$\left(U \frac{\partial}{\partial x} + W \frac{\partial}{\partial z}\right) \frac{1}{2} \overline{q}^2 = \frac{\tau}{\rho} \frac{\partial U}{\partial z} - \frac{\partial}{\partial z}\left(\frac{\overline{pw}}{\rho} + \frac{1}{2}\overline{q^2 w}\right) - \xi \tag{2-35}$$

can be transformed into an equation for turbulent shear stress,

$$U \frac{\partial}{\partial x}\left(\frac{\tau}{\partial a_1 \rho}\right) + W \frac{\partial}{\partial z}\left(\frac{\tau}{\partial a_1 \rho}\right) - \frac{\tau}{\rho}\frac{\partial U}{\partial z} + \left(\frac{\tau_{max}}{\rho}\right)^{\frac{1}{2}} \frac{\partial}{\partial z}\left(G \frac{\tau}{\rho}\right) + \frac{(\tau/\rho)^{3/2}}{L} = 0 \quad . \tag{2-36}$$

This equation, together with the mean momentum equation and the mean continuity equation for a two-dimensional flow, form a hyperbolic system with three unknowns, i.e., U , W and τ . Bradshaw et al. indicated that the numerical integrations by the method of characteristics with preliminary choices of the three empirical functions compared favorably

with the results of conventional calculation methods over a wide range of pressure gradients. By dividing through by τ/ρ , it can be seen that Eq. (2-36) is the "mixing length" equation with additional terms representing advection and diffusion. Therefore, this method should be considered as a refinement of the "mixing-length" or "eddy viscosity" assumption. Most of all, their results suggested a much closer connection between the shear stress profile and the turbulent structure than between the shear stress profile and the mean velocity profile, wherever the effect of the past history of the boundary layer becomes important.

2.2.4 Laboratory simulations and field observations - The early laboratory investigation of this problem has been carried out by Jacobs (1939) and Clauser (1956) with only the measurements of mean velocity distributions. Jacobs' experiments were carried out in a fully developed channel flow. He found that the surface shear stress assumed its new value immediately downstream of the discontinuity; this was not confirmed by later experiments. In Taylor's (1962) experiments, the boundary layer was formed and changed suddenly from a rough to a smooth surface. The experimental results indicated a distribution of shear stress similar to that obtained by Jacobs but the assumption of a logarithmic velocity distribution near the roughness discontinuity appears questionable. Logan and Jones (1963) made measurements of Reynolds stresses in the "transitory" region following an abrupt increase in surface roughness of a pipe. They concluded that Reynolds stresses throughout much of the "transitory" region reach values exceeding those in fully developed flow in the rough pipe, and that shear stress distributions must be known for use in the calculation of velocity distributions. Later, Antonia and Luxton (1968) reported on wind-tunnel measurements in which two-dimensional

square-sectioned ribs were used as roughness elements. Their limited turbulence results showed the same trend as those obtained by Logan and Jones for the pipe flow. However, their mean velocity profiles both inside and outside of the inner layer exhibited a linear trend when plotted in the form U versus $z^{\frac{1}{2}}$. They used the point of intersection of the two straight lines to define the edge of the "internal boundary layer," which was found to depend linearly on x, i.e., the inner boundary layer develops in the manner of a two-dimensional wake.

Observations of the velocity changes under various surface conditions have been made by several researchers, (Lettau et al., 1962; Rider, Philip and Bradley, 1963), in the atmospheric boundary layer, mostly for moderate values of U_{*o}/U_{*1} near 0.7. Accuracy of the observations is not sufficient to lead to definite results which could be used to confirm theoretical models.

2.2.5 Review of the related diffusion studies - The only available diffusion studies under the effect of topographical change are those of Hino, (1965, 1967a, 1967b). Theoretically, Hino suggested a conventional numerical analysis of the Eulerian diffusion equation for a point source

$$U \frac{\partial C}{\partial x} + W \frac{\partial C}{\partial z} = \frac{\partial}{\partial z}\left(\sigma_{zz} \frac{\partial C}{\partial z}\right) + \frac{\partial}{\partial y}\left(\sigma_{yy} \frac{\partial C}{\partial y}\right) , \qquad (2\text{-}37)$$

which resulted from the assumption that the principal axes of the mass diffusivity tensor σ_{ij} are oriented parallel to the coordinate system oxyz, and the term $\partial/\partial x\ (\sigma_{xx}\ \partial C/\partial x)$ is negligibly small compared with the convective term $U\ \partial C/\partial x$. In his analysis the diffusion coefficients are assumed to be different functional forms of total turbulent energy at different heights,

$$\begin{cases} \sigma_{yy} = A_1(x - x_s)^{n1} \ (\overline{q^2})^{\frac{1}{2}} & \text{for} \quad 0 \leq z \leq z_1 \\ \sigma_{yy} = A_2(x - x_s)^{n2} \ (\overline{q^2})^{\frac{1}{2}} & \text{for} \quad z_1 < z \quad , \end{cases} \tag{2-38}$$

$$\begin{cases} \sigma_{zz} = A_3(\overline{q^2})^{\frac{1}{2}} \ z^m & \text{for} \quad 0 \leq z \leq z_1 \\ \sigma_{zz} = [A_z + B_z \sin^2\{(z-z_1)/z\}](\overline{q^2})^{\frac{1}{2}} & \text{for} \quad z_1 < z \leq z_2 \\ \sigma_{zz} = [A_z + B_z \sin^2\{(z_2-z_1)/z\}](\overline{q^2})^{\frac{1}{2}} & \text{for} \quad z_2 < z \end{cases} \tag{2-39}$$

in which z_1 and z_2 are the heights from the wall where diffusion coefficients change, x_s is the coordinate of the x axis of the source, and A_1 , A_2 , ..., m, n, etc. are parameters. These assumptions are basically in agreement with the two-layer model, the theory of the internal boundary layer, but the exact forms of Eqs. (2-38) and (2-39) are open to discussion.

Yamamoto and Shimanuki, (1963), reported a numerical solution of Eq. (2-37) using the vertical diffusivity derived from mixing-length theory and an assumed lateral diffusivity of the form

$$\sigma_{yy} = \sigma_{zz} \ \alpha \ (\frac{z}{L}) \quad , \tag{2-40}$$

in which α is an unknown function of z/L , where L is the stability length introduced by Monin and Obukhov, (1954). Surprisingly, α was found to be approximately 13 under neutral-stability conditions when the calculated diffusion patterns were compared with the observations made during projects Prairie Grass and Green Glow over a homogeneous terrain.

Batchelor (1959, 1964) suggested that the statistical functions relating to the motion of a marked fluid particle possess Lagrangian similarity in the constant-stress region of a turbulent boundary layer,

in which mean velocity varies as the logarithm of wall distance z. Based on this hypothesis he was able to predict that dispersion and maximum mean concentrations are proportional to certain powers of downstream distance x. For a continuous point source at the ground level he obtained

$$C_{max}\ (\bar{x},o,o) \propto \frac{Q_{cp}}{b^2 K U_* x^2} \ln \frac{C\bar{z}}{z_o} \quad , \tag{2-41}$$

in which Q_{cp} are the rate of source strength, and b and c are parameters. This prediction has been supported experimentally by numerous others for a fully developed boundary layer, (Cermak, 1963), but has not yet been studied in the roughness-change flow. Principally, the Lagrangian similarity hypothesis can be employed to the roughness change case as long as the assumption of a constant-stress region is justified, and the velocity profile remains logarithmic close to the surface. However, based on the previous discussion that z_o might be a function of x in the non-homogeneous terrain, Eq. (2-41) must be modified accordingly to a different functional form of x.

Chapter III

EXPERIMENTAL EQUIPMENT AND MEASUREMENT PROCEDURE

In this chapter, the experimental equipment and measurement procedure made for this study are briefly described. The instruments used were part of the standard laboratory equipment at the Fluid Dynamics and Diffusion Laboratory of Colorado State University. Emphasis is given to the establishment of the required flow conditions and turbulence measurements.

3.1 Wind Tunnel and Equipments for the Flow Setup

The experiments were carried out in the low-speed wind tunnel (Fig. 2) at Colorado State University. The tunnel is a closed circulating type with a test length of 30 ft, and a cross-sectional area of 6 x 6 ft^2. The free stream turbulence level $\sqrt{\overline{u^2}}/U_\infty$ is kept within $\pm$ 2% by an inlet con triction ratio of 4:1 and a damping screen. Air flow in the tunnel is driven by a constant speed-pitch-controlled fan, which can vary the wind speed from 3 fps to about 75 fps. There is no arrangement for temperature control in the tunnel.

The bulk of data were taken in a thin boundary layer (approximately 3 inches at the step change of roughness), developed over a 3 ft wide flat plate, which was elevated at a height of 2 ft from the wind tunnel floor in order to avoid the secondary motions resulting from the excessive loss of momentum in the corners of the tunnel. The flat plate (Fig. 3) consisted of a smooth front section of a 6 ft length and a rough downstream section of a 4 ft length. The smooth section was made of polished aluminum. A 4-inch wide strip of sandpaper (Grid 36) was

attached across the whole width of the plate at a distance of one inch from the leading edge for tripping the turbulent flow and thickening the boundary layer. The rough section was made of plywood, uniformly and randomly covered with a layer of angular gravel with an average size of 1/4 in. (obtained according to A.S.T.M. Specifications of U.S. Standard Sieve Series). Since turbulence is a statistical phenomenon, the randomly distributed roughness of irregular shape should preserve this statistical concept more favorable than any geometrically well-defined roughness.

Two rows of pressure taps with 1/32 in. in diameter holes, placed at a distance of 6 in. on either side of the centerline, were used to measure the wall static pressure along the flat plate. Little appears to be known about the accuracy of wall pressure measurements in the irregular rough surface, but the results indicate that the flow is nearly two-dimensional because measurements from the two lines of pressure taps are considered practically identical within the experimental errors as shown in Fig. 4. A more satisfactory way for testing two-dimensionality of the flow should be, perhaps, performed by measuring the wall shear stress pattern. The usual devices, such as Preston tubes, or even a visualization technique, were found to be very uncertain in application to the rough surface. Instead, a comparison of similar profiles of mean velocity and turbulent intensity $\overline{u^2}$ within the flow extending to 8 in. on either side of the centerline for a downstream distance of 9 ft. from the leading edge of the flat plate (i.e. $x = 3$ ft) (Figs. 5 and 6) should necessarily show no signs of three-dimensional effects, resulting from the whirling motion generated from the corners of the leading edge of the flat plate. It was thus concluded that centerline measurements would be representative of a truly two-dimensional flow.

To obtain a zero pressure gradient outside of the boundary layer, a specially shaped false ceiling was mounted onto the tunnel ceiling (Fig. 7). The shape of the false ceiling shown in Fig. 8 was found by trial and error. The dimensionless relative static pressures $(p-p_{ref})/\frac{1}{2}\rho U_\infty^2$ measured outside of the boundary layer were plotted against the downstream distance, x, in Fig. 9; p_{ref} was the wall static pressure at the station 3 ft downstream from the leading edge. The maximum magnitude of pressure gradient was about 0.215×10^{-5} psi/in. if the first two-foot section of the flat plate was excluded.

Remote control sensing probes were mounted on a vertically movable carriage, which, with a minimum disturbance, would allow the measurements to be done at any desired height above the flat plate.

3.2 Measurements of Mean Velocity and Pressure Gradient

The mean velocity was measured with both a 1/8 in. diameter Pitot static tube of Prandtl design and a single hot wire. The technique in employing hot wires will be fully discussed in the next section. The Pitot static tube was connected to an electronic differential pressure transducer (Transonic Equibar Type 120), which was, in regular intervals, calibrated against a standard micromanometer (Meriam model 34). From knowledge of the dynamic pressure, the barometric pressure, and the temperature, the velocity could be readily calculated.

Lacking a well-designed integrator circuit, all the mean velocity data were measured on a point-by-point basis and recorded on a x-y plotter (Type Moseley 135), with x axis registered on a time base of 10 seconds per inch of paper. The hot wire results, uncorrected for the effects of turbulence level and wall proximity, were generally in good agreement with the Pitot static values, which in turn, were uncorrected for the

effects of streamline curvature and turbulence. The degree of agreement is shown in Fig. 10 for the worst case at the station 2 inches downstream from the roughness discontinuity, where the maximum deviation was estimated to be less than 3% at the wall region. After correction of the Pitot-static data due to turbulence, the error, as also shown in Fig. 10, is reduced to approximately -1.5%. This error is within a response correction of +1.73%, obtained by Tieleman (1967) in calibrating the 1/8 in. diameter Pitot-static tube against a crystal tube. However, the velocity profiles reported in this experiment were obtained from hot wire data for the stations near to the step change, and Pitot static values for the other stations.

Static pressures were measured along the flat plate and in the flow for the stations near to the step change. For measuring pressures along the flat plate, the pressure taps, arranged at intervals shown in Fig. 3, were connected through plastic tubing to the electronic manometer where they were measured against a suitable reference pressure of the tap located at 3 ft downstream from the leading edge of the flat plate. The pressures in the flow were measured with the static pressure holes of a Pitot static tube. These pressures were recorded continuously by using the probe carriage which was driven by a small motor. A potentiometer geared to the guide bar of the carriage gave a voltage drop proportional to the distance from the flat plate, which was effectively applied as the x-axis of an x-y plotter (Type Moseley 135).

3.3 Measurements of Turbulence

3.3.1 Hot-wire anemometer and associated instrumentations - Three types of hot-wire arrangements were used to measure the various statistical quantities of turbulence, that is, a single wire, placed normal to

the flow, for measuring $\overline{u^2}$, the x-wires, and a yawed wire for measuring $\overline{uw}$, $\overline{w^2}$, and $\overline{uv}$, $\overline{v^2}$; the measurements of these turbulence quantities depend on the plane of axis in which the wires were operated. All the wires were made of 90% platinum and 10% rhodium, with a diameter of 0.0003 inch, a length of 0.05 inch for the single wire, and a length of approximately 0.07 inch for the yawed wire and x-wires. Wires were mounted on the ceramic probles with a diameter of only 3/32 inch, which gave the versatility of measurements at the wall proximity. The transistorized constant-temperature anemometers, designed without a linearizer at Colorado State University by Finn and Sandborn (1967), were used to operate the hot wires. The frequency response of this anemometer is flat up to 50,000 cps or greater.

The a-c outputs of the hot-wire anemometers were fed into a true RMS-voltmeter made by DISA Co., of which a built-in integrator was used to estimate easily the RMS values of the fluctuating electrical voltages over a period of 30 seconds. The d-c output of the single wire anemometer was read directly from a 4-digit digital voltmeter (Hewlett-Packard model 3440A) as a cross check of mean velocity measurements by Pitot static tube. Since the d-c output of hot-wire anemometer was on the order of one volt, the accuracy of the reading would fall into the order of several millivolts.

For the purpose of measuring spectrum and various second-order, or perhaps third-order correlations of turbulent components, the a-c outputs of anemometers for single wire as well as x-wires, at each selected point relevant in the flow field, were simultaneously recorded on magnetic tape for a period of five minutes. Because of the low a-c outputs of the anemometer and a maximum of 1 volt RMS recording limit to the tape

recorder (Mincom Type C-100), the signals were required to pass through the low-level preamplifiers (Tektronics Type 122) and a proper attenuating stage before recording.

Only the frequency spectra of horizontal turbulent component u were analyzed in the present study on a spectrum analyzer (Bruel and Kjear Type 2109). This instrument consists essentially of a set of passive filters in the range of 16 to 10,000 cps. The filters are of octave type varying in band width approximately proportional to the central frequency. Filter band width and recording noise were usually the primary causes of error in this measurement.

All the instrumentations and the procedure for these measurements are shown schematically in Fig. 11.

3.3.2 Calculations of turbulent intensities and shear stress - For the single wire placed normal to the direction of mean flow, the RMS value of a-c output of the anemometer is given by

$$\sqrt{\overline{e_s^2}} = \sqrt{\left(\frac{\partial E_s}{\partial U}\right)^2}\ \overline{u^2} \tag{3-1}$$

in which $\partial E_s/\partial U$ is the sensitivity of the single wire to velocity, obtained from the calibration curve between U and d-c output of the anemometer. Therefore, $\overline{u^2}$ can be calculated directly from the single-wire measurement.

For the x-wires placed in the x-z plane (Fig. 12), the corresponding RMS values of the a-c outputs of wire 1 and wire 2 will take the forms of

$$\sqrt{\overline{e_1^2}} = \sqrt{\overline{\left[\frac{\partial E_1}{\partial (U\cos\theta_1)}\ (u\cos\theta_1 + cw\ \sin\theta_2)\right]^2}} \tag{3-2}$$

$$\sqrt{\overline{e_2^2}} = \sqrt{\overline{\left[\frac{\partial E_2}{\partial (U\sin\theta_1)}\ (u\cos\theta_1 - cw\ \sin\theta_2)\right]^2}} \tag{3-3}$$

in which c is a constant factor (Champagne et al., 1967a, 1967b) taking into account the effects of the parallel component of the velocity on the heat transfer for the inclined wires. For the present experiments, a value of $c = 0.925$ was taken from Champagne et al (1967a, 1967b) for $\theta_1 = \theta_2 = 45^o$, and a length-to-diameter ratio of the wire approximately equal to 200.

After rearranging Eqs. (3-2) and (3-3), and solving simultaneously for $\overline{uw}$ and $\overline{w}^2$, one obtains

$$(0.925)^2\,\overline{w}^2 = \frac{1}{2}\left[\overline{e}_1^{\,2}\left(\frac{\partial U}{\partial E_1}\right)^2 + \overline{e}_2^{\,2}\left(\frac{\partial U}{\partial E_2}\right)^2\right] - \overline{u}^2 \qquad (3\text{-}4)$$

$$(0.925)^2\,\overline{uw} = \frac{1}{4}\left[\overline{e}_1^{\,2}\left(\frac{\partial U}{\partial E_1}\right)^2 - \overline{e}_2^{\,2}\left(\frac{\partial U}{\partial E_2}\right)^2\right] \qquad (3\text{-}5)$$

where $\overline{u}^2$ can be independently obtained from Eq. (3-1).

In the same fashion, $\overline{uv}$ and $\overline{v}^2$ can be measured by operating the x-wires in the x-y plane, and calculating equations similar to Eqs. (3-4) and (3-5). When yawed-wire techniques are used, the calculations can be simplified further by letting $\partial U/\partial E_1 = \partial U/\partial E_2$ in Eqs. (3-4) and (3-5). However, it is cumbersome to rotate the yawed wire while taking data.

Since the wire calibration is performed in the free stream, or under the condition of parallel flow, the sensitivity obtained would hardly be justified for the calculations of turbulence over the region of the step change, where a substantial vertical component of velocity is usually present. Corrections for a mild streamline curvature (Plate et al., 1969) can be readily obtained by introducing into Eqs. (3-2) and (3-3) $\theta_1 = 45^o + \varepsilon$, $\theta_2 = 45^o - \varepsilon$, and for small ε, $\varepsilon^2 \doteqdot 0$, $\sin\varepsilon \doteqdot \varepsilon$, $\cos\varepsilon \doteqdot 1$. Then, the corresponding results for Eqs. (3-4) and (3-5) become

$$(0.925)\ \overline{w^2} = \frac{1}{2}\left[\overline{e_1^2}\left(\frac{\partial U}{\partial E_1}\right)^2 + \overline{e_2^2}\left(\frac{\partial U}{\partial E_2}\right)^2\right] - \overline{u^2} - \varepsilon\left[\overline{e_1^2}\left(\frac{\partial U}{\partial E_1}\right)^2 - \overline{e_2^2}\left(\frac{\partial U}{\partial E_2}\right)^2\right] \quad (3\text{-}6)$$

$$(0.925)^2\ \overline{uw} = \frac{1}{4}\left[\overline{e_1^2}\left(\frac{\partial U}{\partial E_1}\right)^2 - \overline{e_2^2}\left(\frac{\partial U}{\partial E_2}\right)^2\right] - 2\varepsilon\ (0.925)^2\ \overline{w^2} \quad (3\text{-}7)$$

in which ε is estimated approximately from the measured streamline pattern. This correction has been found significant and effective in most types of measurements of disturbed boundary layer. Since the two wires of an x-wire probe are not placed in the same plane, this would require that some information be known about the "correlation" between the turbulent components over a small separation distance between the two wires. The errors incurred in this "correlation" could be substantial in a thin boundary layer. For this reason, the turbulence measurements reported in this experiment were obtained from the yawed-wire data.

3.4 Measurements of Mass Concentrations

A continuous point source with an injection orifice of 1/16 in. diameter was placed flush with the smooth surface 3 ft downstream from the leading edge of the flat plate. Pure helium gas (Grade A, AIRCO), used as a tracer, was released continuously at an exit flow rate of 10 fps from the source. A sampling probe with 1/16 in. diameter was operated at a sampling flow rate of 200 cc/min (or 1.12 in./sec). The sample was directly detected by a mass-spectrometer (Veeco Type MS9AB), of which the d-c output can only be measured on a point-by-point basis because of the slow time-response of the mass-spectrometer. For this reason, it was insufficient to measure concentration fluctuations.

The lateral and vertical concentration profiles were measured at several sections in the downstream direction from the source. The net concentrations, obtained by deducting the increasing ambient concentration resulting from the closed circulating type of wind tunnel, were calculated against a calibration curve based on three standard mixing gases of nitrogen and helium, (i.e., 0.5% He , 0.2% He , and 0.05% He).

The sensing system used in connection with the inlet leak of mass-spectrometer was interconnected with the electronic manometer (Transonic Equibar Type 120) to keep the measurement under the same imposed pressure drop of the sampling flow. This special arrangement of instrumentation, calibration, and error analysis is dealt with in detail in Meroney et al. (1968), and Plate and Sheik (1966). However, the 3-point calibration curve, buoyancy effect of helium, and the constant electronic drift of the mass-spectrometer made it difficult to measure the low concentration fluid with any certainty. Most of the data reported in this experiment should be considered to be in an error range of within 5% except the low-concentration measurement (Plate and Sheik, 1966).

Chapter IV

RESULTS AND DISCUSSION

The experimental investigations performed in this study involved various measurements in three different smooth-to-rough cases:

Case I: The average crests of the 1/4 inch sized roughness elements were elevated 1/8 inch from the smooth surface (Fig. 1). Measurements include mean velocities, wall pressures, mean-square turbulent velocities $\overline{u^2}$, $\overline{v^2}$, $\overline{w^2}$, turbulent shear stresses $-\overline{uw}$ and $-\overline{uv}$, and the mass (helium) concentrations from a continuous point source.

Case II: The average crests of the 1/4 inch-sized roughness elements were aligned with the smooth surface. Measurements include mean velocities, wall pressures, and the turbulent shear stress.

Case III: A standard 20-grid sand paper was used as the rough portion. Measurements include only the mean velocity distributions.

In this Chapter, the physical picture of the air flow over the step change of surface roughness will be examined closely from the experimental results obtained in Case I. The data from Cases II and III were gathered with the purpose of making the experimental conditions more compatible with those for the theoretical models so that a comparison of the experimental results with the theoretical calculations could possibly be reached. The limits of validity of the existing theories will be discussed in light of the extensive hot-wire measurements. Emphasis is given to the mean velocity distributions and the turbulence structure of the wall region immediately following the step change, or of the so-called "internal boundary layer". In

particular, one-dimensional spectral measurements will be used to establish whether the turbulence structure is strongly dependent on the particular roughness configuration.

4.1 Description of the Results

4.1.1 Mean velocity distributions and streamlines - The mean velocity data as obtained from the point-by-point measurements are tabulated in Table I for Case I, Table II for Case II, and Table III for Case III. The mean velocity distributions and the streamline patterns in the x-z plane are shown in Fig. 13 for Case I and Fig. 14 for Cases II and III. The profile distributions of mean velocity display an apparent characteristic of turbulent boundary layers although there are marked changes with the downstream distance in the profiles. The values of the dimensional stream function, ψ which were used in drawing the streamlines were obtained by plotting the velocity profiles in the form shown on the figures, namely,

$$U = \vec{U} \cos\beta = f(z) \quad , \tag{4-1}$$

in which $\vec{U}$ and β are the magnitude and direction of the local velocity vector, and evaluating the integral,

$$\psi(x,z) = \int_0^z U \, dz \quad . \tag{4-2}$$

However, the origin of the wall distance coordinate over the rough section may be taken anywhere between the deepest valley of the roughness and the highest crest (Clauser 1956). So, the question is can we find such a unique, experimentally determinable mean surface for

this particular roughness configuration? Perry and Joubert (1963) suggest an approximate method for graphically locating the origin of z, which turn out to give too rough an estimate. Hence, the data taken for all cases use the average crests of the roughness elements as the origin of z, in order to eliminate inconsistency resulting from selecting an abitrary method. The streamlines from this origin reveal strong variations of vertical velocity distribution encountering the rough surface. Because of these strong variations the magnitude of the vertical velocity components can be readily determined especially from the streamline pattern of Case I. The effect of the origin of z in locating the first streamline above the wall, as shown in Fig. 13, is of the order of 20% if the origin of z on the rough surface was the same as the smooth surface instead of 1/8 in. higher. An estimate of the difference was found to be 21% at $x = 0$ in., and 6% to 7% for the stations from $x = 2$ in. through $x = 12$ in. Nevertheless, the streamlines show only little distortion over the roughness discontinuity for the Cases II and III.

The longitudinal velocity distributions for several vertical locations are shown in Figs. 15, 16, and 17. The curvatures provide a clear picture of the fluid strata accelerations over the "transitory" region. Near the wall, a steady retardation of the fluid is noted. The fluid farther from the wall is at first accelerated and then retarted. These phenomena substantiate the previous discussions in 2.1.3. The sharp velocity gradients near the wall are characteristic of this flow field. These velocity gradients interacting with the turbulent shear stress will, in turn, cause a large increase in the amount of turbulent energy of the flow. Again, these acceleration-

and-retardation behaviors are less clear for Cases II and III due to the correspondingly low wall shear stress. This will justify the detailed measurements for Case I in order that a slight variation in any structure could be easily distinguished.

The displacement thickness δ^* and the momentum thickness θ of of the velocity profiles were calculated for all cases according to their usual definitions (e.g. Schlichting 1960). As can be seen from the values listed in Table IV, δ^* and θ show considerable change as well as some fluctuations at the roughness discontinuities. The observed fluctuations seem to be characteristic of boundary discontinuities and were also observed by Plate and Hidy (1967). For one or two inches downstream from the discontinuity, both δ^* and θ increase rapidly, suggesting an overshooting of the shear stress.

4.1.2 Mean velocity structure of internal boundary layer - The well-known law of the wall, i.e. eq. (2-10), has been successful in the past in describing the wall flow over homogeneously smooth and rough surfaces. Without questioning it's applicability to the "transitory" region of the roughness-change flow, a typical semi-logarithmic plot of dimensionless velocities and wall distance was given in Fig. 18 for all the velocity profiles in Case I. It revealed that the straight-line logarithmic portions of the velocity profiles could only be distinquished for $x < 0$, and became curved for $x \geq 0$. This deflection was obviously due to the ill-defined zero origin of z over the rough surface nor did the trial-and-error schemes of shifting a constant amount of wall distance z on the logarithmic scale give us any satisfactory results for all the profiles. Thus, it may be concluded that fitting a straight logarithmic line is unsuitable for the rough

surface, and, perhaps a straight logarithmic line does not even exist in the "transitory" region of the roughness-change flow. However, if the adjustment of flow to the change of roughness may be assumed as rapid in the inner region near the wall, some pertinent parameters based on data can be evaluated, so that the structure of the mean flow at the wall region could be closely observed in the context of the functional hypotheses of Clauser (1956) and Coles (1956):

(a) Shear velocity U_* - The shear or friction velocities, U_* (where U_* is equal to the square root of the ratio of the shear stress and the air density), were calculated from the slope (or the tangent) of the measured logarithmic profiles in accordance with eq. (2-10), and the results for all three cases are listed in Table IV. The results over the smooth plate have also been cross-checked against the well known Ludwieg and Tillmans' formula

$$U_*^2 = \left[0.123 \times 10^{-0.678H} U_\infty^2 \times \left(\frac{U_\infty \theta}{\nu}\right)^{-0.268}\right]^{\frac{1}{2}} , \qquad (4\text{-}3)$$

in which H denotes the ratio of δ^* to θ, ν is the kinematic viscosity of air, and U_∞ is the free stream velocity outside the boundary layer.

From eq. (4-3) and the data of Table IV for profiles at -6 inches $< x <$ - 2 inches, an average U_* was found to be 0.86 ft/sec for Case I, 0.85 ft/sec for Case II, and 1.35 ft/sec for Case III. These values agree quite satisfactorily with the data obtained from the velocity profiles, indicating that the flow was fully-developed and remained aerodynamically smooth on entering the rough surface.

To obtain consistent estimates for U_* over the rough surface, the best fitting tangent of the logarithmic plot of the velocity data

near the heights $z = 0.07\ \delta$ (δ is the local thickness of boundary layer) were used. The results, as listed in Table IV, reveal in general that a steady increase of U_* for the first six inches downstream from the discontinuity occurs in all cases. And, the U_* values decrease only gradually after reaching the maxima, which are approximately located at $x = +5$ inches for all the cases. These results indicate that the shear velocity in the "transitory" region immediately behind the discontinuity has a value exceeding that expected for fully-developed flow along a rough surface of uniform but identical roughness. Experimentally, this type of response in wall shear stress is an important result, which has been predicted by numerous theoretical models (e.g. Townsend 1965a,b, Onishi 1966, Wagner 1966, etc.).

The observed shear velocities over the rough surface are in fair agreement with values calculated from the method based on Karman's momentum integral equation for zero longitudinal pressure gradient without the assumption of a logarithmic profile, i.e.,

$$U_*^2 = \frac{d}{dx}\,(U_\infty^2\theta) \quad . \tag{4-4}$$

A comparison of these results are shown in Fig. 13 for Case I only. For Cases II and III, the comparisons become less significant because the θ values as listed in Table IV exhibit too much fluctuation for an accurate estimate.

In principle, the shear velocity distribution may be obtained by extrapolating the $-\overline{uw}$ profiles through the longitudinal gradients of the wall pressure, but the results turned out to be significantly lower in comparison with those determined from mean velocity data.

This discrepancy may be expected since it is not clear where one would measure the static pressure along a rough boundary. Chao and Sandborn (1965) found that the pressure gradient along the bottom of the roughness elements is opposite in sign to the pressure gradient along the top of the roughness elements. If this correction could be applied to our type of roughness, the U_* values obtained from $-\overline{uw}$ profiles would be more in agreement with those from the mean velocity data.

(b) Roughness length z_o - Values of z_o were determined from the mean velocity profiles simultaneously with U_* in the previously described manner. They are also listed in Table IV for all cases. For an aerodynamically smooth boundary, z_o is proportional to ν/U_*, in which ν is the kinematic viscosity of the air. Based on the average z_o values of the data for $x < 0$ in Table IV, the factor of proportionality was found to be about 0.14 for Cases I and II, and 0.075 for Case III. These values are in good order of magnitude agreement with the approximate value 0.09 according to Nikuradse's criterion (Ellison 1956).

A comparison of eq. (2-10) with the two well-known velocity distributions for the rough-wall flow

$$\frac{U}{U_*} = \frac{1}{K} \ell n \frac{z}{k_*} + M \left(\frac{k_* U_*}{\nu}\right) , \tag{4-5}$$

or

$$\frac{U}{U_*} = \frac{1}{K} \ell n \frac{zU_*}{\nu} + N - \frac{\Delta U}{U_*} \left(\frac{k_* U_*}{\nu}\right) , \tag{4-6}$$

shows that an equation for z_o can be written as

$$\ell n\ z_o = \ell n\ k_* - K \times M\ (\frac{k_* U_*}{\nu}) \qquad (4\text{-}7)$$

or $$\ell n\ z_o = \ell n\ \frac{\delta}{U_*} - N \times K + K \times \frac{\Delta U}{U_*}\ (\frac{k_* U_*}{\nu}) \qquad (4\text{-}8)$$

Eq. (4-5) is the form adopted by Nikuradse for his pipe data, while eq. (4-6) is the form used by Clauser (1956) and Hama (1954). When plotted on the basis of U/U_* versus $\log_{10}(zU_*/\nu)$, given in Fig. 20 for Case I, eq. (4-6) is represented by a family of straight parallel lines, each being displaced downwards from the smooth wall profiles by a different magnitude of the roughness function $\Delta U/U_*$. The z_o variation as expressed by $\Delta U/U_*$ can be readily seen in Fig. 20, which behaves identically with the z_o values given in Table IV. The same behavior of z_o corresponding to that of U_* for $x > 0$, which is also observed in Table IV, indicates that at heights of order of z_o, the turbulence properties do depend on z_o. And at greater heights the significant effect of z_o seems to impose only a constant translation velocity on the whole flow.

(c) Karman constant K - Since, in the wall region of a fully developed boundary layer, the local rates of production and dissipation of turbulent energy are usually assumed very high compared with the rate of energy gained by advection from the outer strata, the flow near the wall is entirely characterized by the local velocity gradient, and is otherwise independent of the history of the boundary layer. Thus, from eq. (2-10), it follows that

$$\frac{dU}{dz} = \frac{(\tau/\rho)^{\frac{1}{2}}}{Kz} = \frac{(-\overline{uw})^{\frac{1}{2}}}{Kz} \quad . \qquad (4\text{-}8)$$

From the experimental results of Reynold stress and the mean velocity profiles, the Karman constant K can be calculated. For a wall distance of less than $z/\delta = 0.1$, an approximately constant value of K was found at each x. The calculated K values when plotted versus x were unexpectedly found to follow the variations of wall-pressure measurements. This finding, as clearly shown in Figs. 21 and 22 for both Case I and Case II, was not expected from our similarity argument (i.e. eq. (2-9)).

4.1.3 Turbulent results - The distributions of the turbulent shear stress $-\overline{uw}$ and the turbulent velocities $\overline{u^2}$, $\overline{v^2}$, and $\overline{w^2}$ are shown in Fig. 13 and Fig. 23 for Case I. The numerical values of all the turbulence quantities measured in Case I are also tabulated in Table V, together with the only $-\overline{uw}$ measurements in Case II, which were obtained from the yawed-wire data.

A careful study of the turbulence velocities and shear stress curves and the velocity profiles reveals that the turbulence velocities and shear stress at any wall distance do not increase above their initial values until the velocity gradient at that wall distance has increased. This can just as well be illustrated by Figs. 15, 16, and 17, in which both the longitudinal and the traverse velocity gradients do not increase until the fluid layer at that wall distance has attained its maximum velocity. Thus, the points at which the turbulence intensities begin to increase correspond approximately to the curves of Figs. 15, 16, and 17. However, this correspondence becomes less clearly defined as the flow approaches the free stream.

The maximum values of shear stress and turbulence intensities occur at approximately the same wall distance downstream from

x = + 6 inches, the fact that these maxima occur so far from the wall is not expected from any early turbulence data obtained from the smooth surface with zero pressure gradient, expecially since the lower turbulence intensities close to the rough surface are not accompanied by a decrease in mean velocity gradient. A shear stress maxima away from the wall is also found in Chowdhury's (1966) measurements. As noted by Kline et al (1967), close to the smooth wall, the momentum transport is dominated by eruptions from the so-called "laminar sublayer" and new turbulence is thus produced. Since this sublayer instability mechanism does not seem to exist on the rough surface, it appears that turbulence generated in the immediate vicinity of the roughness, transported downstream and away from the wall by the mean motion may explain the maxima.

Though the shear stress close to the rough surface can not be accureately measured, the curvatures of the shear stress profiles as shown in Fig. 13 tend to show an increase in the wall shear stress immediately downstream from the roughness discontinuity. Also, a slight decrease can be noticed when the shear stress profiles display maxima at some distance away from the wall.

One dimensional energy spectra of longitudinal turbulent velocity evaluated for various wall distances at x = - 12 in., + 4 in., + 6 in., + 12 in. are given in Table VI for Case I only. Because of the strong noise levels of the magnetic tape recorder, the part of the spectra corresponding to frequencies above 2000 Hz was not usable.

The normalized spectra for the stations x = - 12 in., + 4 in., + 6 in., + 12 in. are shown in Figs. 24, 25, 26, 27,

$$\int_0^\infty \frac{F(k_1)}{\overline{u^2}}\, dk_1 = 1 \quad , \tag{4-9}$$

in which $k_1 = 2\pi f/U$ is the one-dimensional wave number. In the outer region of the boundary layer there is an extensive region where the spectrum varies as $k_1^{-5/3}$ corresponding to the non-viscous subrange. The extent of this subrange becomes less clear as it approaches the wall, within which the spectrum function varies as k_1^{-1} in accordance with a theoretical prediction by Tchen (1953). Nearly all of the spectra indicate the existence of a region varying as k_1^{-7} at the high-frequency end.

When the spectra are plotted in the similarity form of the universal equilibrium law of Kolmogoroff, the shape of the spectra are identical for all data in the high wave number region and they collapse on a single curve, which is comparable with Heisenberg's (1948) theory for one-dimensional energy spectrum of longitudinal fluctuations (Rotta 1962), i.e.

$$F(k_1) = \int_{k_1}^\infty \frac{k^2 - k_1^2}{k^3} E(k)\, dk \quad , \tag{4-10}$$

in which $E(k)$ is the three-dimensional spectrum with the form in the equilibrium range as

$$E(k) = \left(\frac{8\xi}{9a}\right)^{2/3} k^{-5/3} \left[1 + \frac{8\nu^3}{3a^2\xi} k^4\right]^{-4/3} \tag{4-11}$$

in which a is a constant. If the numerical value of a is precisely known, eq. (4-10) can be numerically integrated and the results compared with our measurements. For this illustration, the data of Table

IV have been replotted, as given in Fig. 28, 29, 30, 31, in a dimensionless form

$$\phi\left(\frac{k_1}{k_s}\right) = \frac{F(k_1)}{(\xi\nu^5)^{\frac{1}{4}}} \quad , \tag{4-12}$$

in which $k_s = (\xi\nu^{-3})^{\frac{1}{4}}$ is the Kolmogorov wave number based on the dissipation of ξ. As an estimate for the dissipation ξ, the isotropic relation has been used

$$\xi = 15\ \nu\ \overline{u^2} \int_0^\infty k_1^2\ F(k_1)\ dk_1 \quad . \tag{4-13}$$

Various parameters involved in the above-mentioned spectrum calculations are given in Table VII. Since the equilibrium range of the spectrum is characterized by eddies much smaller than the scale of energy containing eddies, the structure of such eddies remains largely unaffected by the large scale motion. This leads to the surprising result that the high frequency end of the spectra, even in the "transitory" region of our case, can be exactly represented by the high frequency shape of the undisturbed turbulence in a boundary layer along a flat plate. A similar conclusion was also drawn by Plate et al (1969) in a study of a highly disturbed boundary layer. For the spectrum form in the inertial subrange one finds that

$$\frac{F(k_1)}{(\xi\nu^5)^{\frac{1}{4}}} = a\left(\frac{k_1}{k_s}\right)^{-5/3} \quad , \tag{4-14}$$

in which a appears to be a universal constant, about 0.5 ± 0.005. Lumley's (1965) argument that this constant is significantly dependent on the ratio of dissipation to production, i.e.

$$D = \frac{\xi}{-\overline{uw}\,\frac{\partial U}{\partial z}} \quad , \tag{4-15}$$

is therefore not supported by the present measurements, as is evident by comparing the values of D and a given in Table VII.

The low frequency end of the spectrum is governed by the process of energy extraction from the mean flow and depends on the local velocity field. Kolmogorov's similarity form can therefore not be expected to hold for the whole spectrum.

4.1.4 Momentum transfer - Figure 32 gives all the results of the vertical turbulent diffusivity D_z for Case I, which were calculated by the following simple relation, i.e.,

$$D_z = \frac{-\overline{uw}}{\frac{\partial U}{\partial z}} \tag{4-16}$$

which essentially bears an analogy to laminar flow. The large but systematic variations of D_z in the wall region present a particular feature of eddy structure in the roughness change flow. The possibility that D_z is constant in the outer flow is not fully shown in this calculation, but the portions of maximum values of D_z for most profiles in Fig. 32 furnish sufficient evidence that the following relation holds,

$$D_z = \alpha U_\infty \delta^* \tag{4-17}$$

in which $\alpha = 0.016$. Also, D_z decreases effectively near the outer edge, due perhaps to the intermittency of turbulent flow. However, the extent and quality of the over-all agreement was sufficiently good

to show that D_z is likely to have a strong tendency to be essentially a constant beyond the wall region and, therefore, will have only a weak dependence on local conditions such as the step change of surface roughness.

Though there is little foundation for a mixing-length theory being valid in the wall flow immediately following the step change of roughness, the mixing-length distributions, as calculated from its well-known form are given in Fig. 33 for Case I only. The systematic variation of the mixing-length distributions near the wall also indicates the change of the Karman constant K along the fetch. Thus, it is felt that a rather generalized model, such as the one proposed by Townsend (1961) and Bradshaw et al (1967), should be employed herein for a detailed discussion. From eqs. (2-32) and (2-33), a_1 and L for the stations at $x = +4$ inches and $x = +6$ inches in Case I were calculated as shown in Fig. 34 and Fig. 35. In the numerical integration of eq. (2-36), Bradshaw et al (1967) chose $a_1 = 0.15$ and an empirical function of L which gives values about twice as large as the values obtained in this study. In Fig. 36, the plot based on Townsend's (1961) definition of the dissipation length L_ξ, i.e.

$$L_\xi = \frac{(\overline{q^2})^{3/2}}{\xi} \tag{4-18}$$

gives a value which is almost exactly 15 times greater than Bradshaw's (1967) value. Though the empirical expressions Bradshaw et al (1967) chose, would not necessarily be valid in our type of flow, the definition of L and its functional form should be clearly distinguished before the exact integration of eq. (2-36) can be performed numerically.

Near the wall, the turbulent energy equation, in general, reduces to "production equals dissipation," and the mixing length ℓ_z should be identical with L by the definition of eq. (2-33). The dissipation length L_ξ as Townsend (1965) defined may be related to ℓ_z in the form of

$$\ell_z = a_1^{-3/2} L_\xi \tag{4-19}$$

A comparison of these three values for several wall distances at the downstream stations x = + 4 inches and at x = + 6 inches, can be listed in the following table:

x(in.)	z(in.)	$\ell_z = \frac{(-\overline{uw})^{1/2}}{\frac{\partial U}{\partial z}}$ (in.)	$\ell_z = a_1^{-3/2}\ell_\xi$ (in.)	$\ell_z = L$ (in.)
+4	0.049	0.018	0.025	0.018
	0.074	0.028	0.033	0.028
	0.172	0.042	0.068	0.040
	0.221	0.092	0.097	0.082
+6	0.045	0.021	0.022	0.022
	0.068	0.031	0.035	0.031
	0.091	0.065	0.066	0.065
	0.159	0.086	0.075	0.086

The agreement in these results is no surprise because it can be clearly seen in Table VII that the D values as defined in eq. (4-15) are about equal to unity. However, it certainly reflects the degree of accuracy of not only the mean velocity and turbulence measurements, but also the data deduction and analysis of one-dimensional spectra in the present investigations.

4.1.5 Mass diffusion results - Since the concentration data obtained are too limited to permit a detailed study of the diffusion behavior in the "transitory" region, investigation is mainly directed

towards the determination of a possible similarity law (e.g. Batchelor 1959, 1964, Cermak 1963), if any, for both the vertical and the horizontal concentration distributions. The effect of roughness change on this similarity law, or the self-preserving argument, can thus be illustrated. The experimental data are summarized in Table VIII.

(a) Possibility of similarity profiles - Typical examples of the measured results are given in Fig. 37 for vertical concentration distributions and are given in Fig. 38 for horizontal concentration distributions. The systematic variations of the profiles are suggestive of the existence in attempting a universal form.

Vertical concentration profiles have been non-dimensionalized by dividing the wall distance z by a length scale $\lambda(x)$ and the concentrations by C_{max}. The length scale $\lambda(x)$ was defined as the wall distance at which the local concentration has decreased to half the value at the ground level. The ground level concentration is usually the largest concentration in this experiment and is designated as C_{max}. A close look at the plot of C/C_{max} versus z/λ, as shown in Fig. 39, shows that the results appear to fit consistently the form (Poreh and Cermak 1964)

$$\frac{C}{C_{max}} = e^{-\ell n 2 (\frac{z}{\lambda})^{\gamma}} \quad , \tag{4-20}$$

with a variable exponent γ, which was found to be 1.6 for the smooth surface, 2.0 immediately after the roughness change, and 2.5 far downstream from the roughness change. These results give the degree of the effect of roughness change on the attenuation of mass concentration.

Horizontal concentration profiles have also been non-dimensionalized by the concentration scale C_{max} on the individual profile and a length scale, $\eta(x)$, which was defined as one-half of the plume-spreading width at which the concentration has decreased to one-half of the C_{max}. Results for only three profiles are shown in Fig. 40. The universality of this non-dimensional plotting appears well-established, disregarding the location of the profile. The distribution of this universal curve obviously departs from Gaussianity. Since, such departures may represent the essence of the dynamics of turbulence, it is reasonable to postulate that a density distribution of the Gram-Charlier type, as has been supported by many authors (Longuet-Higgins 1963, Frenkiel and Klebanoff 1966), will correspond considerably better to the experimental results than will the Gaussian distribution. An analysis of this phenomenon is a suggestion for future study, since more data are necessary for a conclusive answer.

(b) Similarity parameters - The data given in Table VIII have been plotted and meshed into a form of iso-concentration contours on the y-z plane for each downstream distance, in order that the maximum concentration, C_{max} can be accurately estimated to test Batchelor's similarity hypothesis, (i.e. eq. (2-41)). The logarithmic plot of these C_{max} versus x as shown in Fig. 41 represent, in general, such an attenuation with

$$C_{max}\,(\bar{x},\ 0,\ 0) \propto x^{-1.7} \quad . \tag{4-21}$$

Departure from the above relation at those stations immediately downstream of the roughness change is associated with disturbances in the mean flow. Interestingly enough, experimental evidence indicates

that the attenuation of C_{max} over the rough surface appears to be not decidedly larger than that over the smooth surface.

The two length scales $\lambda(x)$ and $\eta(x)$ as plotted against x are shown in Fig. 42. This plot presents a rapid diffusion of vertical concentration distribution as the plume approaches the step change of roughness. The values of $\lambda(x)$ and $\eta(x)$ increase approximately according to a power law of the form $x^{0.9}$, which is close to the results attained by Malhotra and Cermak (1963) along a smooth flat plate without any disturbance. Here, is also noticeable that the lateral mixing, which is stronger than the vertical mixing over the rough surface, is more dominate at the beginning of the roughness change than at the far downstream station.

4.2 Application of Results to Theoretical Models

4.2.1 Development of internal boundary layer - On approaching the rough surface, the flow is immediately modified because of the increasing wall shear stress. Since the rate of production of turbulent energy in the boundary layer upstream is $-\overline{uw}\ \partial U/\partial z$, and the kinetic energy of the turbulent motion is $1/2\ \overline{q^2}$, both per unit of mass, the turbulent energy of a fluid parcel entering a region of changed rate-of-strain cannot change appreciably in a time much less than

$$t = \frac{\frac{1}{2}\overline{q^2}}{-\overline{uw}\,\frac{\partial U}{\partial z}} \quad . \tag{4-22}$$

In this time, the mean flow will move the parcel a distance

$$x = \left(\frac{\frac{1}{2}\overline{q^2}}{-\overline{uw}\,\frac{\partial U}{\partial z}} \right) U(z) \quad . \tag{4-23}$$

Turbulent energy and Reynolds stress are almost unchanged along streamlines well above the critical surface (see Townsend 1965a) defined by eq. (4-23). It follows that the stress gradient has the same value as that which exists far upstream. Flow acceleration is therefore negligible and the mean velocity remains constant along streamlines far above the critical surface, and, probably the only modification caused by the change of surface roughness is a vertical displacement of streamlines.

Based on this argument, such a critical surface can be calculated from the turbulence measurements rather than from any assumption on the equilibrium relations, such as the one used by Panofsky and Townsend (1964). Since the influence of the change of roughness could begin anywhere near $x = 0$, tentatively, we chose the origin at $x = -4$ inches; thus, only the data collected at $x = -4$ inches was used for the following calculations.

z (in.)	U (fps)	$\overline{q^2}=\overline{u^2}+\overline{v^2}+\overline{w^2}$ $(fps)^2$	$-\overline{uw}\,\frac{\partial U}{\partial z}$ (ft^2/sec^3)	$x=\left(\frac{\frac{1}{2}\overline{q^2}}{-\overline{uw}\,\frac{\partial U}{\partial z}}\right)U$ (in.)
0.188	12.30	9.51	101.80	6.9
0.250	12.85	9.08	68.70	10.2
0.500	14.58	7.24	47.20	13.4
0.625	15.30	6.44	34.45	17.2
0.875	16.35	5.91	20.50	24.6
1.250	17.60	4.49	9.56	49.7
1.500	18.36	3.71	5.32	63.8

The results are plotted in Fig. 43. Although a linear relationship cannot be well established from these results, we can say, roughly, the critical surface corresponds to a ratio of height and fetch which on the order of 1/25.

The wind-tunnel study makes possible measurements up to the free stream, which could hardly be performed in a field study. Since the effect of roughness change is assumed to be confined to the "internal boundary layer" with a thickness $d(x)$, and the flow outside of $d(x)$ is "undisturbed" and dependent on the wall shear stress upstream of the discontinuity, it is postulated that a velocity defect law of the form

$$\frac{U_\infty - U}{U_{*\text{at } x=-4 \text{ in.}}} = A_1 \ln \frac{z}{\delta} + B_1 \qquad (4\text{-}24)$$

should be applicable for the flow outside of $d(x)$. A plot of $(U_\infty - U)/U_{*\text{at } x=-4 \text{ in.}}$ versus z/δ, as has been made by others (Clauser 1956), is shown in Fig. 44. From this plot we can clearly see that the portion of the universal defect profile becomes less and less as the downstream distance increases. It is thus assumed that the "knee" point on this plot may be used to define the edge $d(x)$. A rough estimate of $d(x)$ as defined in this fashion is also plotted in Fig. 43, in comparison with the calculated critical surface based on the time required for the adjustment of Reynolds stress. The slope of the internal boundary layer appears to be of the order of 1/13, which is close to the order of 1/10, as given by Elliott (1958) and Panofsky and Townsend (1964). It is interesting to note that Antonia and Luxton (1968), based on the U versus $z^{\frac{1}{2}}$ plot, found that the internal layer grows in the manner of a two-dimensional wake, i.e. as $x^{0.5}$.

From the evidence shown in Fig. 43, we are inclined to draw a significant conclusion that the effect of roughness change on the mean flow is much greater than that on the turbulence.

4.2.2 Mean velocity distributions compared with Nickerson's Model - Numerical computations based on Nickerson's original scheme (1968) were carried out on CDC 6400 at the CSU computing facility for the three experimental cases. The selected values for the roughness lengths upwind and downwind of the roughness discontinuity were: $z_1 = 4.08 \times 10^{-4}$ in. and $z_o = 3.06 \times 10^{-2}$ in. for Case I, $z_1 = 3.80 \times 10^{-4}$ in. and $z_o = 1.10 \times 10^{-2}$ in. for Case II, and $z_1 = 1.40 \times 10^{-4}$ in. and $z_o = 6.00 \times 10^{-4}$ in. for Case III. The initial shear velocity involved in the computations is $U_{*1} = 0.77$ fps. for Case I, $U_{*1} = 0.79$ fps. for Case II and $U_{*1} = 1.17$ fps. for Case III. For clarity, the results shown in Figs. 45, 46, 47 for the Cases I, II, and III respectively, were compared with the experimental data only at a few selected stations.

It was found that large discrepancy between the observational and numerical results for Cases I and II occurs immediately downstream of the roughness discontinuity but that the differences become less as the fetch becomes large only for Case I. However, in Case III, the experimental wind profiles agree quite well with the numerical calculations up to about $x = 6$ in.. Sizable discrepancy at the larger fetch are perhaps due to an inadequate treatment of the lower boundary conditions in the numerical model. Further quantitative comparison with Mr. Huang's (Dr. Nickerson's Ph.D. student at CSU) numerical model, in which the pressure term is retained in the governing equations, does not give any significant improvement for all the cases. Thus, it may be concluded that the current numerical techniques are sufficient to simulate the air flow near the boundary for a small roughness change. Further experimental investigation

is required to determine the exact influence of the important parameters, such as Karman constant and the roughness length. Local dynamically-produced pressure gradients for large roughness changes will have to be included in current numerical model in order to extend the usefulness of those models.

Chapter V

CONCLUSIONS

The following conclusions regarding the effect of a sudden increase in surface roughness on a fully developed turbulent boundary layer can be drawn from the experimental results of this investigation. For clarity the conclusions are summarized into three categories:

5.1 Mean Velocity Field

1. Because of the presence of the vertical component of mean velocity, velocity distributions in the "transtory" region cannot be calculated exactly from the Reynold equations with boundary layer assumptions.

2. The internal boundary layer grows with a ratio of heights and downstream distance of order 1/13. Observations show that the origin of the internal boundary layer should start approximately one boundary layer thickness upstream from the roughness discontinuity. The logarithmic profile in the conventional form cannot fully describe the wall flow in the "transitory" region.

3. The fluid near the wall is accelerated in front of the roughness discontinuity and retarded behind it. The maxima in the mean velocity in the transitory region occurs farther downstream with increasing distance from the wall.

4. Values of velocity gradient and wall shear stress in the "transitory" region exceed those values attained far downstream.

5. Numerical techniques, such as those developed by Nickerson (1968) prove to be sufficient in modeling non-uniform wall flows for a small roughness change. More experimental investigations are

required to determine the role of the Karman constant and the roughness length hypothesis and the logarithmic wind profile. The numerical integration of a transformed energy equation by Bradshaw et al (1967) should be of value if more experimental information is provided.

5.2 Turbulence Field

1. Mixing-length (distribution in the "transitory" region is not consistent with that established for fully developed turbulent boundary layer. The more complicated models, such as those proposed by Townsend (1961) and Bradshaw et al (1967) appear reasonable if the three empirical functions they defined can be well established.

2. Eddy diffusivity as calculated is likely to have a strong tendency to become constant beyond the wall region, and, therefore, will have only a weak dependence on local conditions.

3. Turbulence intensities and Reynolds stress in the "transitory" region are unchanged along streamlines well above a critical surface, which grows with a ratio of height and fetch approximately 1/25. This slower rate of development in comparison with that of the internal boundary layer (i.e. 1/13) demonstrates that even when the mean velocity has adjusted to a new logarithmic profile, the flow is not necessarily in an equilibrium condition.

4. The high frequency end of the spectra in the "transitory" region can be exactly represented by the high frequency shape of the undisturbed turbulence in a boundary layer along a flat plate.

5.3 Mass Transfer

1. Self-preserving concentration profile is in general possible for both the vertical and the horizontal distributions. A look at the

results show that self-preserving forms with an exponent that differs slightly exist both upstream and downstream of the roughness discontinuity.

2. Lateral mixing is stronger than vertical mixing. Attentuation of the ground level concentration appears to be unaffected by the roughness difference.

REFERENCES

REFERENCES

Antonia, R. A. and R. E. Luxton (1968), "The response of a turbulent boundary layer to a step change in surface roughness," Dept. of Mech. Engr., Univ. of Sydney, Australia.

Batchelor, G. K. (1959), "Some reflections on the theoretical problems raised at the symposium," Adv. Geophys., 6, 449-452.

Batchelor, G. K. (1964), "Diffusion from sources in a turbulent boundary layer," Archiwum Mechaniki Stosowanej, 3, 661-670.

Blom, J. and L. Wartena (1969), "The influence of changes in surface roughness on the development of the turbulent boundary layer in the lower layer of the atmosphere," J. Atmos. Sci., 26, 255.

Bradshaw, P., D. H. Ferriss and N. P. Atwell (1966), "Calculation of boundary-layer development using the turbulent energy equation," NPL Aero. Report 1182, also J. Fluid Mech. 28, 593-617.

Bradshaw, P. (1967a), "The turbulent structure of equilibrium boundary layer," J. Fluid Mech. 29, 625.

Bradshaw, P. (1967b), "Inactive motion and pressure fluctuations in turbulent boundary layer," J. Fluid Mech. 30, 241.

Chao, J. L. and V. A. Sandborn (1965), "Study of static pressure along a rough boundary," Proceedings of ASCE, Vol. 91, HY 2, 4269.

Cermak, J. E. (1963), "Lagrangian similarity hypothesis applied to diffusion in turbulent shear flow," J. Fluid Mech. 15, 49-64.

Champagne, F. H., C. A. Sleicher and O. H. Wehrmann (1967a), "Turbulence measurements with inclined hot wires, Part I: Heat transfer experiments with inclined hot wire," J. Fluid Mech. 28, 153-175.

Champagne, F. H. and C. A. Sleicher (1967b), "Turbulence measurements with inclined hot wires, Part II: Hot-wire response equations," J. Fluid Mech. 28, 177-182.

Chowdhury, S. (1966), "Turbulent eddies in boundary layers on smooth and rough flat plate," CER65SC-EJP57, Colorado State Univ., Ft. Collins, Colorado

Clauser, F. H. (1956), "The turbulent boundary layer," Adv. in Applied Mech. 4, Academic Press, N. Y.

Coles, D. E. (1956), "The law of the wake in the turbulent boundary layer," J. Fluid Mech., 1, 191.

Elliott, W. P. (1958), "The growth of the atmospheric internal boundary layer," Trans. Amer. Geophys. Union, 39, 1048-1054.

REFERENCES - Continued

Ellison, T. H. (1956), "Atmospheric turbulence," Surveys in Mechanics, Cambridge Univ. Press, N. Y.

Finn, C. L. and V. A. Sandborn (1967), "The design of a constant temperature hot wire anemometer," TR CER66-67CLF36, Colorado State University, Ft. Collins, Colorado.

Hama, F. R. (1954), "Boundary layer characteristics for smooth and rough surface," Annual meeting of the Soc. of Naval Architects and Marine Engrs., p. 333.

Heisenberg, W. (1948), "On the theory of statistical and isotropic turbulence," Proc. Royal Soc. (London), Series A, 195, 402-406.

Hino, M. (1965, 1967a, 1967b), "Numerical analysis of smoke diffusion under the effects of topography," Part I (1965), Part II (1967), Part III (1967), Tech. Report, Central Research Institute of Electric Power Industry, Tokyo, Japan.

Hinze, J. O. (1959), "Turbulence," McGraw Hill, N. Y.

Jacob, W. (1939), "Umformung eines turbulenten geschwindigkeits profils," Zietschrift fur Augewandte Mathematik und Mechanik, 87-100, Translation, NACA TM 951 (1940).

Klebanoff, P. S. and F. N. Frenkiel (1967), "Higher-order correlations in a turbulent field," Phys. Fluids, 10, 507.

Kline, S. J., W. C. Reynolds, F. A. Schraub and P. W. Runstadler (1967), "The structure of turbulent boundary layers," J. Fluid Mech., 30, 741-773.

Lettau, H. H. (1962), "Studies of the three-dimensional structure of the planetary boundary layer," Annual Report DA36-039-SC-80282, U.S. Army Electronic Proving Ground.

Logan, E. and J. B. Jones (1963), "Flow in a pipe following an abrupt increase in surface roughness," J. Basic Engr., ASME Trans., 35-40.

Longuet-Higgins, M. S. (1963), "The effect of non-linearities on statistical distributions in the theory of sea waves," J. Fluid Mech. 17, 459.

Margolis, D. P. and J. L. Lumley (1965), "Curved turbulent mixing layer," Phys. Fluids, 8, 1775.

Malhotra, R. C. and J. E. Cermak (1964), "Mass diffusion in neutral and unstably stratified boundary layer flows," International J. of Heat and Mass Transfer, 7, 169-186.

REFERENCES - Continued

Meroney, R. N., D. Kesic and T. Yamada (1968), "Gaseous plume diffusion characteristics within model peg canopies," TR CER68-69RNM-DK-TY-3, Colorado State University, Ft. Collins, Colorado.

Nickerson, E. C. (1968), "Boundary layer adjustment as an initial-value problem," J. Atm. Sci., 25, 207-213.

Onishi, G. (1966), "A two-dimensional steady state numerical model of atmospheric boundary layer flow over inhomogeneous terrain," Final Report, Part II. Hawaii Institute of Geophysics, Univ. of Hawaii.

Panofsky, H. A. and A. A. Townsend (1964), "Change of terrain roughness and the wind profile," Q. J. Roy. Met. Soc., 90, 147.

Perry, A. E. and P. N. Joubert (1963), "Rough-wall boundary layers in adverse pressure gradients," J. Fluid Mech., 17, 195.

Perry, A. E., W. H. Schofield and P. N. Joubert (1969), "Rough wall turbulent boundary layer," J. Fluid Mech., 37, 383.

Plate, E. J. and C. M. Sheih (1965), "Diffusion from a continuous point source into the boundary layer downstream from a model hill," TR CER65EJP-CMS60, Colorado State University, Ft. Collins, Colorado.

Plate, E. J. and G. M. Hidy (1967), "Laboratory study of air flowing over a smooth surface onto small water wave," J. Geophys. Res., 72, No. 18, 4627.

Plate, E. J., F. F. Yeh and R. J. Kung (1969), "Approximate joint probability distributions of the turbulence along a hypothetical missile trajectory downstream of a sinusoidal model ridge," TR CER68-69EJP-FY-RK-4, Colorado State University, Ft. Collins, Colo.

Poreh, M. and J. E. Cermak (1964), "Study of diffusion from a line source in a turbulent boundary layer," Int. J. Heat Mass Transfer, 7, 1083-1095.

Richtmyer, R. D. (1957), "Difference methods for initial-value problems," Interscience Publishers, N. Y.

Rider, N. E., J. R. Philip and E. F. Bradley (1963), "The horizontal transport of heat and moisture - a micrometeorological study," Q. J. Roy. Met. Soc., 89, 507-531.

Rotta, J. C. (1962), "Turbulent boundary layers in incompressible flow," Prog. Aero. Sci., 2, Ferri-Pergamon, N. Y.

Schlichting, H. (1960), "Boundary layer theory," 4th ed., McGraw-Hill, N.Y.

Taylor, P. A. (1967), "On turbulent wall flows above a change in surface roughness," ph. D. dissertation, Univ. of Bristol, Canada.

REFERENCES - Continued

Taylor, R. J. (1962), "Small-scale advection and the neutral wind profile," J. Fluid Mech., 13, 529.

Tchen, C. M. (1953), "On the spectrum of energy in turbulent shear flow," J. Res. Nat. Bur. Standards, 50, 51-62.

Tieleman, H. W. (1967), "Viscous region of turbulent boundary layer," TR, CER67-68HWT21, Colorado State University, Fort Collins, Colo.

Townsend, A. A. (1961), "Equilibrium layers and wall turbulence," J. Fluid Mech., 11, 97-120.

Townsend, A. A. (1965a), "Self-preserving flow inside a turbulent boundary layer," J. Fluid Mech., 22, 773-797.

Townsend, A. A. (1965b), "The response of a turbulent boundary layer to abrupt changes in surface conditions," J. Fluid Mech., 22, 799-822.

Townsend, A. A. (1966), "The flow in a turbulent boundary layer after a change in surface roughness," J. Fluid Mech., 26, 255.

Wagner, N. K. (1966), "A two-dimensional time dependent numerical model of atmospheric boundary layer flow over inhomogeneous terrain," Final Report, Part I, Hawaii Institute of Geophysics, Univ. of Hawaii.

Yamamoto, G. and A. Shimanaki (1964), "The determination of lateral diffusivity in diabatic conditions near the ground from diffusion experiment," J. Atm. Sci., 21, 187-195.

APPENDIX I

Appendix I

Derivation of Eq. (2-9)

From vorticity transport equation (Schlichting 1960)

$$\frac{\partial \nabla^2 \psi}{\partial t} + \frac{\partial \psi}{\partial z}\frac{\partial \nabla^2 \psi}{\partial x} - \frac{\partial \psi}{\partial x}\frac{\partial \nabla^2 \psi}{\partial z} = \nu \nabla^4 \psi \tag{A-1}$$

Let us consider no viscous terms and imagine a two-dimensional mean flow, such that $\overline{U} = \overline{U}(z)$ and $\overline{w} = \overline{w}(x)$, and $\psi(x,z) = \psi(x,z) + \psi'(x,z)$

$$\frac{\partial(\nabla^2\psi\ \nabla^2\psi')}{\partial t} + (\overline{U} + \frac{\partial \psi'}{\partial z})(\frac{\partial \nabla^2 \psi'}{\partial x} - \frac{d^2\overline{w}}{dx^2}) + (\overline{w} - \frac{\partial \psi'}{\partial x})(\frac{d^2\overline{U}}{dz^2} + \frac{\partial \nabla^2 \psi'}{\partial z}) = 0 \tag{A-2}$$

where

$$\frac{\partial \nabla^2 \psi}{\partial x} = \frac{\partial}{\partial x}(-\frac{\partial \overline{w}}{\partial x} + \frac{\partial \overline{U}}{\partial z} + \nabla^2 \psi') = -\frac{d^2\overline{w}}{dx^2} + \frac{\partial \nabla^2 \psi'}{\partial x} \tag{A-3}$$

and

$$\frac{\partial \nabla^2 \psi}{\partial z} = \frac{d^2\overline{U}}{dz^2} + \frac{\partial \nabla^2 \psi'}{\partial z} \quad . \tag{A-4}$$

The mean flow will now be expanded in a Taylor's series in the neighborhood of a point (x_o, z_o), so that

$$\overline{U} = \overline{U}_o + (\frac{d\overline{U}}{dz})_o (z-z_o) + \frac{1}{2}(\frac{d^2\overline{U}}{dz^2})_o (z-z_o)^2 + \tag{A-5}$$

$$\overline{w} = \overline{w}_o + (\frac{d\overline{w}}{dx})_o (x-x_o) + \frac{1}{2}(\frac{d^2\overline{w}}{dx^2})_o (x-x_o)^2 + \quad . \tag{A-6}$$

Furthermore, introduce a system of co-ordinates moving with a velocity $\bar{U}_o$ and $\bar{w}_o$, and assume a steady motion, so that

$$(z-z_o)\left(\frac{d\bar{U}}{dz}\right)_o\left[\frac{\partial\nabla^2\psi'}{\partial x} - \left(\frac{d^2\bar{w}}{dx^2}\right)_o\right] + \frac{\partial\psi'}{\partial z}\left[\frac{\partial\nabla^2\psi'}{\partial x} - \left(\frac{d^2\bar{w}}{dx^2}\right)_o\right]$$

$$+ (x-x_o)\left(\frac{d\bar{w}}{dx}\right)_o\left[\left(\frac{d^2\bar{U}}{dz^2}\right)_o + \frac{\partial\nabla^2\psi'}{\partial z}\right] - \frac{\partial\psi'}{\partial x}\left[\left(\frac{d^2\bar{U}}{dz^2}\right)_o + \frac{\partial\nabla^2\psi'}{\partial z}\right] = 0 \qquad \text{(A-7)}$$

By similarity hypothesis, assume a length scale ℓ and a velocity scale B at point (x_o, z_o), and introduce

$$x - x_o = \ell\xi \qquad \text{(A-8)}$$

$$z - z_o = \ell\eta \qquad \text{(A-9)}$$

$$\psi' = B\ell f(\xi,\eta) \qquad \text{(A-10)}$$

Eq. (A-9) then becomes

$$\frac{B}{\ell}\eta\left(\frac{d\bar{U}}{dz}\right)_o\left[\frac{\partial\nabla^2 f}{\partial\xi} - \left(\frac{d^2\bar{w}}{dx^2}\right)_o\right] + B\frac{\partial f}{\partial\eta}\left[\frac{B}{\ell^2}\frac{\partial\nabla^2 f}{\partial\xi} - \left(\frac{d^2\bar{w}}{dx^2}\right)_o\right]$$

$$+ \frac{B}{\ell}\xi\left(\frac{d\bar{w}}{dx}\right)_o\left[\left(\frac{d^2\bar{U}}{dz^2}\right)_o + \frac{\partial\nabla^2 f}{\partial\eta}\right] - B\frac{\partial f}{\partial\xi}\left[\left(\frac{d^2\bar{U}}{dz^2}\right)_o + \frac{B}{\ell^2}\frac{\partial\nabla^2 f}{\partial\eta}\right] = 0 . \qquad \text{(A-11)}$$

If eq. (A-11) is divided through by $B/\ell\,(d\bar{U}/dz)_o$, then

$$\eta\frac{\partial\nabla^2 f}{\partial\xi} + \frac{\left(\frac{d\bar{w}}{dx}\right)_o}{\left(\frac{d\bar{U}}{dz}\right)_o}\xi\frac{\partial\nabla^2 f}{\partial\eta} + \frac{\ell\left(\frac{d^2\bar{w}}{dx^2}\right)_o}{\left(\frac{d\bar{U}}{dz}\right)_o}\frac{\partial f}{\partial\eta} - \frac{\ell\left(\frac{d^2\bar{w}}{dz^2}\right)_o}{\left(\frac{d\bar{U}}{dz}\right)_o}\frac{\partial f}{\partial\xi}$$

$$+ \frac{B}{\ell\left(\frac{d\bar{U}}{dz}\right)_o}\left[\frac{\partial f}{\partial \eta}\frac{\partial \nabla^2 f}{\partial \xi} - \frac{\partial f}{\partial \xi}\frac{\partial \nabla^2 f}{\partial \eta}\right] - \eta\left(\frac{d^2\bar{w}}{dx^2}\right)_o + \xi\frac{\left(\frac{d\bar{w}}{dx}\right)_o}{\left(\frac{d\bar{U}}{dz}\right)_o}\left(\frac{d^2\bar{U}}{dz^2}\right)_o = 0 \qquad \text{(A-12)}$$

from which the similarity hypothesis will require

$$\frac{\ell\left(\frac{d^2\bar{w}}{dz^2}\right)_o}{\left(\frac{d\bar{U}}{dz}\right)_o} = \text{const} \quad , \quad \frac{\ell\left(\frac{d^2\bar{U}}{dz^2}\right)_o}{\left(\frac{d\bar{U}}{dz}\right)_o} = K \text{ (Karman Const)}$$

$$\frac{B}{\ell\left(\frac{d\bar{U}}{dz}\right)_o} = \text{const}$$

thus,

$$K = \text{const} \left| \frac{\frac{d\bar{U}}{dz}}{\frac{d^2\bar{w}}{dx^2}} \right| \left| \frac{\frac{d^2\bar{U}}{dz^2}}{\frac{d\bar{U}}{dz}} \right| . \qquad \text{(A-13)}$$

APPENDIX II

TABLES

Table 1. Mean Velocity Data for Case I

U_∞ = 20 fps

x = -24 in.		x = -12 in.		x = -6 in.		x = -4 in.		x = -2 in.		x = 0 in.	
z (in.)	U (fps)	z (in.)	U (fps)	z (in.)	U (fps)	z (in.)	U (fps)	z (in.)	U (fps)	z (in.)	U (fps)
0.063	11.20	0.063	11.20	0.063	10.80	0.063	10.60	0.063	10.20	0.125	13.77
0.095	12.20	0.094	11.45	0.125	12.28	0.125	12.20	0.125	11.70	0.188	13.82
0.125	12.50	0.125	12.10	0.188	12.37	0.188	12.30	0.188	11.88	0.250	14.04
0.156	13.10	0.250	13.66	0.250	13.01	0.250	12.85	0.250	12.53	0.375	14.58
0.188	13.50	0.375	14.40	0.375	14.15	0.313	13.25	0.313	12.85	0.500	15.17
0.250	14.10	0.438	14.80	0.500	14.90	0.375	14.00	0.375	13.45	0.750	16.25
0.375	15.00	0.500	15.20	0.625	15.55	0.500	14.58	0.500	14.26	1.000	17.06
0.500	15.80	0.625	15.90	0.875	16.63	0.625	15.30	0.625	14.90	1.375	18.15
0.625	16.50	0.750	16.40	1.125	17.55	0.688	15.65	0.688	15.30	1.875	19.17
0.875	17.50	0.875	16.90	1.500	18.58	0.875	16.35	0.875	16.00	2.344	19.66
1.125	18.35	1.125	17.70	2.000	19.33	1.125	17.33	1.000	16.37		
1.750	19.30	1.188	17.98	2.469	19.60	1.250	17.60	1.125	16.85		
2.250	19.90	1.625	18.80			1.500	18.36	1.250	17.50		
		1.875	19.33			2.000	19.10	1.500	17.98		
		2.375	19.87			2.469	19.59	2.000	18.85		
								2.469	19.39		

Table 1 Continued

x = 2 in.		x = 4 in.		x = 6 in.		x = 12 in.		x = 24 in.		x = 36 in.	
z (in.)	U (fps)	z (in.)	U (fps)	z (in.)	U (fps)	z (in.)	U (fps)	z (in.)	U (fps)	z (in.)	U (fps)
0.125	10.30	0.125	8.20	0.125	5.50	0.125	7.63	0.125	6.00	0.094	5.91
0.188	11.77	0.188	9.20	0.188	6.94	0.188	8.00	0.188	6.85	0.188	7.45
0.250	12.40	0.250	10.80	0.250	9.35	0.125	9.34	0.250	7.90	0.250	8.53
0.313	13.28	0.313	11.76	0.313	10.80	0.313	10.10	0.313	8.70	0.313	8.85
0.438	14.60	0.438	13.55	0.438	12.85	0.438	11.45	0.438	10.00	0.438	10.10
0.563	15.34	0.563	15.10	0.625	15.10	0.625	13.55	0.625	12.10	0.625	11.42
0.625	15.80	0.625	15.45	0.750	15.80	0.875	15.30	0.750	13.55	0.875	12.78
0.750	16.25	0.750	16.00	0.875	16.75	1.375	17.60	0.875	13.78	1.375	15.65
1.000	17.20	1.000	17.00	1.000	16.90	1.875	18.70	1.000	15.00	2.000	17.90
1.250	17.82	1.250	17.80	1.375	17.90	2.625	19.55	1.375	16.75	2.750	19.32
1.500	18.45	1.500	18.60	1.500	18.35			1.500	17.40		
1.750	19.10	1.750	19.00	1.875	18.95			1.875	18.05		
2.000	19.55	2.000	19.45	2.000	19.15			2.250	19.30		
2.500	19.76	2.500	19.75	2.625	19.70			2.625	19.32		

Table II. Mean Velocity Data for Case II

U_∞ = 20 fps

x = -6 in.		x = -4 in.		x = -2 in.		x = 0 in.		x = 1 in.		x = 2 in.		x = 3 in.		x = 4 in.	
z (in.)	U (fps)	z (in.)	U (fps)	z (in.)	U (fps)	z (in.)	U (fps)	z (in.)	U (fps)	z (in.)	U (fps)	z (in.)	U (fps)	z (in.)	U (fps)
0.063	10.66	0.063	9.96	0.063	10.39	0.096	10.68	0.106	10.66	0.111	10.18	0.109	8.41	0.124	9.00
0.108	11.02	0.088	10.42	0.095	10.50	0.123	10.77	0.134	11.32	0.143	10.74	0.132	8.87	0.138	9.62
0.141	11.35	0.110	10.78	0.108	10.80	0.145	10.93	0.176	12.01	0.172	11.18	0.186	9.96	0.156	10.07
0.172	11.82	0.137	11.20	0.135	11.06	0.226	12.08	0.234	12.38	0.196	11.45	0.247	12.08	0.244	11.45
0.256	12.78	0.194	12.01	0.197	11.95	0.344	13.11	0.320	12.90	0.245	12.66	0.356	12.90	0.326	12.31
0.338	13.55	0.264	12.67	0.255	12.38	0.487	13.98	0.475	13.88	0.373	13.33	0.418	13.67	0.431	13.22
0.471	14.29	0.355	13.44	0.358	13.33	0.775	15.37	0.603	14.49	0.491	14.19	0.546	14.49	0.522	14.09
0.635	14.98	0.537	14.33	0.536	14.40	1.215	17.08	0.705	15.18	0.613	14.57	0.694	15.19	0.648	14.70
0.897	16.32	0.835	15.55	0.794	15.56	1.667	18.20	0.907	15.65	0.775	15.18	0.837	15.83	0.758	15.18
1.125	17.06	1.172	17.08	1.090	16.81	2.250	19.25	1.092	16.64	1.015	16.55	1.153	16.63	0.879	15.94
1.345	17.90	1.388	17.80	1.311	17.70			1.472	17.90	1.252	17.50	1.498	17.74	1.156	17.00
1.998	19.14	1.820	18.78	1.464	18.15			1.989	18.70	1.656	18.22	2.027	18.80	1.597	18.08
2.422	19.32	2.110	19.10	2.805	19.25			2.515	19.47	2.152	19.10	2.398	19.25	2.080	18.94
										2.561	19.43	2.611	19.47	2.523	19.39

Table II. Continued

x = 6 in.		x = 8 in.		x = 10 in.		x = 12 in.		x = 15 in.		x = 18 in.		x = 24 in.	
z (in.)	U (fps)	z (in.)	U (fps)	z (in.)	U (fps)	z (in.)	U (fps)	z (in.)	U (fps)	z (in.)	U (fps)	z (in.)	U (fps)
0.110	8.19	0.129	7.44	0.121	7.12	0.130	7.37	0.103	6.73	0.135	6.40	0.110	6.16
0.153	9.04	0.162	8.71	0.158	8.16	0.172	8.54	0.146	7.72	0.158	6.84	0.159	7.04
0.211	10.39	0.213	9.56	0.175	8.54	0.200	9.35	0.177	8.36	0.215	8.19	0.258	8.20
0.294	11.43	0.247	9.96	0.227	9.81	0.290	10.53	0.250	9.58	0.313	8.87	0.370	9.35
0.374	12.31	0.349	11.32	0.329	10.80	0.412	11.32	0.298	9.96	0.435	10.66	0.492	10.61
0.467	13.33	0.487	12.81	0.480	12.20	0.502	12.89	0.407	11.45	0.580	12.20	0.620	11.45
0.595	14.19	0.600	13.77	0.650	13.77	0.652	13.66	0.640	13.00	0.775	13.55	0.781	12.95
0.868	15.56	0.780	15.00	0.787	14.65	0.806	14.29	0.876	14.40	1.131	15.55	0.920	13.77
1.171	16.81	0.914	15.73	0.934	15.55	0.995	15.40	1.022	15.18	1.717	17.58	1.402	17.00
1.675	18.08	1.257	16.81	1.340	17.16	1.295	16.90	1.508	16.90	2.288	18.62	2.095	18.22
2.340	19.01	1.660	17.90	1.786	18.22	1.605	17.50	2.017	18.55	2.939	19.31	3.085	19.40
2.778	19.48	2.175	18.85	2.655	19.55	2.159	18.93	3.038	19.46				
		2.719	19.47			2.753	19.55						

Table III. Mean Velocity Data for Case III

U_∞ = 30 fps

x = -6 in.		x = -4 in.		x = -2 in.		x = 0 in.		x = 1 in.		x = 3 in.		x = 4 in.		x = 6 in.		x = 10 in.		x = 14 in.	
z (in.)	U (fps)	z (in.)	U (fps)	z (in.)	U (fps)	z (in.)	U (fps)	z (in.)	U (fps)	z (in.)	U (fps)	z (in.)	U (fps)	z (in.)	U (fps)	z (in.)	U (fps)	z (in.)	U (fps)
0.079	18.61	0.068	18.31	0.058	17.91	0.134	19.91	0.146	19.28	0.097	17.79	0.080	17.83	0.089	17.41	0.081	16.86	0.078	16.86
0.112	19.94	0.084	19.09	0.074	18.90	0.178	20.13	0.163	19.32	0.152	19.84	0.167	19.84	0.140	18.03	0.162	18.31	0.130	17.29
0.129	20.38	0.128	20.02	0.122	19.84	0.243	21.43	0.190	19.95	0.224	21.09	0.244	21.33	0.198	19.09	0.196	19.47	0.210	19.09
0.134	20.38	0.166	20.74	0.302	22.43	0.281	22.07	0.249	20.84	0.288	22.10	0.356	22.53	0.280	20.91	0.267	20.91	0.308	20.63
0.173	20.81	0.220	21.70	0.529	24.30	0.346	22.91	0.298	21.77	0.474	23.69	0.487	23.69	0.388	22.43	0.381	22.43	0.439	22.17
0.189	21.43	0.313	22.75	0.825	25.76	0.411	23.54	0.373	22.59	0.575	24.45	0.584	24.15	0.567	24.06	0.491	23.38	0.565	23.54
0.252	22.26	0.438	23.75	1.296	27.67	0.500	24.09	0.444	23.23	0.676	25.13	0.733	25.18	0.636	24.45	0.554	23.91	0.741	24.83
0.371	23.63	0.568	24.60	1.843	28.83	0.584	24.75	0.510	23.75	1.095	27.00	0.925	26.04	0.717	24.89	0.759	25.18	0.899	25.56
0.475	24.45	0.915	26.45	2.288	29.20	0.692	25.39	0.574	24.24	1.371	27.93	1.439	27.13	0.868	25.70	0.968	26.12	1.155	26.59
0.542	24.89	1.472	28.19	2.869	29.50	0.912	26.37	0.713	25.33	1.633	28.57	1.524	28.14	1.037	26.59	1.227	27.13	1.437	27.53
0.999	27.00	2.126	29.20	3.459	29.55	1.256	27.67	0.879	26.04	1.944	28.95	1.791	28.57	1.272	27.27	1.459	27.80	1.710	28.32
1.322	27.93	2.702	29.53			1.735	28.65	1.126	27.00	2.264	29.28	2.131	29.13	1.455	27.80	1.727	28.57	2.004	28.70
1.651	28.70	3.835	29.58			2.334	29.33	1.431	27.80	2.464	29.53	2.500	29.45	1.793	28.45	2.038	28.95	2.309	29.25
2.153	29.45					2.901	29.53	1.731	28.55	2.801	29.63	2.660	29.68	2.202	29.20	2.334	29.25	2.535	29.58
						3.770	29.58	2.027	29.08	2.924	29.72	3.059	29.82	2.647	29.63	2.602	29.68	2.896	29.82
								2.329	29.33	3.235	29.92	3.309	29.97	3.011	29.72	2.991	29.72	3.262	29.97
								2.844	29.55					3.252	29.87	3.279	29.82		
								3.187	29.58										
								3.766	29.65										

Table III. Continued

x = 18 in.		x = 22 in.		x = 28 in.		x = 34 in.		x = 40 in.		x = 48 in.		x = 54 in.		x = 60 in.		x = 66 in.		x = 72 in.	
z (in.)	U (fps)	z (in.)	U (fps)	z (in.)	U (fps)	z (in.)	U (fps)	z (in.)	U (fps)	z (in.)	U (fps)	z (in.)	U (fps)	z (in.)	U (fps)	z (in.)	U (fps)	z (in.)	U (fps)
0.051	16.73	0.032	16.42	0.068	16.42	0.093	16.73	0.072	15.97	0.078	15.84	0.129	17.03	0.075	15.97	0.072	15.03	0.095	16.06
0.097	17.20	0.086	16.99	0.084	16.47	0.120	17.50	0.132	16.51	0.125	16.69	0.156	17.50	0.112	16.95	0.143	17.08	0.174	17.37
0.139	18.11	0.107	17.50	0.112	16.86	0.169	18.31	0.223	18.43	0.172	17.58	0.204	18.31	0.189	18.03	0.250	18.31	0.292	19.02
0.193	19.21	0.135	18.03	0.143	17.54	0.249	19.39	0.327	19.73	0.256	18.71	0.285	19.17	0.263	18.98	0.360	19.66	0.409	19.84
0.282	20.46	0.178	18.98	0.167	18.11	0.348	20.56	0.387	20.46	0.360	19.91	0.385	20.20	0.346	19.95	0.456	20.49	0.521	20.74
0.346	21.19	0.249	19.91	0.198	18.63	0.418	21.26	0.493	21.50	0.446	20.56	0.469	20.91	0.441	20.56	0.555	20.98	0.612	21.33
0.415	22.00	0.298	20.38	0.240	19.21	0.496	22.03	0.673	22.72	0.530	21.43	0.550	21.53	0.528	21.26	0.660	21.87	0.710	21.93
0.591	23.63	0.347	21.09	0.275	19.58	0.563	22.49	1.005	24.69	0.594	22.03	0.608	21.93	0.589	21.60	0.761	22.26	0.873	22.91
0.693	24.21	0.424	21.87	0.344	20.31	0.665	23.13	1.423	26.51	0.774	23.07	0.812	23.23	0.670	22.17	0.918	23.13	1.053	23.69
0.824	25.04	0.502	22.49	0.393	20.84	0.787	24.06	2.016	28.11	0.873	23.63	0.899	23.69	0.790	22.97	1.107	24.15	1.239	24.60
1.056	26.04	0.729	24.24	0.456	21.63	0.868	24.36	2.551	29.20	0.960	24.09	0.992	24.09	0.877	23.38	1.386	25.45	1.559	25.95
1.333	27.00	0.996	25.70	0.555	22.36	0.938	24.78	3.142	29.58	1.109	24.75	1.253	25.47	0.964	23.91	1.703	26.54	2.487	28.32
1.522	27.67	1.238	26.86	0.817	24.24	1.112	25.61	3.729	29.77	1.411	26.09	1.748	27.05	1.089	24.30	2.694	28.90	3.603	29.48
1.702	28.06	1.519	27.67	1.166	25.90	1.421	26.95	4.803	29.87	2.565	28.70	2.928	29.13	1.781	27.13	2.880	29.70	5.104	29.70
1.990	28.57	1.903	28.57	1.811	28.06	2.549	29.13			3.519	29.45	4.111	29.75	3.153	29.25	5.612	29.87		
2.315	29.08	2.252	29.08	2.287	28.88	3.688	29.72			4.593	29.70	5.668	29.80	4.240	29.70				
2.513	29.48	2.810	29.48	2.901	29.33	4.470	29.77												
2.824	29.77	3.653	29.82	3.599	29.63														
3.155	29.92	4.958	29.92	5.132	29.71														

Table IV. δ, δ^*, θ, U_* and z_o for all Cases

Case I (U_∞ = 20 fps)						Case II (U_∞ = 20 fps)						Case III (U_∞ = 30 fps)					
x (in.)	δ (in.)	δ^* (in.)	θ (in.)	U_* (fps)	z_o (in.)	x (in.)	δ (in.)	δ^* (in.)	θ (in.)	U_* (fps)	z_o (in.)	x (in.)	δ (in.)	δ^* (in.)	θ (in.)	U_* (fps)	z_o (in.)
-24	2.16	0.292	0.232	0.878	0.43×10^{-3}	-6	2.35	0.383	0.280	0.799	3.90×10^{-4}	-6	2.35	0.291	0.239	1.216	1.46×10^{-4}
-12	2.40	0.343	0.263	0.868	0.47×10^{-3}	-4	2.50	0.417	0.310	0.799	3.90×10^{-4}	-4	2.50	0.304	0.245	1.162	1.36×10^{-4}
-4	2.53	0.385	0.296	0.773	0.37×10^{-3}	-2	2.65	0.451	0.325	0.781	3.70×10^{-4}	-2	2.80	0.320	0.257	1.162	1.36×10^{-4}
-2	2.76	0.443	0.331	0.764	0.28×10^{-3}	1	2.81	0.475	0.326	0.868	8.60×10^{-4}	0	2.75	0.293	0.236	1.041	9.10×10^{-5}
0	2.48	0.503	0.429	0.368	0.40×10^{-3}	2	2.90	0.443	0.321	1.060	2.30×10^{-3}	1	2.80	0.309	0.245	1.268	3.20×10^{-4}
2	2.55	0.559	0.431	1.325	5.94×10^{-3}	4	3.00	0.483	0.339	1.494	1.16×10^{-2}	3	2.85	0.304	0.236	1.561	9.80×10^{-4}
4	2.55	0.612	0.456	2.045	3.24×10^{-2}	6	3.15	0.527	0.344	1.562	1.47×10^{-2}	4	3.15	0.318	0.250	1.458	7.40×10^{-4}
6	2.75	0.679	0.483	2.426	5.28×10^{-2}	8	3.30	0.551	0.342	1.492	1.75×10^{-2}	6	3.10	0.336	0.252	1.543	1.35×10^{-3}
12	2.87	0.731	0.521	1.650	3.38×10^{-2}	10	3.40	0.569	0.346	1.460	1.70×10^{-2}	8	3.05	0.326	0.245	1.458	8.30×10^{-4}
24	2.95	0.787	0.560	1.513	3.06×10^{-2}	12	3.45	0.602	0.370	1.390	1.45×10^{-2}	10	3.10	0.337	0.257	1.492	1.02×10^{-3}
36	3.14	0.924	0.626	1.510	2.28×10^{-2}	15	3.50	0.635	0.387	1.354	1.37×10^{-2}	14	3.15	0.353	0.265	1.475	1.20×10^{-3}
						18	3.55	0.681	0.403	1.216	1.62×10^{-2}	18	3.20	0.364	0.271	1.353	6.80×10^{-4}
						24	3.60	0.730	0.420	1.042	1.10×10^{-2}	22	3.25	0.371	0.282	1.145	2.60×10^{-4}
												28	3.35	0.412	0.315	1.266	6.00×10^{-4}

Table V. (a) $\overline{u}^2$, $\overline{w}^2$, $-\overline{uw}$ data for Case I

x = -24 in.				x = -12 in.				x = -6 in.				x = -4 in.				x = -2 in.			
z	$\overline{u}^2$	$\overline{w}^2$	$-\overline{uw}$	z	$\overline{u}^2$	$\overline{w}^2$	$-\overline{uw}$	z	$\overline{u}^2$	$\overline{w}^2$	$-\overline{uw}$	z	$\overline{u}^2$	$\overline{w}^2$	$-\overline{uw}$	z	$\overline{u}^2$	$\overline{w}^2$	$-\overline{uw}$
(in.)	$(fps)^2$	$(fps)^2$	$(fps)^2$	(in.)	$(fps)^2$	$(fps)^2$	$(fps)^2$	(in.)	$(fps)^2$	$(fps)^2$	$(fps)^2$	(in.)	$(fps)^2$	$(fps)^2$	$(fps)^2$	(in.)	$(fps)^2$	$(fps)^2$	$(fps)^2$
0.094	12.75	0.85	0.41	0.063	17.00	0.85	0.48	0.188	6.27	0.81	0.72	0.188	6.27	1.07	0.82	0.188	6.36	1.00	0.71
0.156	7.40	0.83	0.67	0.125	10.10	0.80	0.67	0.250	5.76	0.88	0.69	0.250	6.10	1.03	0.71	0.250	5.84	0.95	0.66
0.250	5.90	0.82	0.68	0.250	6.96	0.87	0.64	0.375	4.67	0.79	0.70	0.375	5.50	0.97	0.67	0.313	5.44	0.91	0.56
0.375	4.93	0.80	0.60	0.375	5.60	0.84	0.70	0.500	4.44	0.72	0.62	0.500	4.76	0.80	0.62	0.375	5.15	0.85	0.60
0.500	4.25	0.73	0.57	0.438	5.15	0.76	0.62	0.625	3.92	0.70	0.51	0.625	4.22	0.72	0.53	0.500	4.63	0.82	0.60
0.625	3.65	0.71	0.52	0.625	4.50	0.58	0.42	0.875	3.02	0.58	0.45	0.875	4.21	0.55	0.47	0.625	4.17	0.74	0.53
0.875	2.71	0.52	0.31	0.875	3.64	0.47	0.31	1.125	2.27	0.32	0.30	1.125	3.30	0.39	0.31	0.875	3.39	0.56	0.47
1.125	1.94	0.34	0.25	1.187	2.60	0.24	0.24	1.500	1.59	0.15	0.23	1.500	2.95	0.22	0.22	1.125	2.57	0.36	0.37
1.750	0.98	0.08	0.10	1.875	0.76	0.10	0.10	2.000	0.80	0.02	0.09	2.000	1.85	0.04	0.05	1.500	2.07	0.22	0.25
2.250	0.25	0.00	0.04	2.875	0.38	0.00	0.01	2.469	0.41	0.01	0.03	2.469	0.41	0.00	0.02	2.000	1.08	0.08	0.13
																2.469	0.48	0.01	0.04

x = 0 in.				x = 2 in.				x = 4 in.				x = 6 in.				x = 12 in.				x = 24 in.			
z	$\overline{u}^2$	$\overline{w}^2$	$-\overline{uw}$	z	$\overline{u}^2$	$\overline{w}^2$	$-\overline{uw}$	z	$\overline{u}^2$	$\overline{w}^2$	$-\overline{uw}$	z	$\overline{u}^2$	$\overline{w}^2$	$-\overline{uw}$	z	$\overline{u}^2$	$\overline{w}^2$	$-\overline{uw}$	z	$\overline{u}^2$	$\overline{w}^2$	$-\overline{uw}$
(in.)	$(fps)^2$	$(fps)^2$	fps	(in.)	$(fps)^2$	$(fps)^2$	$(fps)^2$	(in.)	$(fps)^2$	$(fps)^2$	$(fps)^2$	(in.)	$(fps)^2$	$(fps)^2$	$(fps)^2$	(in.)	$(fps)^2$	$(fps)^2$	$(fps)^2$	(in.)	$(fps)^2$	$(fps)^2$	$(fps)^2$
0.125	7.39	1.26	1.19	0.125	11.22	2.06	1.64	0.125	10.20	1.42	1.06	0.125	7.45	1.27	1.16	0.125	8.88	1.48	1.07	0.125	11.00	1.05	1.51
0.188	6.38	1.09	1.12	0.188	9.82	1.76	1.18	0.188	8.09	1.38	0.81	0.188	8.65	1.40	1.30	0.188	9.43	1.68	1.17	0.188	12.40	2.09	1.67
0.250	5.84	1.00	1.11	0.250	6.70	1.11	0.70	0.250	7.35	1.26	0.70	0.250	9.06	1.47	1.56	0.250	9.89	2.02	1.29	0.250	13.10	2.25	1.72
0.375	5.50	0.97	0.67	0.313	5.51	0.93	0.65	0.313	6.62	1.17	0.69	0.313	8.93	1.74	1.39	0.313	9.90	2.69	1.25	0.313	12.35	1.88	1.74
0.500	7.76	0.80	0.62	0.438	4.56	0.81	0.65	0.438	5.39	0.93	0.65	0.438	7.90	1.46	1.07	0.438	8.86	1.79	1.14	0.438	11.84	2.17	1.69
0.625	4.22	0.72	0.53	0.562	4.23	0.74	0.56	0.562	3.85	0.68	0.62	0.625	5.42	1.10	0.84	0.625	7.32	1.56	1.08	0.625	10.30	2.41	1.70
0.875	4.21	0.55	0.47	0.750	3.61	0.64	0.52	0.750	3.48	0.67	0.58	0.875	4.33	0.79	0.63	0.875	5.05	0.99	0.86	0.875	8.61	1.89	1.41
1.125	3.30	0.39	0.31	1.000	3.06	0.52	0.41	1.000	3.10	0.53	0.51	1.375	2.82	0.40	0.41	1.375	2.65	0.44	0.43	1.375	4.73	1.02	0.83
1.500	2.95	0.22	0.22	1.250	2.59	0.42	0.31	1.250	2.54	0.36	0.45	1.875	1.20	0.16	0.24	1.875	1.56	0.19	0.22	1.875	2.23	0.32	0.32
2.000	1.85	0.04	0.05	1.750	1.28	0.19	0.20	1.750	1.46	0.17	0.17	2.625	0.44	0.02	0.06	2.625	0.50	0.05	0.09	2.625	0.62	0.04	0.09
				2.500	0.50	0.01	0.06	2.500	0.43	0.03	0.10												

Table V. (b) $\overline{v^2}$ data for Case I

x = -24 in.		x = -4 in.		x = -2 in.		x = 2 in.		x = 4 in.		x = 6 in.		x = 24 in.	
z	$\overline{v^2}$	z	$\overline{v^2}$	z	$\overline{v^2}$	z	$\overline{v^2}$	z	$\overline{v^2}$	z	$\overline{v^2}$	z	$\overline{v^2}$
(in.)	$(fps)^2$	(in.)	$(fps)^2$	(in.)	$(fps)^2$	(in.)	$(fps)^2$	(in.)	$(fps)^2$	(in.)	$(fps)^2$	(in.)	$(fps)^2$
0.063	2.00	0.175	2.10	0.175	1.95	0.100	3.50	0.100	3.00	0.100	2.70	0.250	3.00
0.125	1.75	0.300	1.75	0.300	1.75	0.225	2.50	0.625	1.60	0.175	3.40	0.425	3.30
0.260	1.70	0.500	1.65	0.500	1.60	0.425	1.85	0.750	1.50	0.225	3.20	0.600	3.10
0.500	1.15	0.675	1.45	0.675	1.55	0.625	1.65	1.000	1.25	0.425	2.10	0.750	2.55
0.675	0.95	0.870	1.10	0.870	1.35	0.750	1.55	1.500	0.55	0.625	1.30	1.000	1.90
0.925	0.70	1.000	1.10	1.000	1.15	1.000	1.15	2.000	0.20	0.750	1.00	1.500	0.95
1.250	0.45	1.250	0.80	1.250	0.85	1.500	0.80			1.000	0.60	2.250	0.30
		2.000	0.20	2.000	0.20	2.000	0.25			1.350	0.40		
										1.500	0.35		
										2.000	0.20		

Table V. (c) $-\overline{uw}$ data for Case II

x = 6 in.		x = -4 in.		x = -2 in.		x = 0 in		x = 1 in.		x = 2 in.		x = 3 in.		x = 4 in.		x = 6 in.		x = 8 in.		x = 10 in.		x = 12 in.		x = 15 in.		x = 24 in.	
z	$-\overline{uw}$	z	$-\overline{uw}$	z	$-\overline{uw}$	z	$-\overline{uw}$	z	$-\overline{uw}$	z	$-\overline{uw}$	z	$-\overline{uw}$	z	$-\overline{uw}$	z	$-\overline{uw}$	z	$-\overline{uw}$	z	$-\overline{uw}$	z	$-\overline{uw}$	z	$-\overline{uw}$	z	$-\overline{uw}$
(in.)	$(fps)^2$	(in.)	$(fps)^2$	(in.)	$(fps)^2$	(in.)	$(fps)^2$	(in.)	$(fps)^2$	(in.)	$(fps)^2$	(in.)	$(fps)^2$	(in.)	$(fps)^2$	(in.)	$(fps)^2$	(in.)	$(fps)^2$	(in.)	$(fps)^2$	(in.)	$(fps)^2$	(in.)	$(fps)^2$	(in.)	$(fps)^2$
0.063	0.62	0.063	0.82	0.063	0.77	0.145	0.56	0.106	1.07	0.111	1.64	0.132	1.30	0.156	1.96	0.110	1.45	0.129	0.38	0.175	0.80	0.175	1.08	0.103	0.66	0.110	0.55
0.172	0.57	0.137	0.64	0.135	0.64	0.226	0.57	0.134	0.78	0.196	1.32	0.186	1.05	0.244	1.81	0.153	1.59	0.162	0.64	0.227	0.81	0.200	1.14	0.177	0.95	0.159	0.74
0.256	0.57	0.194	0.61	0.197	0.66	0.344	0.61	0.176	0.70	0.245	1.37	0.247	1.12	0.326	1.51	0.211	1.78	0.247	0.84	0.329	0.92	0.290	1.20	0.298	1.05	0.258	1.08
0.338	0.62	0.264	0.61	0.255	0.65	0.487	0.63	0.320	0.59	0.373	0.80	0.356	1.08	0.431	1.10	0.374	1.37	0.349	0.95	0.480	0.99	0.412	1.10	0.407	1.04	0.370	1.32
0.471	0.62	0.355	0.61	0.358	0.62	0.775	0.62	0.475	0.65	0.491	0.68	0.418	0.96	0.522	0.81	0.595	0.87	0.600	0.81	0.650	0.89	0.502	1.11	0.640	0.80	0.620	1.11
0.635	0.59	0.537	0.54	0.534	0.57	1.215	0.58	0.603	0.63	0.775	0.52	0.546	0.61	0.648	0.68	0.868	0.46	0.914	0.34	0.934	0.51	0.806	0.76	1.022	0.37	0.920	1.07
0.897	0.58	0.835	0.47	0.794	0.49	1.667	0.36	0.705	0.66	1.015	0.52	0.837	0.43	0.758	0.60	1.171	0.42	1.257	0.27	1.340	0.34	1.295	0.42	1.508	0.21	1.402	0.52
1.345	0.41	1.172	0.30	1.090	0.49	2.250	0.13	0.907	0.58	1.252	0.46	1.153	0.42	1.156	0.60	1.675	0.34	1.660	0.24	1.786	0.26	1.605	0.31	2.017	0.20	2.095	0.28
1.998	0.18	2.110	0.13	1.464	0.32			1.092	0.50	1.656	0.30	1.498	0.38	1.597	0.41	2.340	0.22	2.175	0.11	2.655	0.04	2.159	0.18	3.038	0.04	3.085	0.06
				2.805	0.03			1.472	0.46	2.152	0.15	2.611	0.02	2.080	0.25	2.778	0.11	2.719	0.03			2.733	0.04				
								1.989	0.31																		
								2.515	0.10																		

Table VI. Data On One-Dimensional Spectra

x = -12 in. U_∞ = 20 fps.

z = 0.065 in.		z = 0.094 in.		z = 0.499 in.		z = 0.750 in.		z = 1.622 in.		z = 2.250 in.	
k_1	$F(k_1)/\overline{u}^2$	k_1	$F(k_1)/\overline{u}^2$	k_1	$F(k_1)/\overline{u}^2$	k_1	$F(k_1)/\overline{u}^2$	k_1	$F(k_1)/\overline{u}^2$	k_1	$F(k_1)/\overline{u}^2$
ft^{-1}	ft	ft^{-1}	ft	ft^{-1}	ft	ft^{-1}	ft	ft^{-1}	ft	ft^{-1}	ft
1.02×10^{1}	7.82×10^{-3}	8.88×10^{0}	7.58×10^{-3}	6.60×10^{0}	1.57×10^{-2}	6.13×10^{0}	1.89×10^{-2}	5.35×10^{0}	2.90×10^{-2}	5.17×10^{0}	2.90×10^{-2}
1.28	1.00×10^{-2}	1.11×10^{1}	1.32×10^{-2}	8.26	1.86	7.66	2.56	6.68	4.28	6.47	2.16
1.60	1.52	1.39	1.62	1.03×10^{1}	2.42	9.57	2.92	8.35	3.80	8.08	1.93
2.04	1.60	1.78	1.78	1.32	2.49	1.23×10^{1}	2.61	1.07×10^{1}	3.54	1.04×10^{1}	3.14
2.56	1.60	2.22	1.78	1.65	1.86	1.53	2.38	1.34	2.52	1.29	2.29
3.20	9.08×10^{-3}	2.77	1.42	2.07	1.79	1.92	1.93	1.67	1.90	1.62	2.05
4.09	9.08	3.55	1.00	2.64	1.30	2.45	1.33	2.14	1.39	2.07	1.57
5.11	7.43	4.44	8.08×10^{-3}	3.30	1.02	3.06	9.40×10^{-3}	2.67	1.21	2.59	1.16
6.39	5.10	5.55	5.18	4.13	7.15×10^{-3}	3.83	7.00	3.34	7.80×10^{-3}	3.23	5.82×10^{-3}
7.99	3.41	6.94	3.39	5.16	4.85	4.79	4.91	4.18	5.06	4.04	5.45
1.02×10^{2}	2.04	8.88	2.58	6.61	3.58	6.13	3.40	5.35	3.42	5.17	3.50
1.28	1.06	1.11×10^{2}	1.62	8.26	1.94	7.66	2.10	6.68	2.65	6.47	2.66
1.60	4.95×10^{-4}	1.39	8.40×10^{-4}	1.03×10^{2}	1.04	9.57	1.12	8.35	1.06	8.08	1.18
2.04	2.94	1.78	5.82	1.32	8.16×10^{-4}	1.23×10^{2}	7.30×10^{-4}	1.07	8.20×10^{-4}	1.04	8.35×10^{-4}
2.56	1.14	2.22	2.58	1.65	4.10	1.53	3.87	1.34	3.65	1.29	3.00
3.20	4.85×10^{-5}	2.77	1.55	2.07	2.54	1.92	2.46	1.67	2.27	1.62	1.45
4.09	1.86	3.55	7.10×10^{-5}	2.64	1.35	2.45	1.23	2.14	1.02	2.07	1.21
5.11	7.12×10^{-6}	4.44	3.07	3.30	6.64×10^{-5}	3.06	6.66×10^{-5}	2.67	6.45×10^{-5}	2.59	6.78×10^{-5}
6.39	1.88	5.55	1.21	4.13	2.81	3.83	2.42	3.34	2.15	3.23	3.50
7.99	8.13×10^{-7}	6.94	5.23×10^{-6}	5.16	1.27	4.79	1.12	4.18	1.06	4.04	1.45
1.02×10^{3}	2.50	8.88	1.37	6.61	3.82×10^{-6}	6.13	2.98×10^{-6}	5.35	3.65×10^{-6}	5.17	6.87×10^{-6}
1.28	1.10	1.11×10^{3}	4.87×10^{-7}	8.26	1.25	7.66	1.12			6.47	6.40
1.60	6.28×10^{-8}	1.39	1.95	1.03×10^{3}	4.33×10^{-7}	9.57	5.22×10^{-7}				

Table VI. Data on One-Dimensional Spectra - Continued

x = +4 in. U_∞ = 20 fps

z = 0.125 in.		z = 0.238 in.		z = 0.437 in.		z = 0.562 in.		z = 0.750 in.		z = 1.250 in.		z = 1.750 in.	
k_1 ft^{-1}	$F(k_1)/\overline{u}^2$ ft	k_1 ft^{-1}	$F(k_1)/\overline{u}^2$ ft	k_1 ft^{-1}	$F(k_1)/\overline{u}^2$ ft	k_1 ft^{-1}	$F(k_1)/\overline{u}^2$ ft	k_1 ft^{-1}	$F(k_1)/\overline{u}^2$ ft	k_1 ft^{-1}	$F(k_1)/\overline{u}^2$ ft	k_1 ft^{-1}	$F(k_1)/\overline{u}^2$ ft
1.25×10^1	2.94×10^{-3}	1.09×10^1	4.66×10^{-3}	7.42×10^0	8.42×10^{-3}	6.65×10^0	1.71×10^{-2}	6.28×10^0	2.68×10^{-2}	5.65×10^0	2.76×10^{-2}	5.29×10^0	3.78×10^{-2}
1.56	4.04	1.37	6.82	9.27	1.27×10^{-2}	8.32	1.97	7.85	2.92	7.06	2.96	6.61	4.10
1.96	6.14	1.71	9.35	1.16×10^1	1.50	1.04×10^1	2.46	9.80	3.31	8.82	3.27	8.26	4.58
2.50	8.00	2.18	1.01×10^{-2}	1.48	1.64	1.33	2.44	1.26×10^1	2.88	1.13×10^1	3.03	1.06×10^1	3.30
3.13	9.21	2.73	1.32	1.85	1.87	1.66	2.35	1.57	2.34	1.41	2.84	1.32	2.87
3.91	9.68	3.41	1.24	2.32	1.72	2.08	1.77	1.96	1.76	1.76	2.10	1.65	2.18
5.01	6.56	4.37	8.02×10^{-3}	2.97	1.21	2.66	1.33	2.51	1.38	2.26	1.56	2.12	1.77
6.26	5.98	5.46	6.45	3.71	8.96×10^{-3}	3.33	8.71×10^{-3}	3.14	9.17×10^{-3}	2.82	1.05	2.64	1.16
7.82	4.35	6.84	4.07	4.63	6.15	4.16	6.09	3.93	6.73	3.53	7.09×10^{-3}	3.31	8.45×10^{-3}
9.78	2.94	8.53	2.99	5.79	4.19	5.20	4.64	4.91	4.59	4.41	4.80	4.13	4.90
1.25×10^2	2.19	1.09×10^2	1.96	7.42	3.31	6.65	3.20	6.28	3.01	5.65	3.46	5.29	3.69
1.56	1.34	1.37	1.32	9.27	2.14	8.32	2.06	7.85	1.97	7.06	2.12	6.61	2.25
1.96	7.45×10^{-4}	1.71	6.21×10^{-4}	1.16×10^2	1.10	1.04×10^2	1.02	9.80	9.48×10^{-4}	8.82	1.09	8.26	1.04
2.50	4.78	2.18	4.40	1.48	8.21×10^{-4}	1.33	7.82×10^{-4}	1.26×10^2	6.72	1.13×10^2	7.77×10^{-4}	1.06×10^2	8.05×10^{-4}
3.13	2.50	2.73	2.50	1.85	4.67	1.66	4.07	1.57	3.82	1.41	3.80	1.32	4.02
3.91	1.57	3.41	1.43	2.32	3.46	2.08	2.79	1.96	2.45	1.76	2.38	1.65	2.49
5.01	7.00×10^{-5}	4.37	7.18×10^{-5}	2.97	1.72	2.66	1.37	2.51	1.18	2.26	1.16	2.12	1.12
6.26	3.70	5.46	3.40	3.71	9.06×10^{-5}	3.33	6.97×10^{-5}	3.14	5.94×10^{-5}	2.82	5.64×10^{-5}	2.64	4.02×10^{-5}
7.82	1.66	6.84	1.44	4.63	3.74	4.16	2.89	3.93	2.21	3.53	2.18	3.31	1.95
9.78	1.34	8.53	6.45×10^{-6}	5.79	1.87	5.20	1.44	4.91	1.03	4.41	9.64×10^{-6}	4.13	6.27×10^{-6}
1.25×10^3	4.10×10^{-6}	1.09×10^3	2.04	7.42	5.99×10^{-6}	6.65	5.22×10^{-6}	6.28	3.11×10^{-6}	5.65	2.89	5.29	2.33
1.56	2.10	1.37	6.81×10^{-7}	9.27	2.61	8.32	1.56	7.85	1.06	7.06	9.33×10^{-7}	6.61	9.70×10^{-7}
1.96	9.25×10^{-7}	1.71	1.90	1.16×10^3	8.60×10^{-7}	1.04×10^3	5.22×10^{-7}	9.80	4.33×10^{-7}	8.82	4.68	8.26	6.05
		2.18	9.52×10^{-8}	1.48	2.98	1.33	3.20	1.26	3.31				

Table VI. Data On One-Dimensional Spectra - Continued

x = +6 in. U_∞ = 20 fps

z = 0.125 in.		z = 0.238 in.		z = 0.250 in.		z = 0.437 in.		z = 0.625 in.		z = 0.875 in.		z = 1.875 in.	
k_1 ft^{-1}	$F(k_1)/\overline{u}^2$ ft	k_1 ft^{-1}	$F(k_1)/\overline{u}^2$ ft	k_1 ft^{-1}	$F(k_1)/\overline{u}^2$ ft	k_1 ft^{-1}	$F(k_1)/\overline{u}^2$ ft	k_1 ft^{-1}	$F(k_1)/\overline{u}^2$ ft	k_1 ft^{-1}	$F(k_1)/\overline{u}^2$ ft	k_1 ft^{-1}	$F(k_1)/\overline{u}^2$ ft
1.86×10^{1}	2.62×10^{-3}	1.45×10^{1}	4.64×10^{-3}	1.08×10^{1}	7.00×10^{-3}	7.82×10^{0}	1.39×10^{-2}	6.65×10^{0}	1.54×10^{-2}	6.24×10^{0}	2.42×10^{-2}	5.30×10^{0}	2.48×10^{-2}
2.33	3.65	1.81	5.75	1.34	9.82	9.77	1.82	8.30	1.68	7.80	2.53	6.63	2.73
2.91	6.80	2.26	8.73	1.68	1.36×10^{-2}	1.22×10^{1}	2.29	1.04×10^{1}	2.48	9.75	2.88	8.29	3.07
3.72	7.49	2.90	9.06	2.15	1.25	1.56	1.77	1.33	2.35	1.25×10^{1}	2.53	1.06×10^{1}	3.07
4.65	5.95	3.62	7.96	2.69	1.33	1.96	1.62	1.66	2.08	1.56	2.15	1.33	2.60
5.82	4.65	4.52	5.46	3.36	1.28	2.44	1.16	2.08	1.51	1.95	1.46	1.66	2.05
7.44	4.56	5.79	4.37	4.30	9.64×10^{-3}	3.13	1.03	2.66	1.22	2.50	1.28	2.12	1.51
9.30	3.18	7.24	5.28	5.37	6.60	3.91	7.16×10^{-3}	3.33	9.26×10^{-3}	3.12	8.30×10^{-3}	2.65	1.27
1.16×10^{2}	1.89	9.05	3.46	6.72	4.81	4.89	4.92	4.16	6.43	3.90	6.05	3.31	7.16×10^{-3}
1.45	9.90×10^{-6}	1.13×10^{2}	2.37	8.40	3.02	6.11	3.48	5.20	4.69	4.88	4.51	4.14	5.43
1.86	1.19×10^{-3}	1.45	1.55	1.08×10^{2}	2.06	7.82	2.46	6.65	3.21	6.24	2.95	5.30	3.71
2.33	7.40×10^{-4}	1.81	1.01	1.34	1.27	9.77	1.66	9.32	2.14	7.80	2.08	6.63	2.69
2.91	3.65	2.26	4.91×10^{-6}	1.68	6.19×10^{-6}	1.22×10^{2}	7.98×10^{-4}	1.04×10^{2}	1.08	9.75	1.00	8.29	1.25
3.72	2.44	2.90	3.46	2.15	4.54	1.56	5.94	1.33	7.70×10^{-4}	1.25×10^{2}	6.92×10^{-4}	1.06×10^{2}	8.81×10^{-4}
4.65	1.29	3.62	1.87	2.69	2.62	1.96	3.36	1.66	4.21	1.56	3.95	1.33	4.20
5.82	7.65×10^{-5}	4.52	1.05	3.36	1.52	2.44	2.05	2.08	2.72	1.95	2.28	1.66	2.77
7.44	3.53	5.79	5.38×10^{-5}	4.30	7.89×10^{-5}	3.13	1.00	2.66	1.31	2.50	1.15	2.12	1.18
9.30	1.55	7.24	2.37	5.37	3.87	3.91	5.41×10^{-5}	3.33	7.17×10^{-5}	3.12	5.54×10^{-5}	2.65	6.34×10^{-5}
1.16×10^{3}	6.15×10^{-6}	9.05	1.00	6.72	1.64	4.89	2.05	4.16	2.89	3.90	2.04	3.31	2.31
1.45	2.31	1.13×10^{3}	4.53×10^{-6}	8.40	6.70×10^{-6}	6.11	9.52×10^{-6}	5.20	1.59	4.88	9.68×10^{-6}	4.14	1.13
1.86	7.65×10^{-7}	1.45	1.27	1.08×10^{3}	1.94	7.82	2.83	6.65	4.45×10^{-6}	6.24	2.82	5.30	4.62×10^{-6}
2.33	2.56	1.81	3.46×10^{-7}	1.34	6.40×10^{-7}	9.77	9.27×10^{-7}	8.32	1.68	7.80	1.15	6.63	2.14
2.91	7.05×10^{-8}	2.26	1.46	1.68	2.08	1.22×10^{3}	2.83	1.04×10^{3}	6.01×10^{-7}	9.75	5.20×10^{-7}	8.29	1.30
		2.90	2.30×10^{-8}	2.15	8.48×10^{-8}	1.56	1.47	1.33	3.61	1.25×10^{3}	2.97		

Table VI. Data On One-Dimensional Spectra - Continued

x = +12 in. U_∞ = 20 fps

z = 0.125 in.		z = 0.238 in.		z = 0.250 in.		z = 0.437 in.		z = 0.625 in.		z = 1.875 in.		z = 1.875 in.	
k_1 ft^{-1}	$F(k_1)/\overline{u}^2$ ft	k_1 ft^{-1}	$F(k_1)/\overline{u}^2$ ft	k_1 ft^{-1}	$F(k_1)/\overline{u}^2$ ft	k_1 ft^{-1}	$F(k_1)/\overline{u}^2$ ft	k_1 ft^{-1}	$F(k_1)/\overline{u}^2$ ft	k_1 ft^{-1}	$F(k_1)/\overline{u}^2$ ft	k_1 ft^{-1}	$F(k_1)/\overline{u}^2$ ft
1.86×10^{1}	5.17×10^{-3}	1.26×10^{1}	4.72×10^{-3}	1.08×10^{1}	6.11×10^{-3}	8.78×10^{0}	1.29×10^{-2}	7.42×10^{0}	2.48×10^{-2}	6.57×10^{0}	1.70×10^{-2}	5.37×10^{0}	1.69×10^{-2}
2.33	5.27	1.57	5.97	1.35	7.88	1.10×10^{1}	1.20	9.27	2.21	8.21	1.73	6.70	1.89
2.91	8.44	1.96	9.74	1.68	1.24×10^{-2}	1.37	1.69	1.16×10^{1}	2.42	1.03×10^{1}	2.11	8.40	2.30
3.72	1.05×10^{-2}	2.51	1.15×10^{-2}	2.15	1.43	1.76	1.71	1.48	2.07	1.31	1.95	1.08×10^{1}	2.75
4.65	1.25	3.14	1.25	2.69	1.26	2.19	1.75	1.85	1.80	1.64	1.97	1.34	2.10
5.82	8.44×10^{-3}	3.93	9.62×10^{-3}	3.36	1.01	2.74	1.21	2.32	1.26	2.05	1.52	1.68	1.60
7.44	7.10	5.02	7.22	4.30	7.84×10^{-3}	3.51	8.68×10^{-3}	2.97	1.15	2.63	1.29	2.15	1.39
9.30	5.27	6.28	5.23	5.38	5.85	4.39	6.37	3.71	7.85×10^{-3}	3.28	8.87×10^{-3}	2.69	1.04
1.16×10^{2}	3.55	7.85	3.66	6.72	3.91	5.49	4.56	4.64	5.27	4.10	6.83	3.36	6.76×10^{-3}
1.45	2.40	9.81	2.62	8.40	2.60	6.86	3.18	5.79	3.73	5.13	4.32	4.20	4.95
1.86	1.53	1.26×10^{2}	1.66	1.08×10^{2}	1.83	8.78	2.07	7.42	2.72	6.57	3.05	5.37	3.38
2.33	9.56×10^{-4}	1.57	9.93×10^{-4}	1.35	1.16	1.10×10^{2}	1.47	9.27	1.60	8.21	2.00	6.70	2.27
2.91	4.31	1.96	4.59	1.68	5.86×10^{-6}	1.37	7.37×10^{-4}	1.16×10^{2}	8.50×10^{-4}	1.03×10^{2}	1.04	8.40	1.08
3.72	3.36	2.51	3.44	2.15	4.01	1.76	4.96	1.48	6.11	1.31	7.50×10^{-4}	1.08×10^{2}	8.16×10^{-4}
4.65	1.73	3.14	1.78	2.69	2.23	2.19	2.79	1.85	3.39	1.64	4.04	1.34	4.37
5.82	1.05	3.93	1.15	3.36	1.43	2.74	1.79	2.32	2.07	2.05	2.79	1.68	2.50
7.44	5.08×10^{-5}	5.02	5.54×10^{-5}	4.30	6.51×10^{-5}	3.51	8.15×10^{-5}	2.97	1.02	2.63	1.34	2.15	1.18
9.30	2.12	6.28	2.41	5.38	3.12	4.39	4.38	3.71	5.40×10^{-5}	3.28	6.70×10^{-5}	2.69	6.42×10^{-5}
1.16×10^{3}	9.58×10^{-6}	7.85	1.02	6.72	1.30	5.49	1.79	4.64	2.20	4.10	2.90	3.36	2.83
1.45	3.74	9.81	4.08×10^{-6}	8.40	6.54×10^{-6}	6.86	7.56×10^{-6}	5.79	9.87×10^{-6}	5.13	1.48	4.20	1.53
1.86	1.21	1.26×10^{3}	1.27	1.08×10^{3}	1.82	8.78	2.46	7.42	2.98	6.57	4.56×10^{-6}	5.37	5.34×10^{-6}
2.33	5.28×10^{-7}	1.57	4.18×10^{-7}	1.35	5.86×10^{-7}	1.10×10^{3}	7.11×10^{-7}	9.27	9.17×10^{-7}	8.21	1.50	6.70	2.42
2.91	1.43	1.96	1.89	1.68	1.83	1.37	2.56	1.16×10^{3}	2.94	1.03×10^{3}	6.82×10^{-7}	8.40	1.36
		2.51	8.50×10^{-8}	2.15	7.42×10^{-8}	1.76	1.24	1.48	1.94	1.31	3.29		

Table VII. Parameters Used in Spectral Calculations for Case I

U_∞ = 20 fps

x (in.)	z (in.)	U (fps)	$\overline{u^2}$ (fps^2)	$-\overline{uw}$ (fps^2)	ν (ft^2/sec)	λ_g (ft)	ξ (ft^2/sec^3)	k_s (ft^{-1})	z/δ	$D = \frac{\xi}{\overline{uw}\frac{\partial U}{\partial z}}$
-12	0.065	9.83	16.50	0.48	2.00×10^{-4}	1.34×10^{-2}	277.00	2.43×10^{3}	0.026	1.39
	0.094	11.32	15.50	0.55	2.00×10^{-4}	1.15×10^{-2}	285.20	2.44×10^{3}	0.039	1.86
	0.499	15.20	4.80	0.60	2.00×10^{-4}	1.34×10^{-2}	97.40	1.87×10^{3}	0.208	2.20
	0.750	16.40	4.10	0.39	2.00×10^{-4}	1.61×10^{-2}	47.70	1.56×10^{3}	0.313	2.48
	1.622	18.80	1.45	0.13	2.00×10^{-4}	1.95×10^{-2}	11.05	1.08×10^{3}	0.676	3.66
	2.250	19.42	0.64	0.03	2.00×10^{-4}	1.88×10^{-2}	5.42	9.07×10^{2}	0.938	10.42
+4	0.125	8.03	10.20	1.06	2.00×10^{-4}	6.50×10^{-3}	716.50	3.08×10^{3}	0.049	1.37
	0.188	9.20	8.09	0.81	2.00×10^{-4}	8.80×10^{-3}	313.40	2.50×10^{3}	0.074	1.18
	0.437	13.55	5.39	0.65	2.00×10^{-4}	1.04×10^{-2}	148.60	2.08×10^{3}	0.172	1.62
	0.562	15.10	3.85	0.62	2.00×10^{-4}	1.34×10^{-2}	64.36	1.68×10^{3}	0.221	1.07
	0.750	16.00	3.48	0.58	2.00×10^{-4}	1.58×10^{-2}	41.80	1.51×10^{3}	0.294	1.30
	1.250	17.80	2.54	0.45	2.00×10^{-4}	1.86×10^{-2}	22.00	1.29×10^{3}	0.491	1.47
	1.750	19.00	1.46	0.17	2.00×10^{-4}	2.09×10^{-2}	9.99	1.06×10^{3}	0.686	2.37
	2.500	19.75	0.43	0.10	2.00×10^{-4}	2.24×10^{-2}	2.59	7.55×10^{2}	0.979	4.50
+6	0.125	5.40	7.45	1.16	2.00×10^{-4}	5.67×10^{-3}	695.20	3.05×10^{3}	0.045	1.03
	0.188	6.94	8.65	1.30	2.00×10^{-4}	6.68×10^{-3}	581.30	2.92×10^{3}	0.068	1.15
	0.250	9.35	9.06	1.56	2.00×10^{-4}	8.69×10^{-3}	360.00	2.59×10^{3}	0.091	0.79
	0.437	12.85	7.90	1.07	2.00×10^{-4}	1.24×10^{-2}	154.50	2.10×10^{3}	0.159	0.86
	0.625	15.10	5.42	0.84	2.00×10^{-4}	1.34×10^{-2}	90.80	1.84×10^{3}	0.227	1.10
	0.875	16.10	4.33	0.63	2.00×10^{-4}	1.62×10^{-2}	49.40	1.58×10^{3}	0.518	1.60
	1.875	18.95	1.20	0.24	2.00×10^{-4}	1.89×10^{-2}	10.00	1.06×10^{3}	0.682	1.77
+12	0.125	7.63	8.88	1.07	2.00×10^{-4}	7.90×10^{-3}	427.97	2.71×10^{3}	0.044	1.01
	0.238	8.00	9.43	1.17	2.00×10^{-4}	8.20×10^{-3}	422.13	2.70×10^{3}	0.083	1.37
	0.250	9.34	9.89	1.29	2.00×10^{-4}	9.40×10^{-3}	339.20	2.55×10^{3}	0.087	1.50
	0.437	11.45	8.86	1.14	2.00×10^{-4}	1.14×10^{-3}	204.50	2.45×10^{3}	0.152	1.37
	0.625	13.55	7.32	1.08	2.00×10^{-4}	1.30×10^{-3}	128.70	2.00×10^{3}	0.218	1.19
	0.875	15.30	5.05	0.86	2.00×10^{-4}	1.38×10^{-3}	79.30	1.77×10^{3}	0.305	1.29
	1.875	18.70	1.56	0.22	2.00×10^{-4}	1.79×10^{-3}	14.63	1.16×10^{3}	0.654	3.40

Table VIII. Mass Concentration Data for Case I

Point ground source at x = -36 inches U_∞ = 20 fps

x (in.)	y (in.)	z (in.)	C (ppm)	x (in.)	y (in.)	z (in.)	C (ppm)	x (in.)	y (in.)	z (in.)	C (ppm)	x (in.)	y (in.)	z (in.)	C (ppm)	x (in.)	y (in.)	z (in.)	C (ppm)
-24	℄	0.031	24000	-24	0.375E	0.031	15500	-24	0.938E	0.031	6000	-12	℄	0.031	6900	-12	0.500E	0.031	7400
		0.234	18000			0.218	12500			0.359	4700				6300			0.125	7000
		0.531	6000			0.500	7800			0.640	2800				5100			0.531	5200
		0.906	1700			0.750	5300			1.062	490				2950			0.875	3100
		1.218	340			1.140	780			1.500	10				2250			1.438	800
		1.375	155			1.547	340								185			1.750	265
		1.812	78												115			2.281	39
-24	1.312E	0.031	1625	-24	1.750E	0.031	115	-24	0.875W	0.031	1820	-12	2.000E	0.031	1000	-12	1.000W	0.031	1850
		0.156	1625			0.156	122			0.218	1800			0.469	720			0.688	1400
		0.312	1550			0.422	160			0.500	1220			1.078	420			1.375	265
		0.625	1000			0.781	100			0.734	475			1.594	90			2.000	48
		1.094	380			1.000	71			1.265	58								
		1.359	330			1.422	10												

Table VIII. Continued

x (in.)	y (in.)	z (in.)	C (ppm)	x (in.)	y (in.)	z (in.)	C (ppm)	x (in.)	y (in.)	z (in.)	C (ppm)	x (in.)	y (in.)	z (in.)	C (ppm)	x (in.)	y (in.)	z (in.)	C (ppm)
-12	1.000E	0.031	5300	-4	℄	0.031	4300	-4	0.406E	0.031	4400	-4	0.875E	0.031	4400	0	℄	0.172	3700
		0.188	5300			0.156	4450			0.125	4100			0.156	4300			0.297	3700
		0.500	4300			0.343	4100			0.406	3800			0.344	3900			0.469	3150
		0.781	3100			0.687	3200			0.781	2650			0.641	2900			0.875	2400
		0.948	2300			1.015	2400			1.062	2100			1.015	2050			1.375	1250
		1.438	530			1.625	960			1.469	990			1.547	800			1.938	425
		2.000	96			2.344	385			2.093	220			2.156	46			2.563	92
										2.375	100			2.484	5				
				-4	1.937E	1.813	195	-4	2.469E	0.031	660	-4	1.000W	0.031	1850	0	2.500E	0.188	1000
						2.406	35			0.172	620			0.172	1650			0.406	960
										0.422	620			0.328	1550			0.781	520
										0.781	525			0.828	1080			1.313	350
														1.093	800			1.859	110
				-4	1.703W	0.031	570							1.531	340			2.188	62
						0.281	540							2.046	90				
						0.625	380												
						1.156	250												
						1.687	80												

Table VIII. Continued

x (in.)	y (in.)	z (in.)	C (ppm)	x (in.)	y (in.)	z (in.)	C (ppm)	x (in.)	y (in.)	z (in.)	C (ppm)	x (in.)	y (in.)	z (in.)	C (ppm)	x (in.)	y (in.)	z (in.)	C (ppm)
0	0.375E	0.125	4000	0	1.000E	0.188	3350	+4	℄	0.188	3200	+4	0.469E	0.094	3300	+4	1.025E	0.141	3300
		0.266	3800			0.438	3250			0.344	3000			0.172	3150			0.344	3100
		0.688	3000			0.750	2800			0.594	2700			0.500	3050			0.625	2700
		1.063	2300			1.141	1850			1.093	2250			0.781	2500			1.063	1850
		1.469	1100			1.609	820			1.562	1340			1.313	1600			1.656	900
		2.031	275			2.313	59			2.172	410			1.813	600			2.266	265
		2.406	140							2.594	185			2.375	175			2.328	96
														2.813	68				
0	1.750W	0.188	840					+4	2.750E	0.188	630	+4	2.063W	0.188	320				
		0.344	520							0.875	620			0.297	290				
		0.656	405							0.688	580			0.641	200				
		1.000	360							1.219	480			1.219	105				
		1.563	130							2.000	94			1.718	85				
		2.375	32							2.594	47			2.562	41				

Table VIII. Continued

x (in.)	y (in.)	z (in.)	C (ppm)	x (in.)	y (in.)	z (in.)	C (ppm)	x (in.)	y (in.)	z (in.)	C (ppm)	x (in.)	y (in.)	z (in.)	C (ppm)	x (in.)	y (in.)	z (in.)	C (ppm)
+12	℄	0.109	2600	+12	0.688E	0.093	2800	+12	1.500E	0.141	2050	+24	℄	0.188	1800	+24	0.750E	0.125	1980
		0.219	2500			0.281	2700			0.313	2000			0.344	1800			0.344	1920
		0.469	2480			0.703	2550			0.719	2025			0.812	1640			0.875	1800
		0.969	2000			1.281	1750			1.250	1630			1.437	1250			1.344	1650
		1.500	1225			1.906	780			2.938	615			2.156	595			2.031	860
		2.016	640			2.719	185			2.750	135			2.656	272			2.703	320
		2.656	195			3.250	80			3.188	76			3.281	90			3.375	105
		3.062	120																
+12	2.906E	0.156	730	+12	1.000W	0.125	1590	+12	2.094W	0.188	740	+24	3.375E	0.125	400	+24	1.125W	0.125	1140
		0.500	600			0.359	1070			0.500	590			0.500	375			0.469	1140
		1.250	580			1.078	1080			0.844	580			1.062	272			0.938	1010
		1.812	285			1.844	340			1.594	150			1.688	166			1.594	650
		2.781	48			2.812	82			2.625	46			2.375	86			2.437	272
														3.094	30			3.062	86

Table VIII. Continued

x (in.)	y (in.)	z (in.)	C (ppm)	x (in.)	y (in.)	z (in.)	C (ppm)	x (in.)	y (in.)	z (in.)	C (ppm)	x (in.)	y (in.)	z (in.)	C (ppm)
+24	1.750E	0.109	1370	+36	℄	0.125	1380	+36	1.000E	0.188	1500	+36	2.000E	0.156	1200
		0.344	1280			0.312	1320			0.437	1400			0.606	1200
		0.812	1260			0.750	1300			1.031	1350			0.937	1170
		1.594	775			1.328	1175			1.844	920			1.469	1000
		2.219	415			1.969	780			2.750	640			2.281	570
		3.156	93			2.938	265			3.281	350			3.281	160
						3.406	190			3.625	109				
+24	2.375W	0.188	440	+36	4.000E	0.094	450	+36	1.469W	0.141	830	+36	3.031W	0.094	325
		0.500	415			0.531	440			0.531	830			0.438	325
		1.188	315			1.281	320			1.469	650			1.344	225
		1.750	182			1.906	270			2.344	400			2.094	120
		2.313	100			2.437	180			3.375	76			2.812	79
		3.000	40			3.391	75								

APPENDIX III
FIGURES

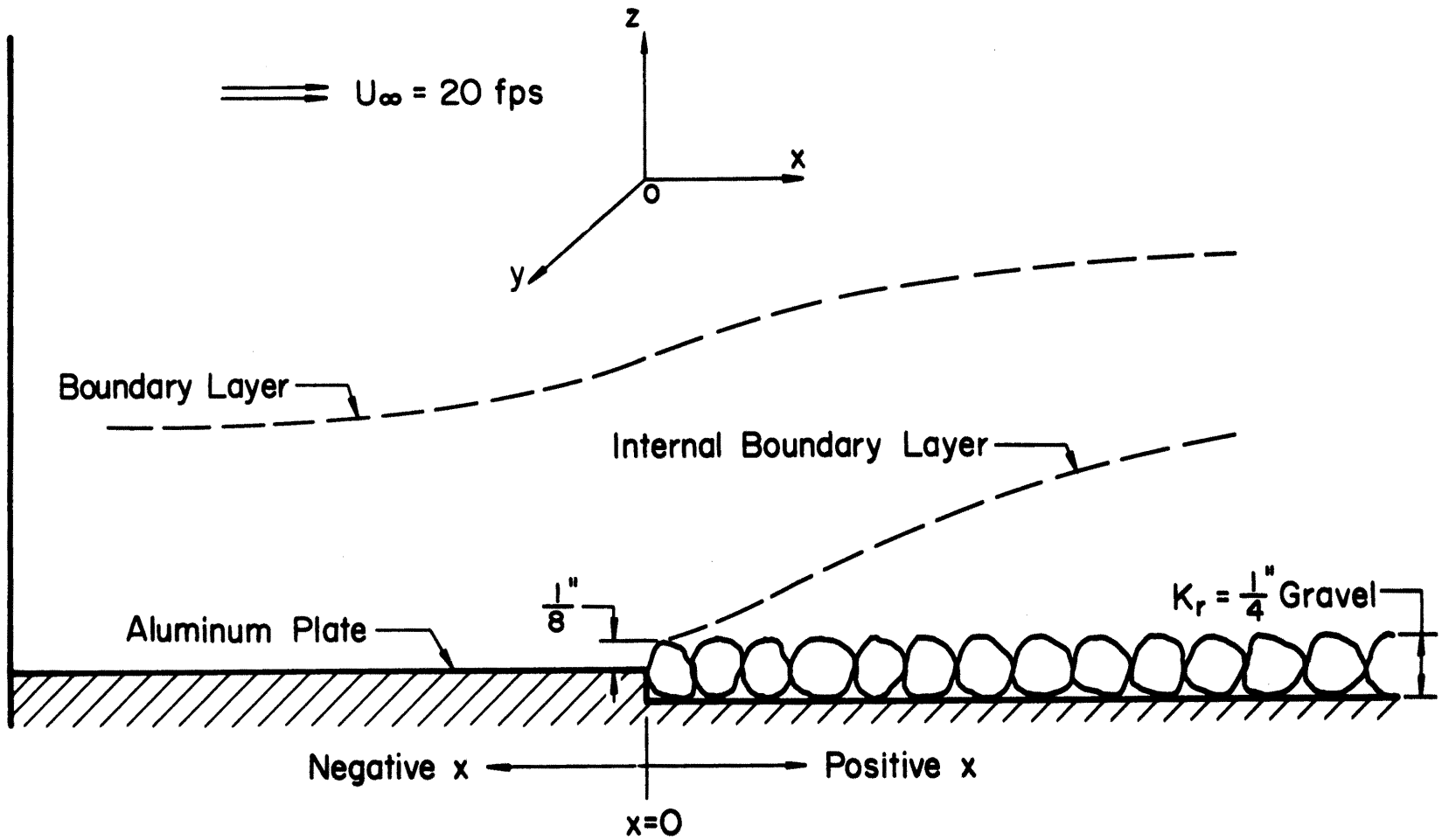

Figure 1. Coordinate system and flow features.

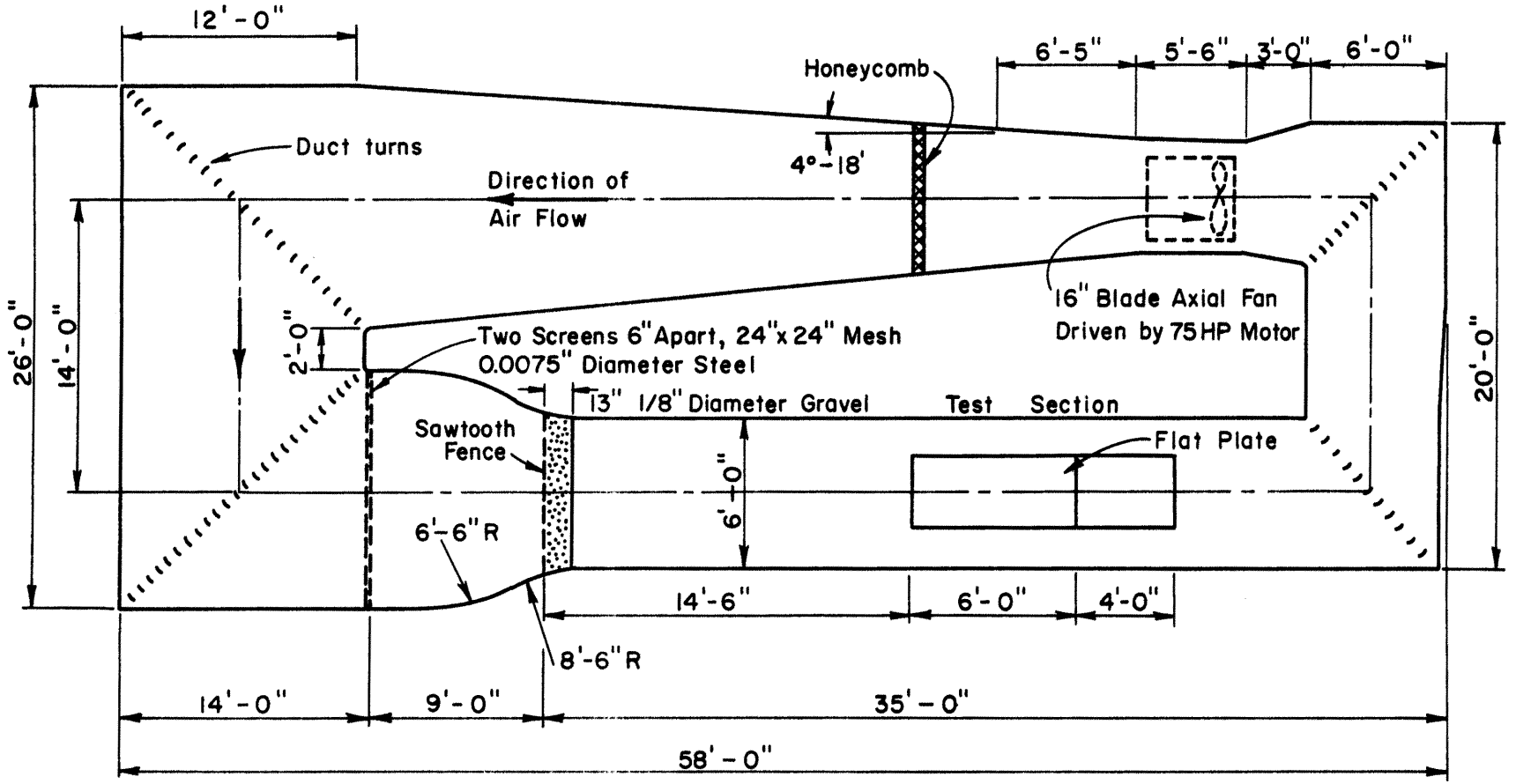

Figure 2. Plan view of wind tunnel.

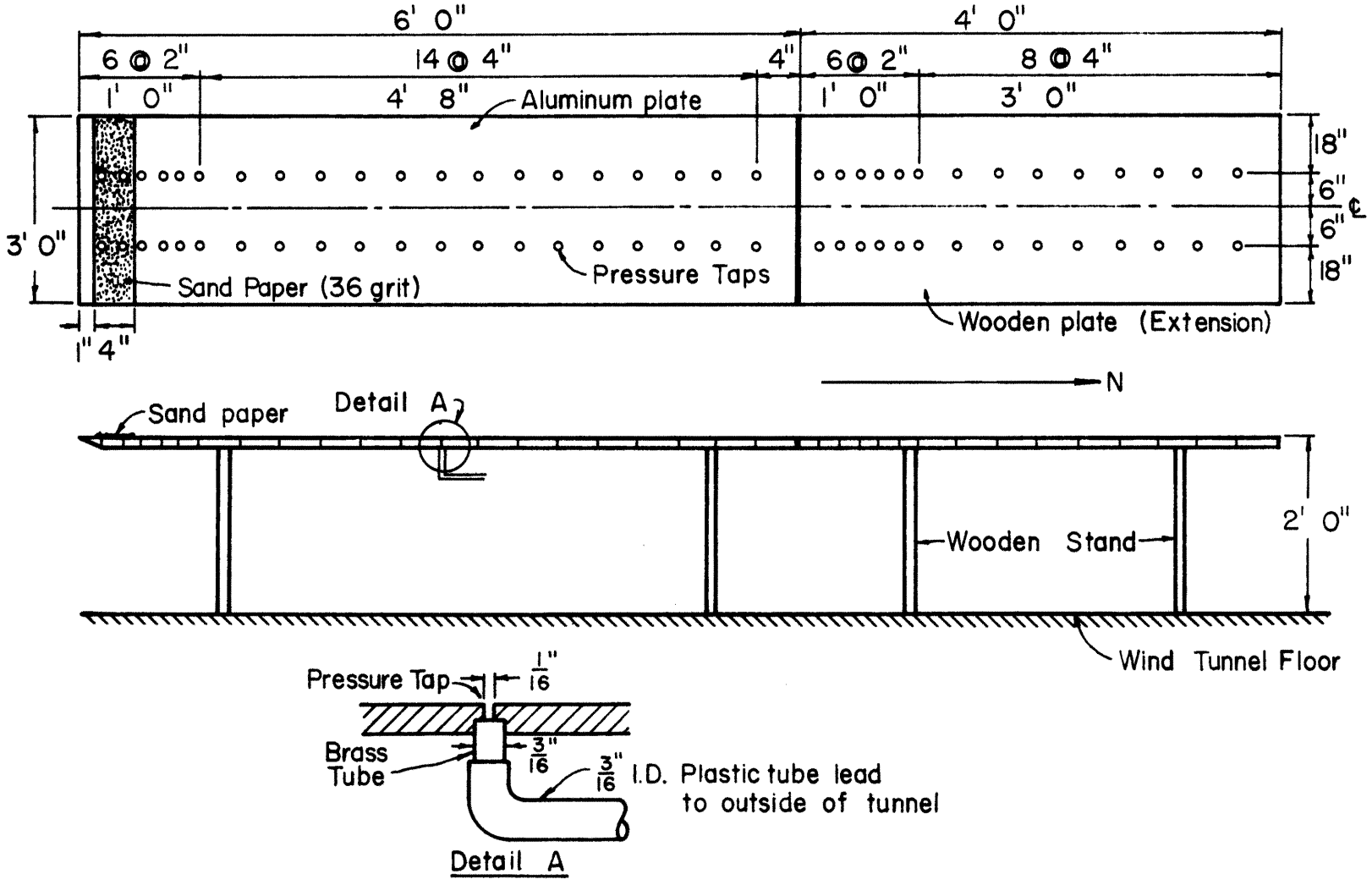

Figure 3. Flat plate and pressure tape.

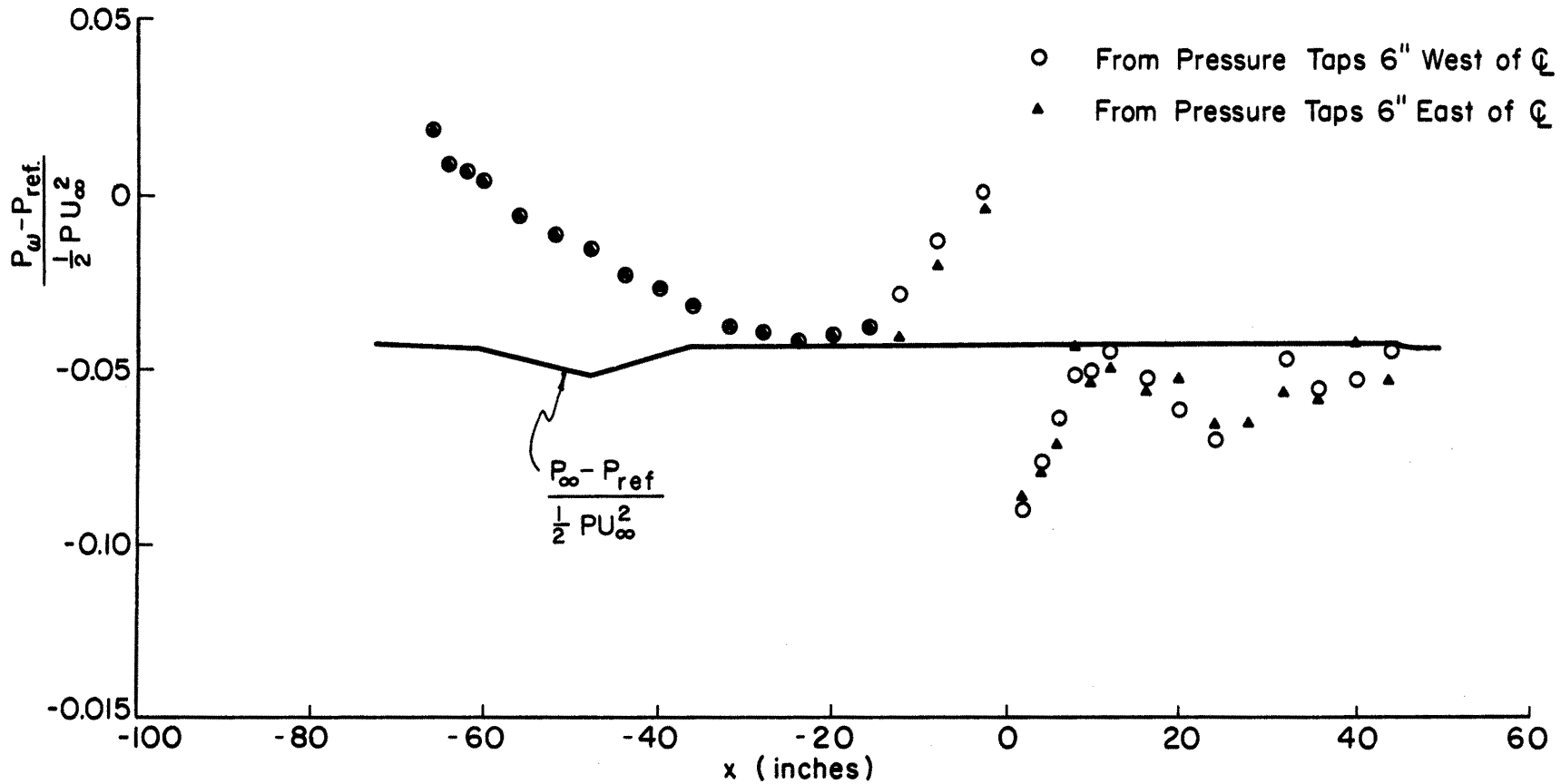

Figure 4. Non-dimensional plot of wall pressure distributions on the flat plate.

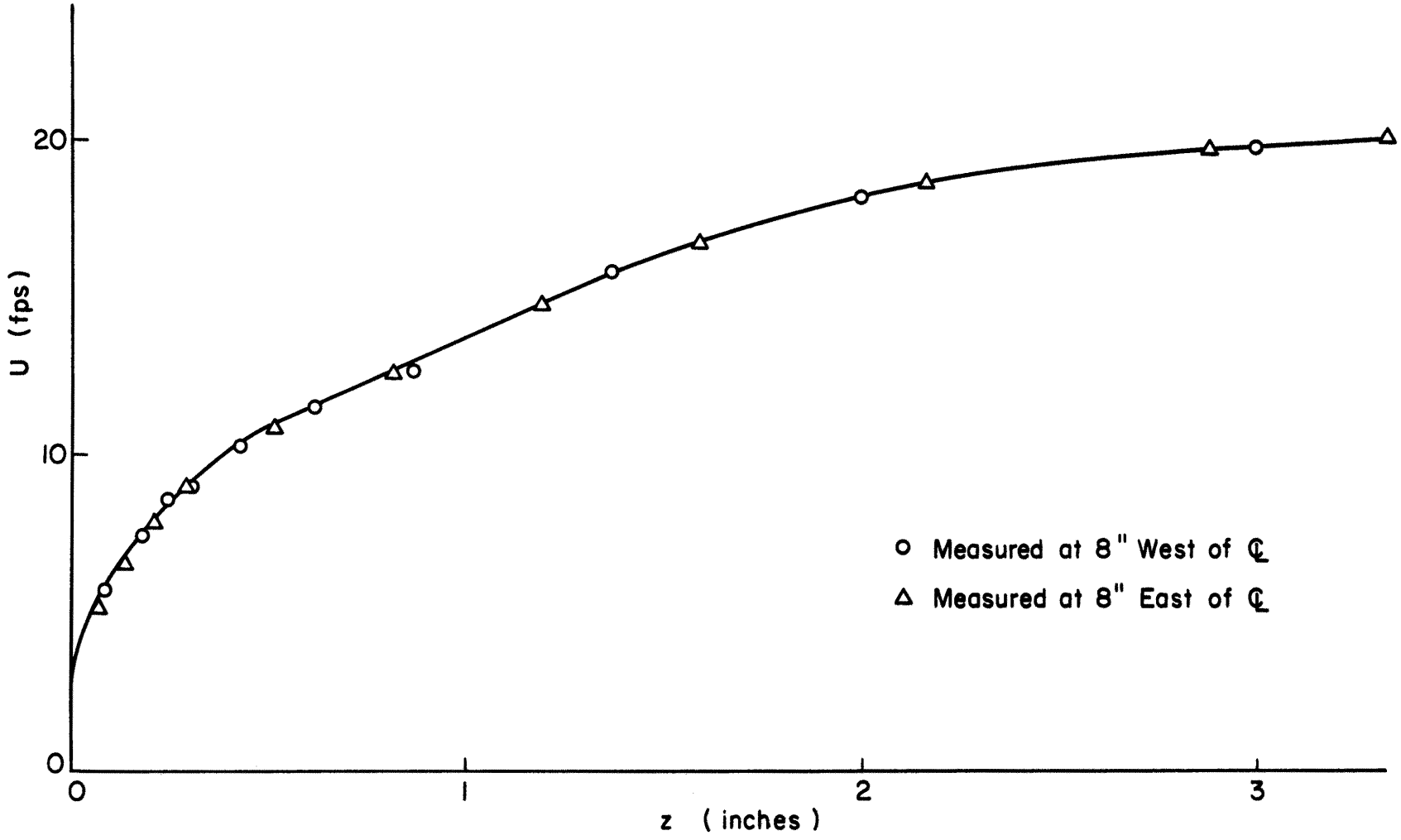

Figure 5. Mean velocity distributions at x=3 ft. to check the two-dimensionality of the flow.

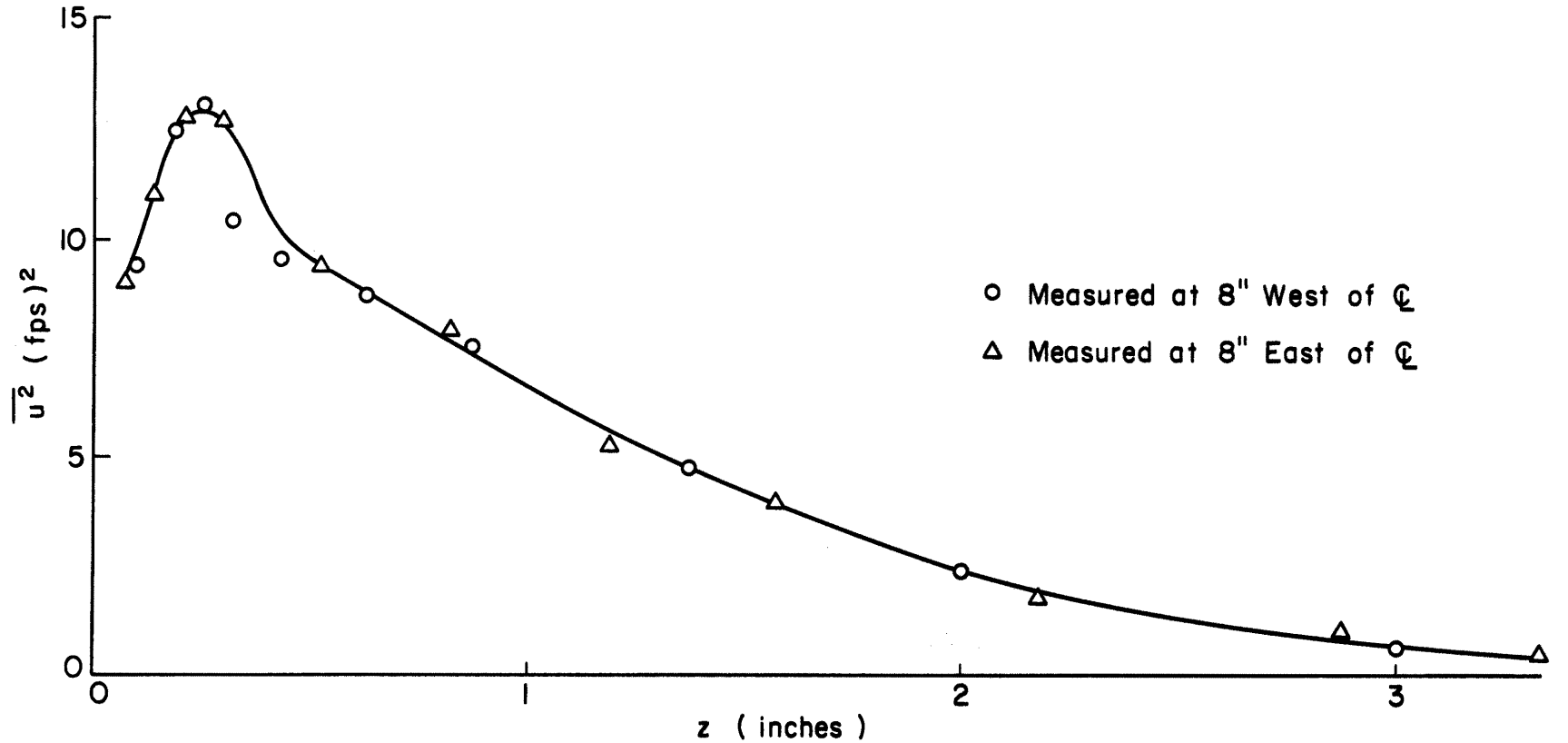

Figure 6. $\overline{u}^2$ distributions at x=3 ft. to check the two-dimensionality of the flow.

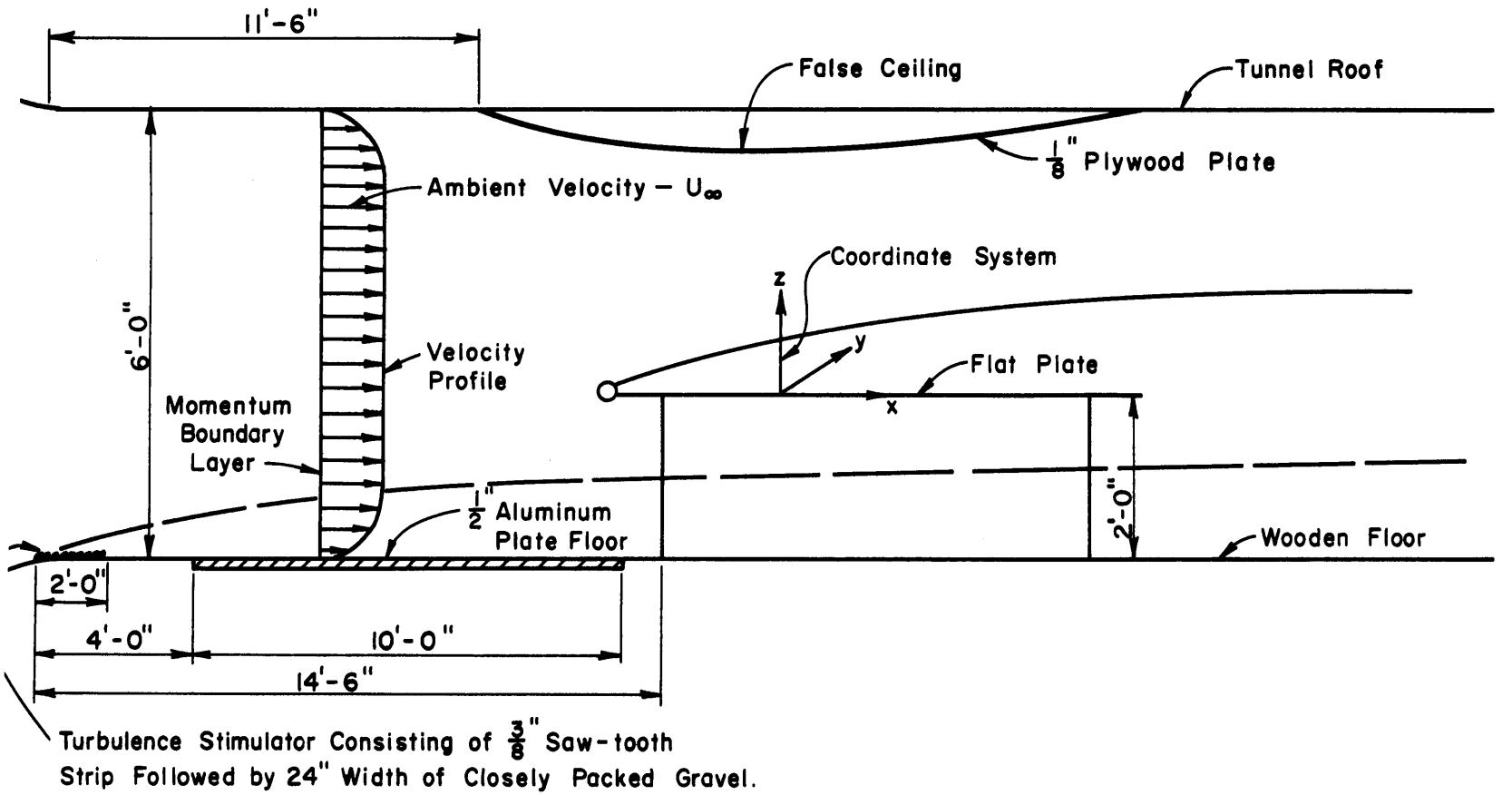

Figure 7. Test section geometry.

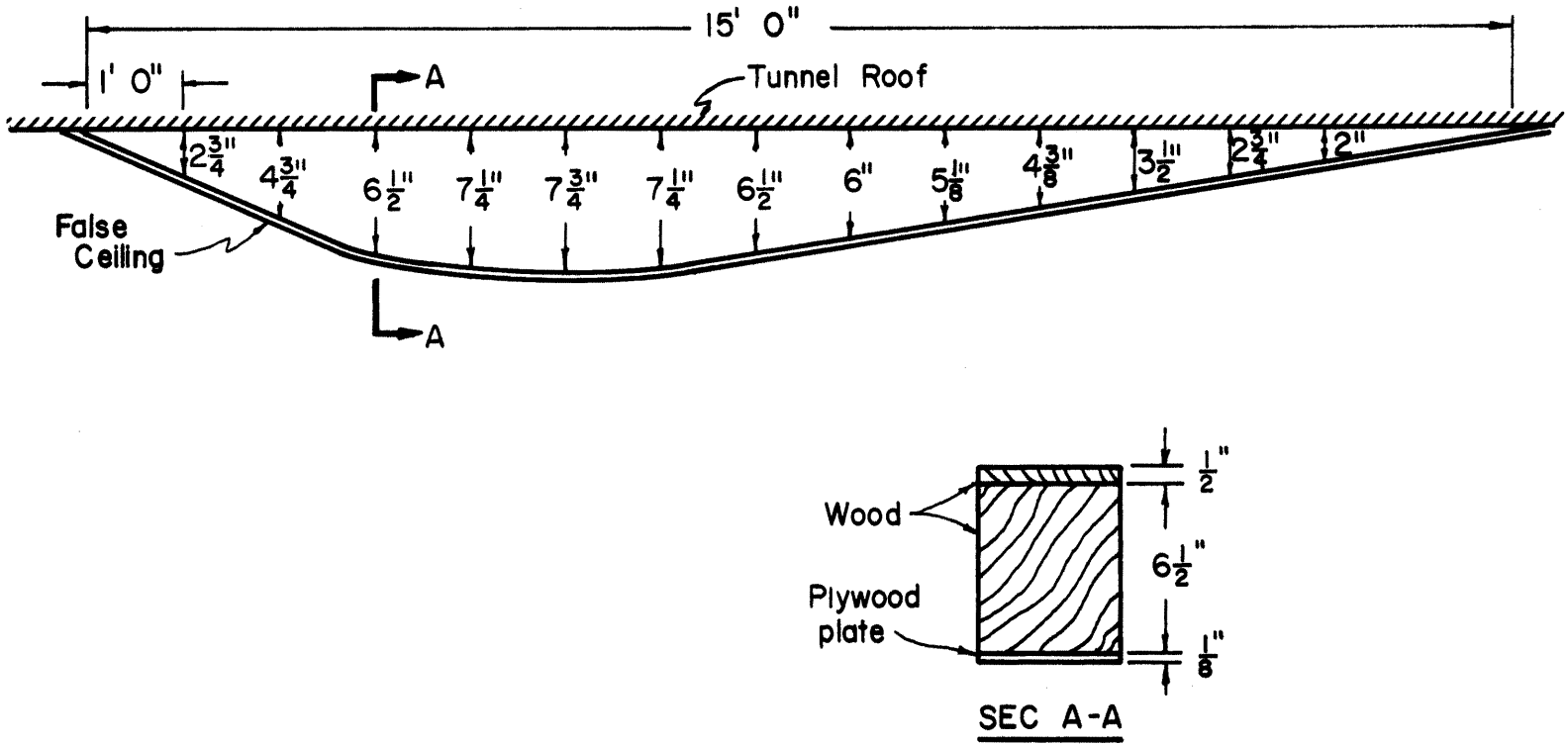

Figure 8. False wind tunnel ceiling to obtain zero pressure gradient over flat plate.

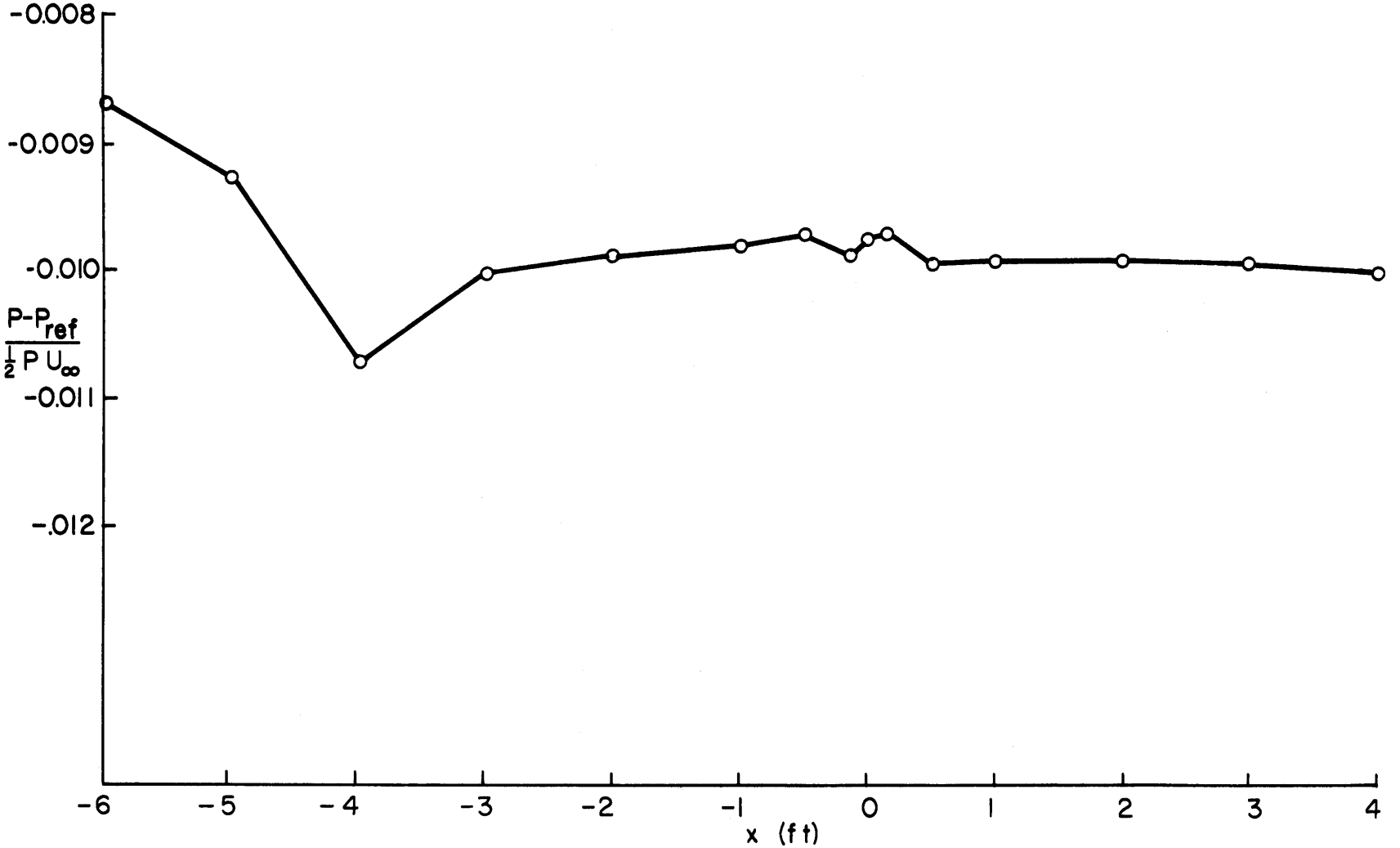

Figure 9. Non-dimensional plot of static pressure distribution at the free stream along the flat plate (P_{ref} = wall pressure at x = - 3 ft).

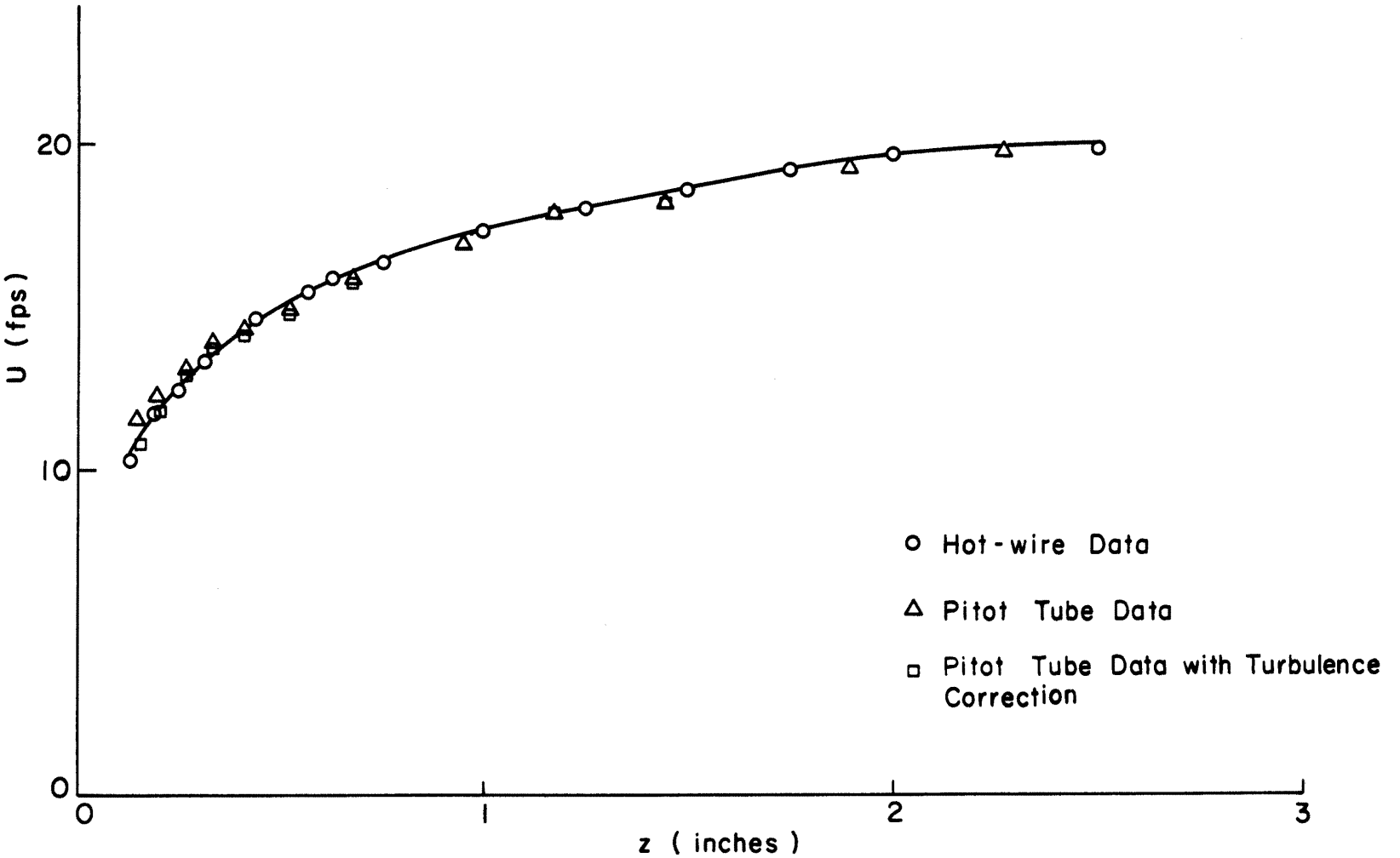

Figure 10. Comparison of mean velocity distributions measured by the hot wire and the pilot tube at x = 2 in.

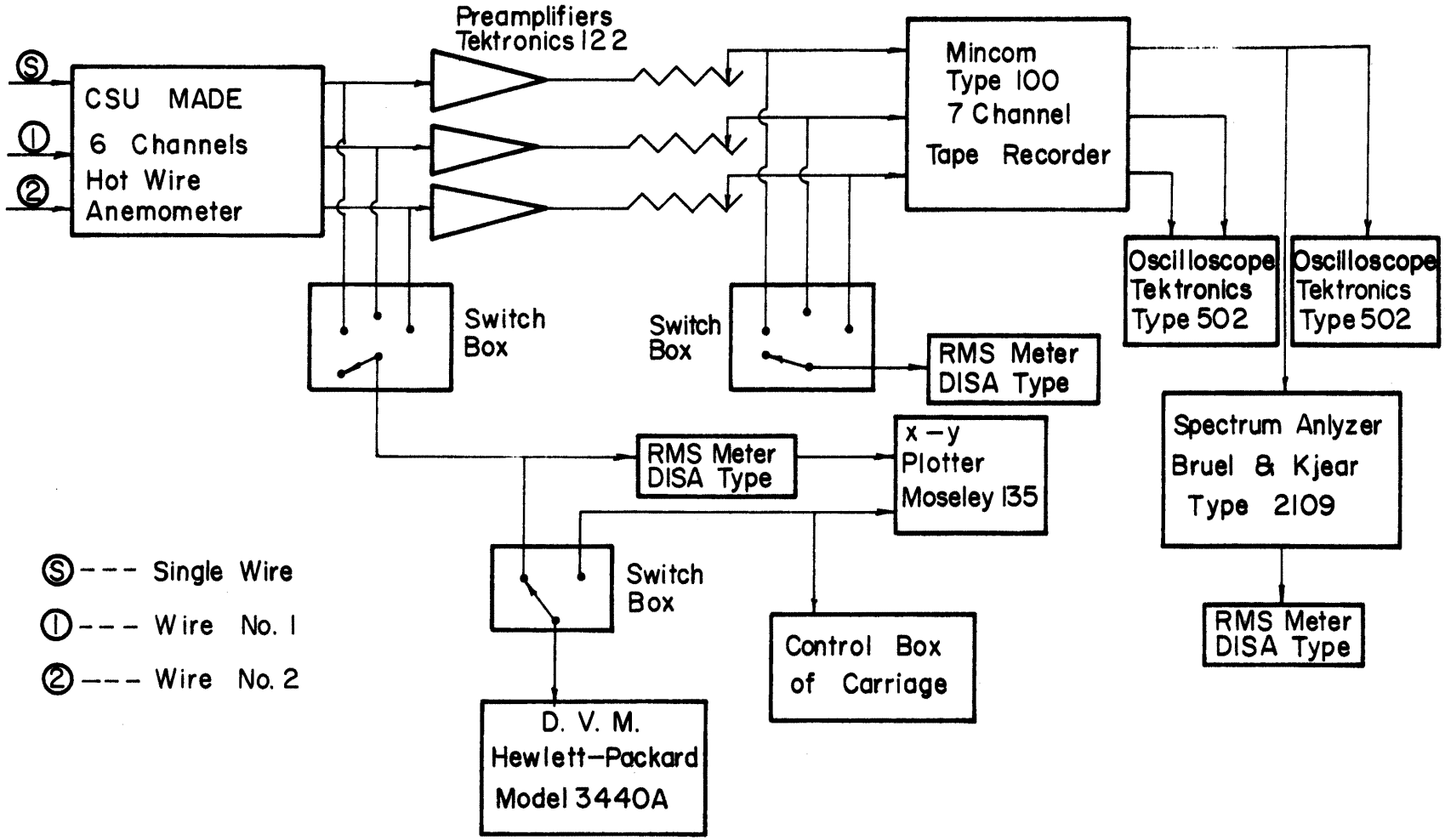

Figure 11. Block diagram for turbulence measurements.

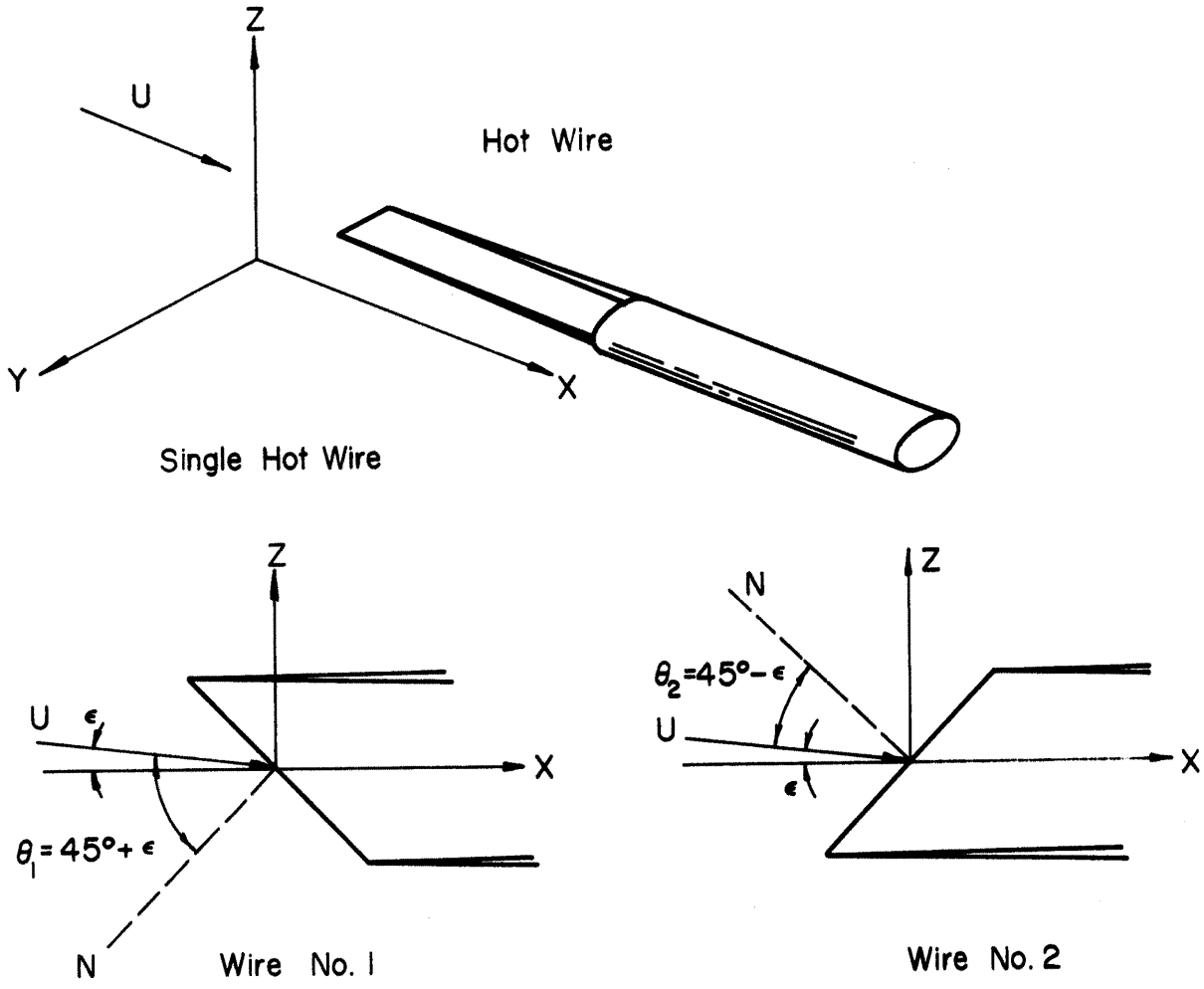

Figure 12. Coordinates of the single and crossed hot wires.

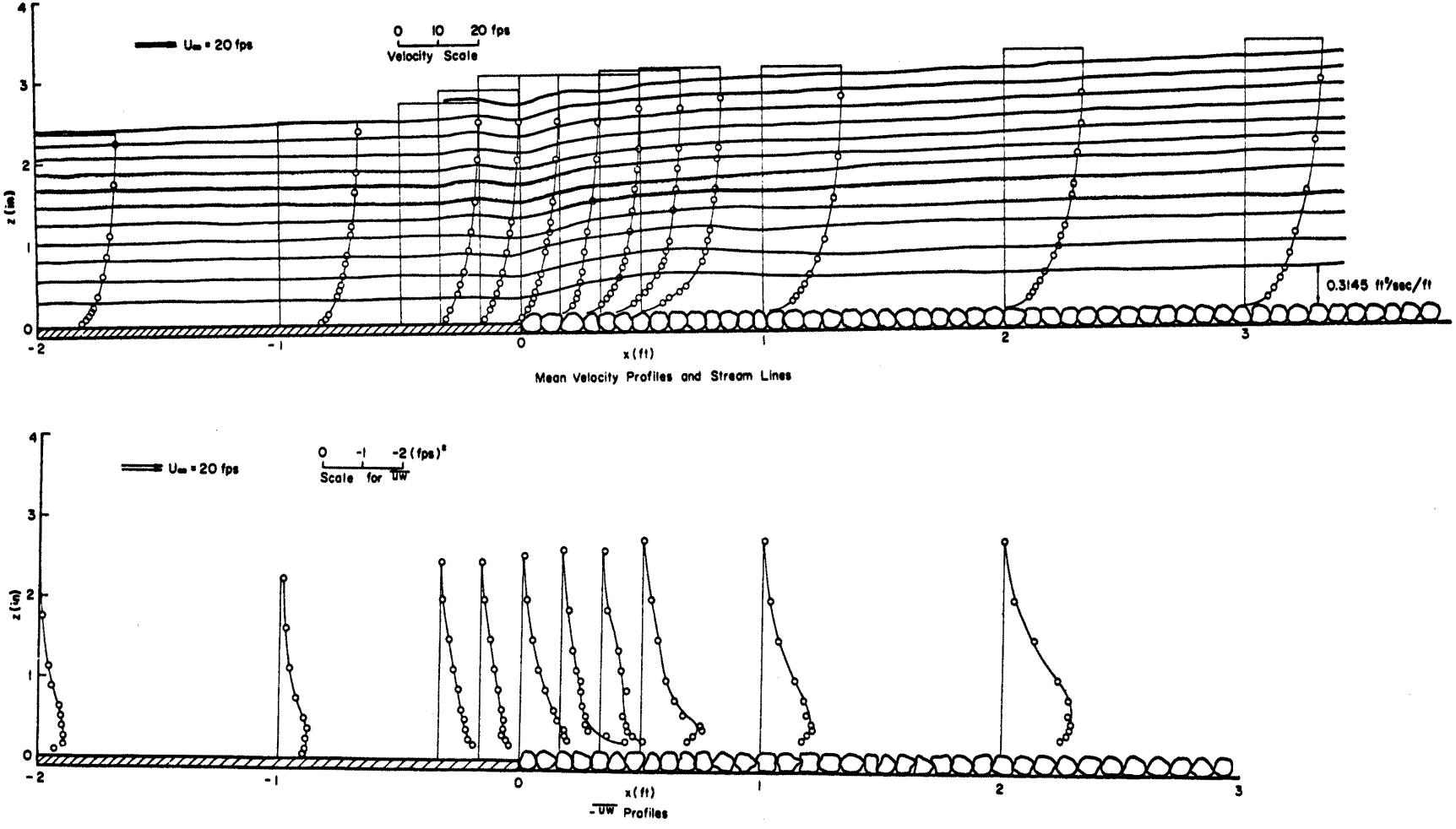

Figure 13. Mean velocity, streamline and $-\overline{uw}$ distributions in the x-z plane for Case I.

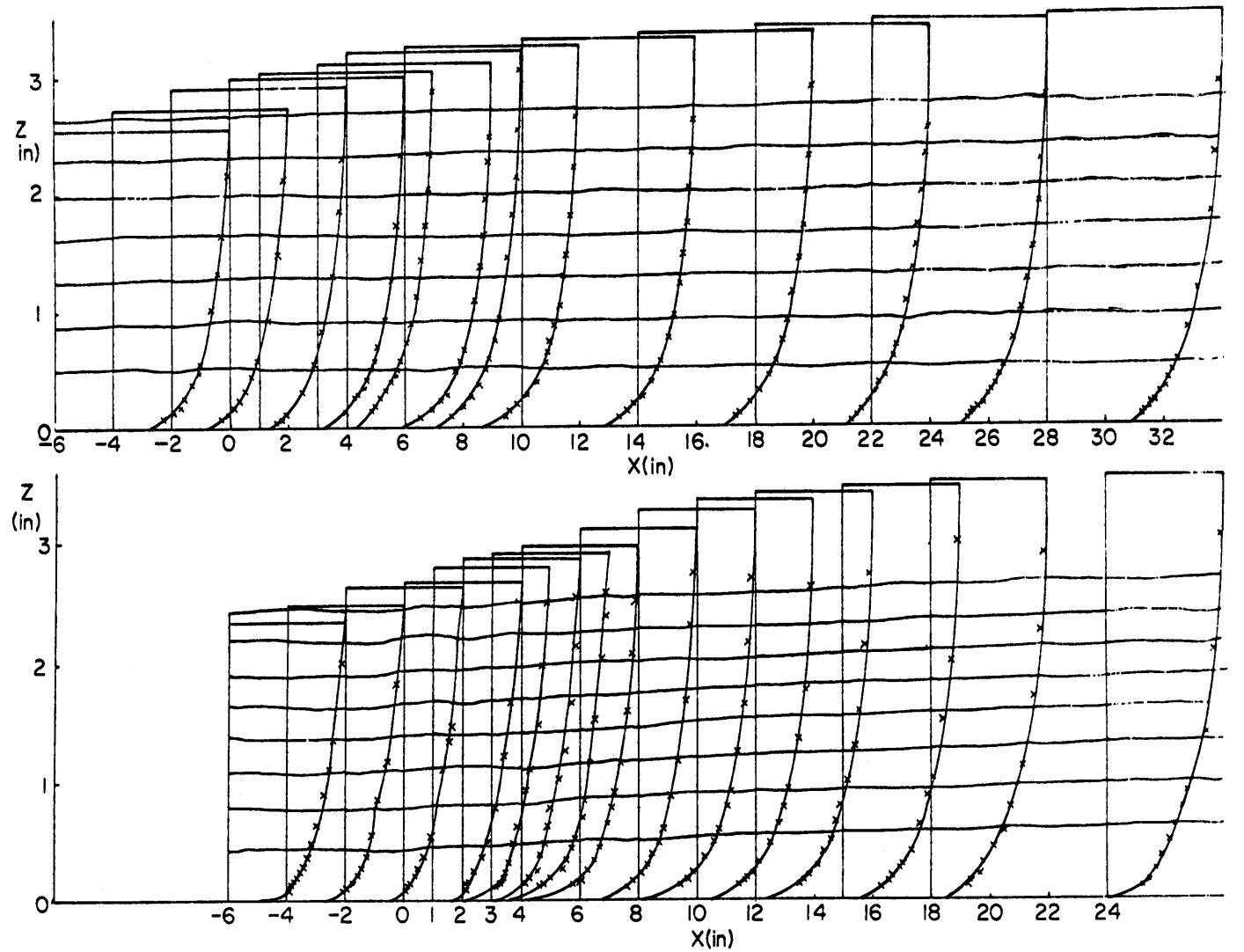

Figure 14. Mean velocity and streamline distributions in the x-z plane for Cases II and III.

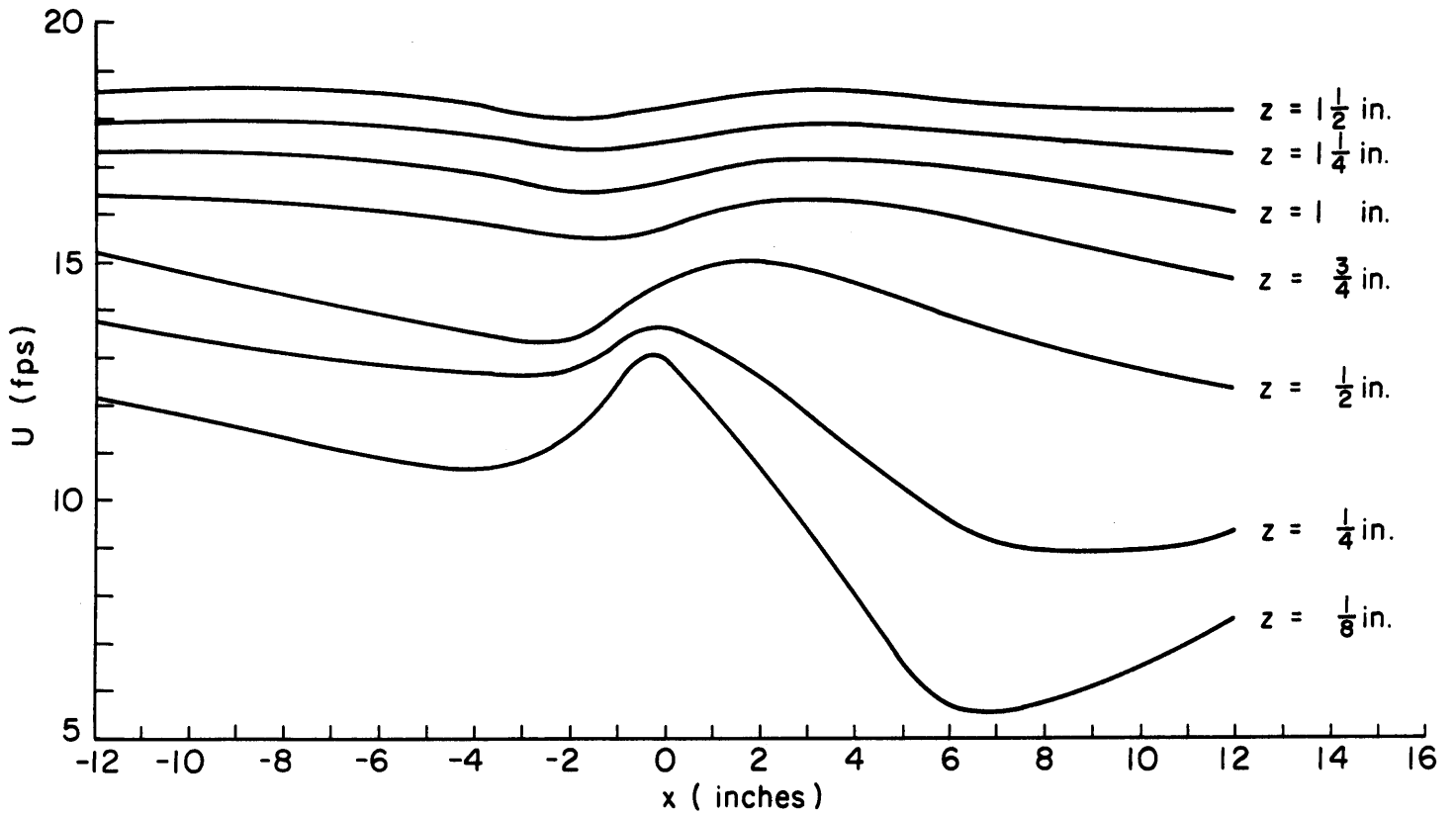

Figure 15. Longitudinal velocity distributions for Case I.

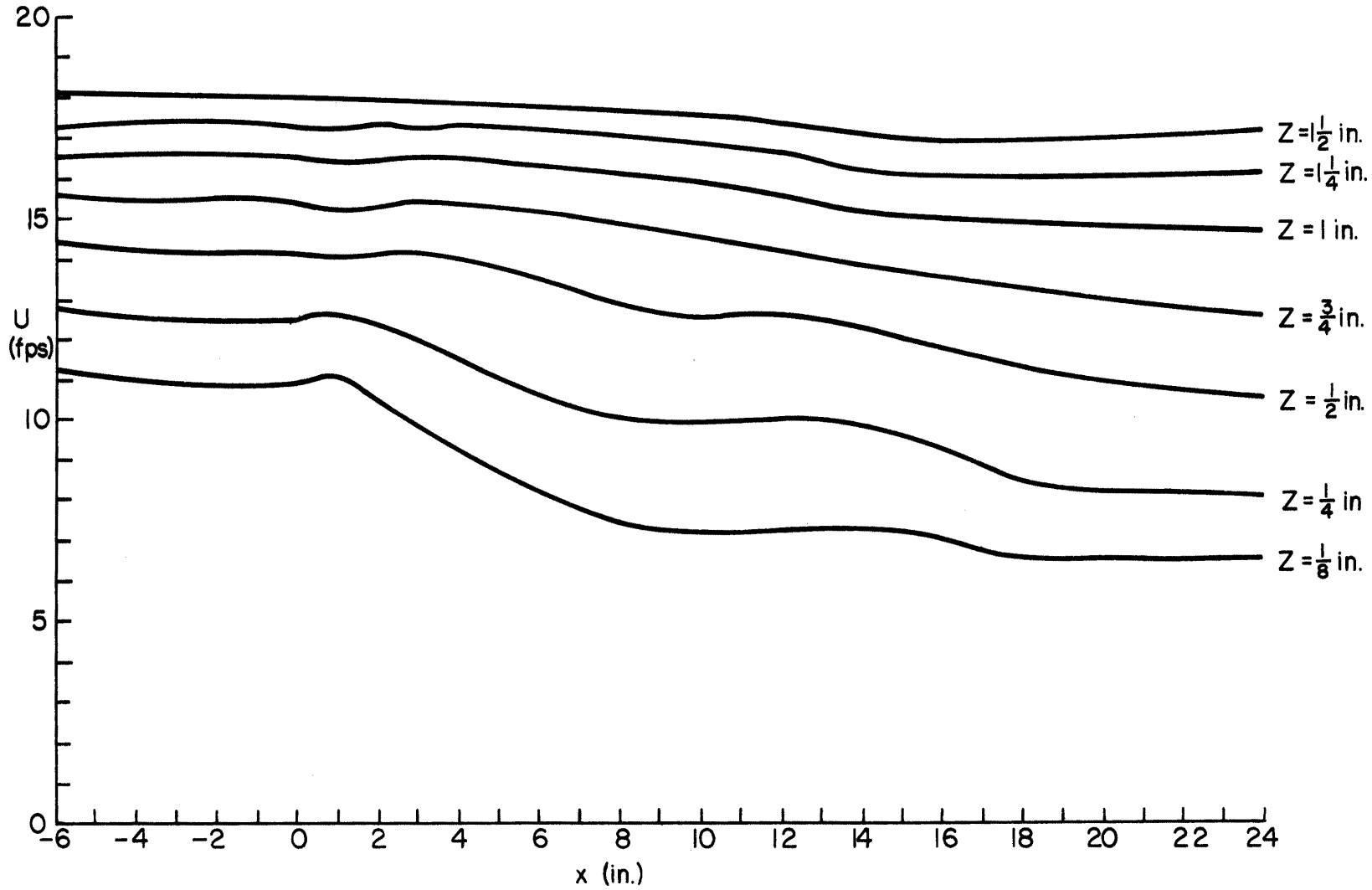

Figure 16. Longitudinal velocity distributions for Case II.

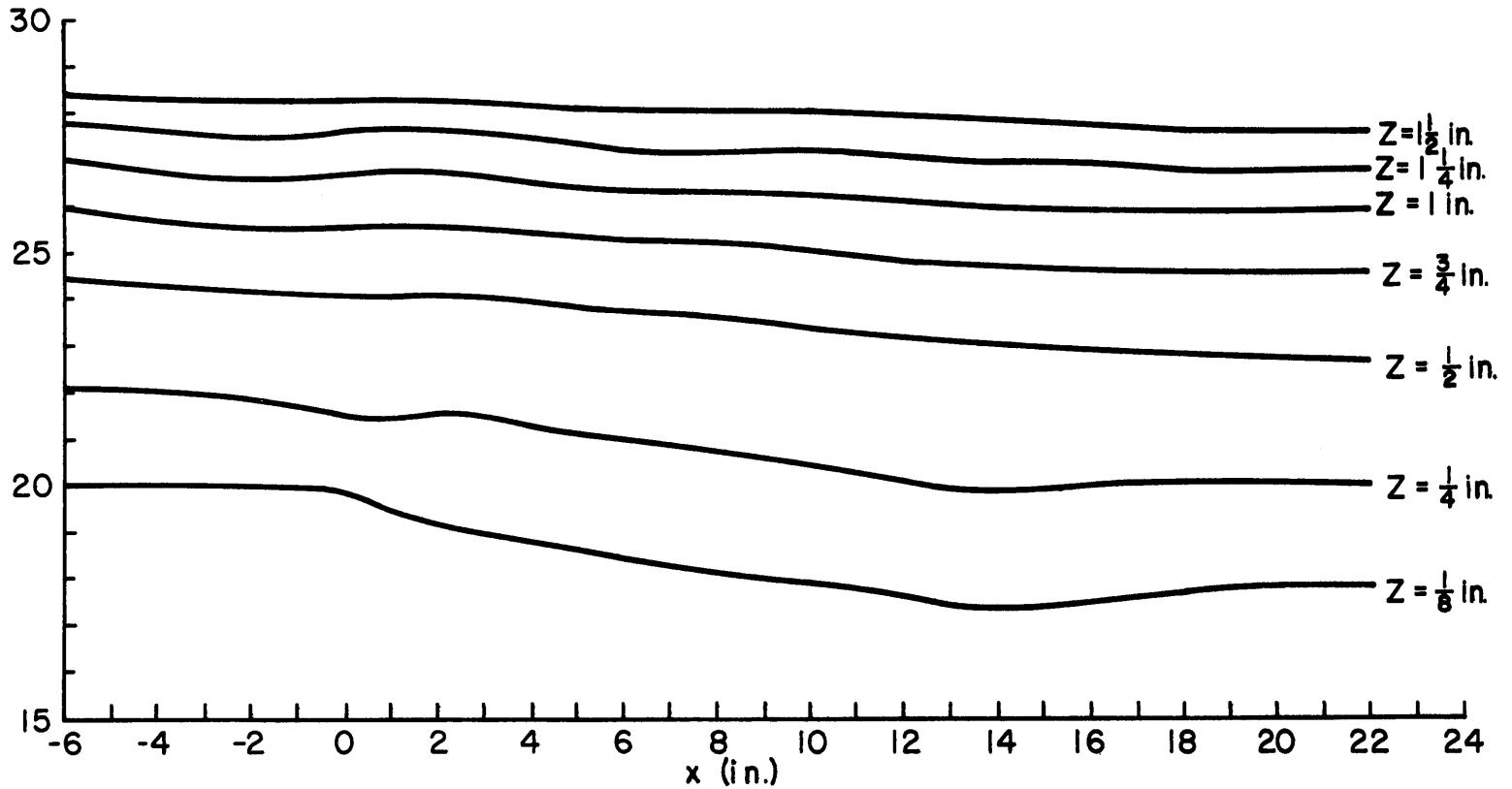

Figure 17. Longitudinal velocity distributions for Case III.

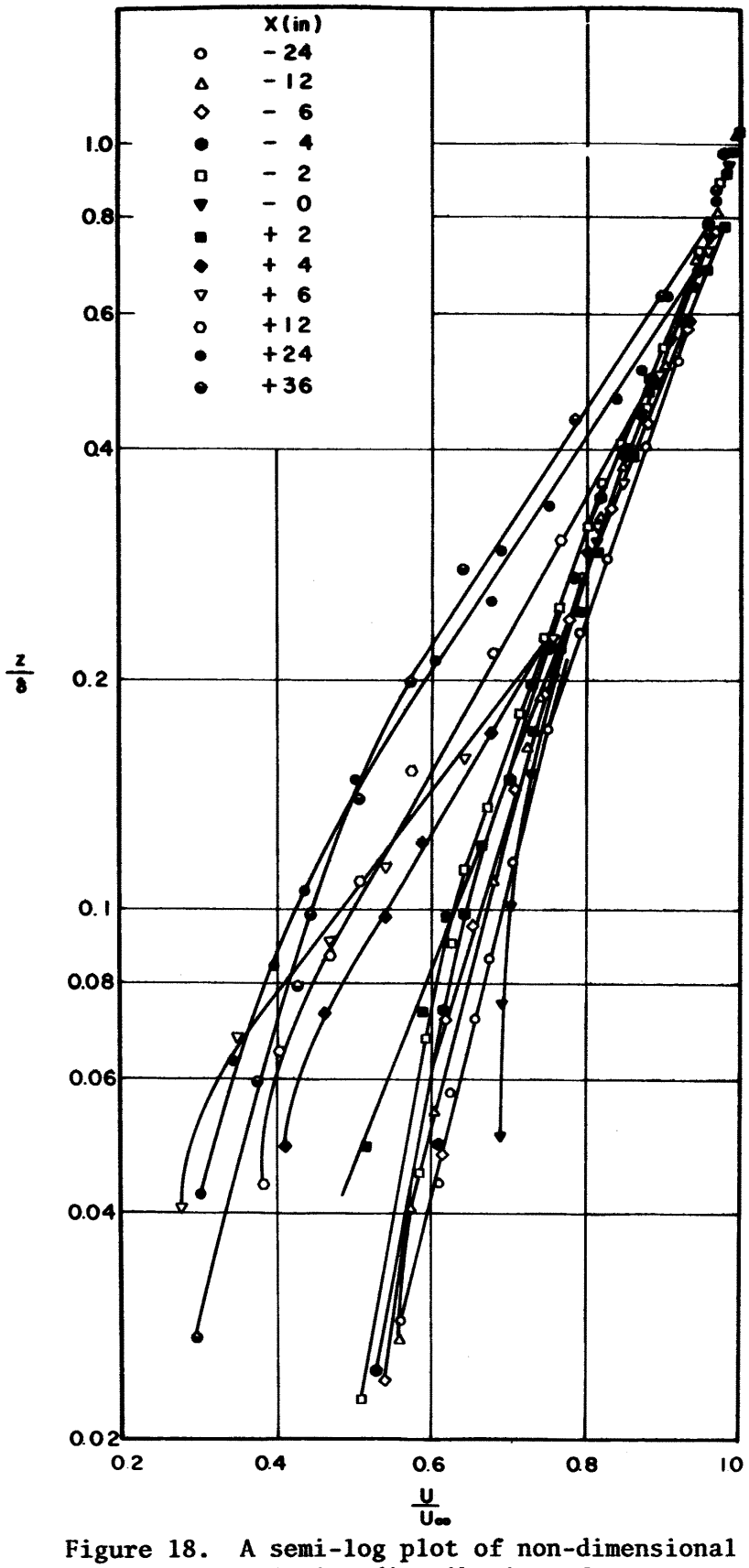

Figure 18. A semi-log plot of non-dimensional velocity distributions for Case I.

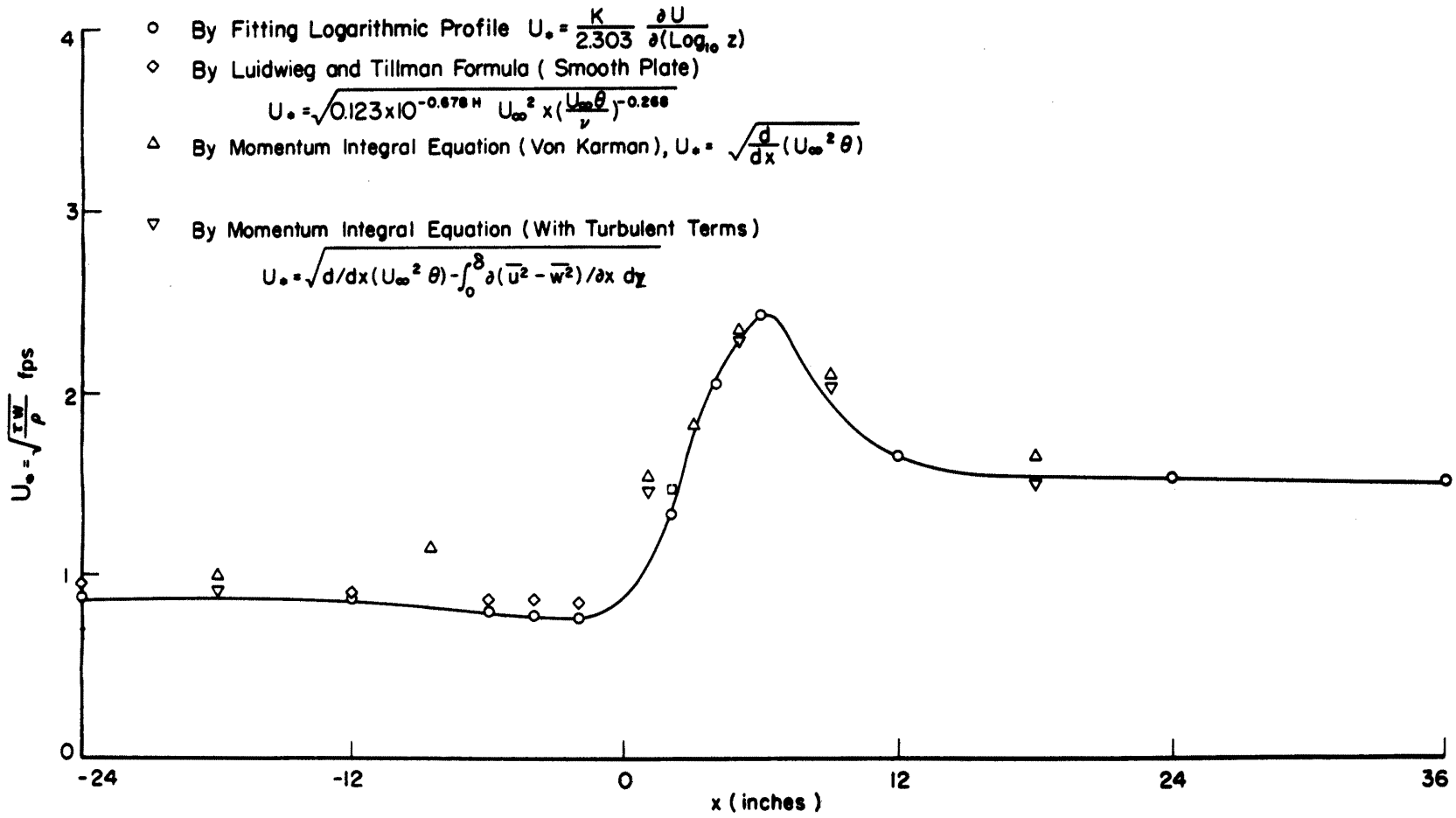

Figure 19. Shear velocity distributions for Case I.

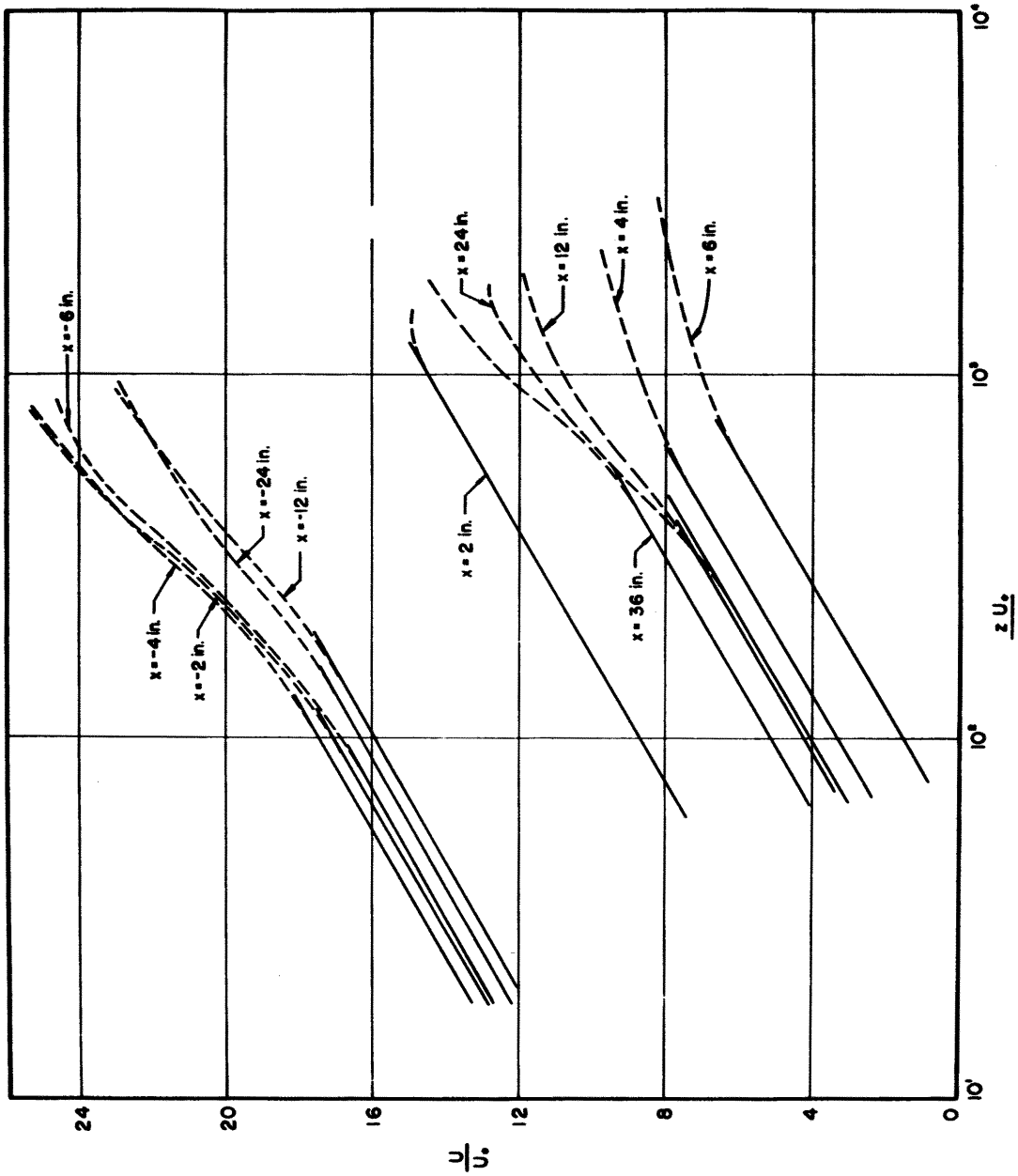

Figure 20. U/U_* vs. $\log_{10}(\frac{zU_*}{\nu})$ for Case I.

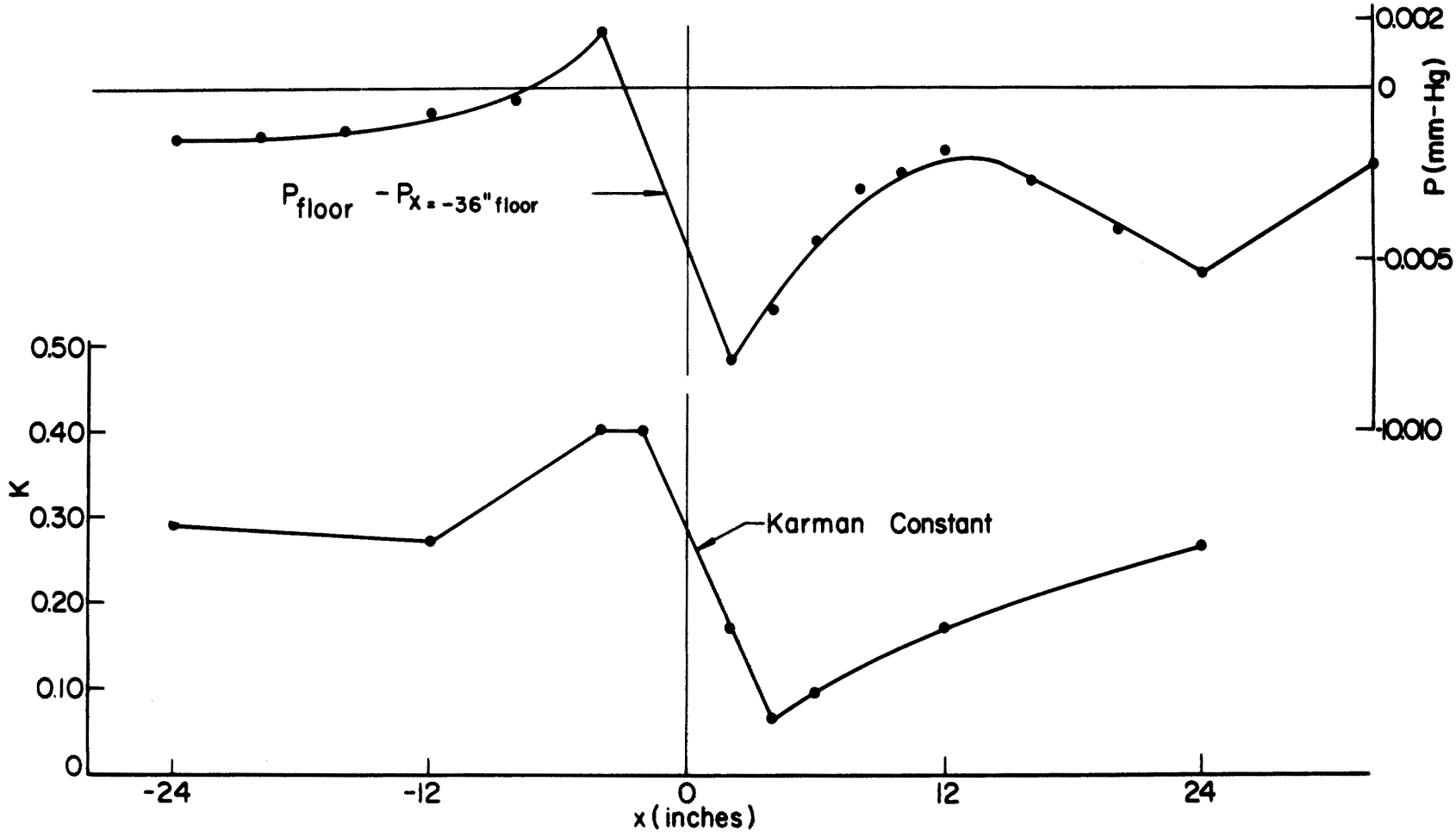

Figure 21. Kármán constant and wall pressure measurements for Case I.

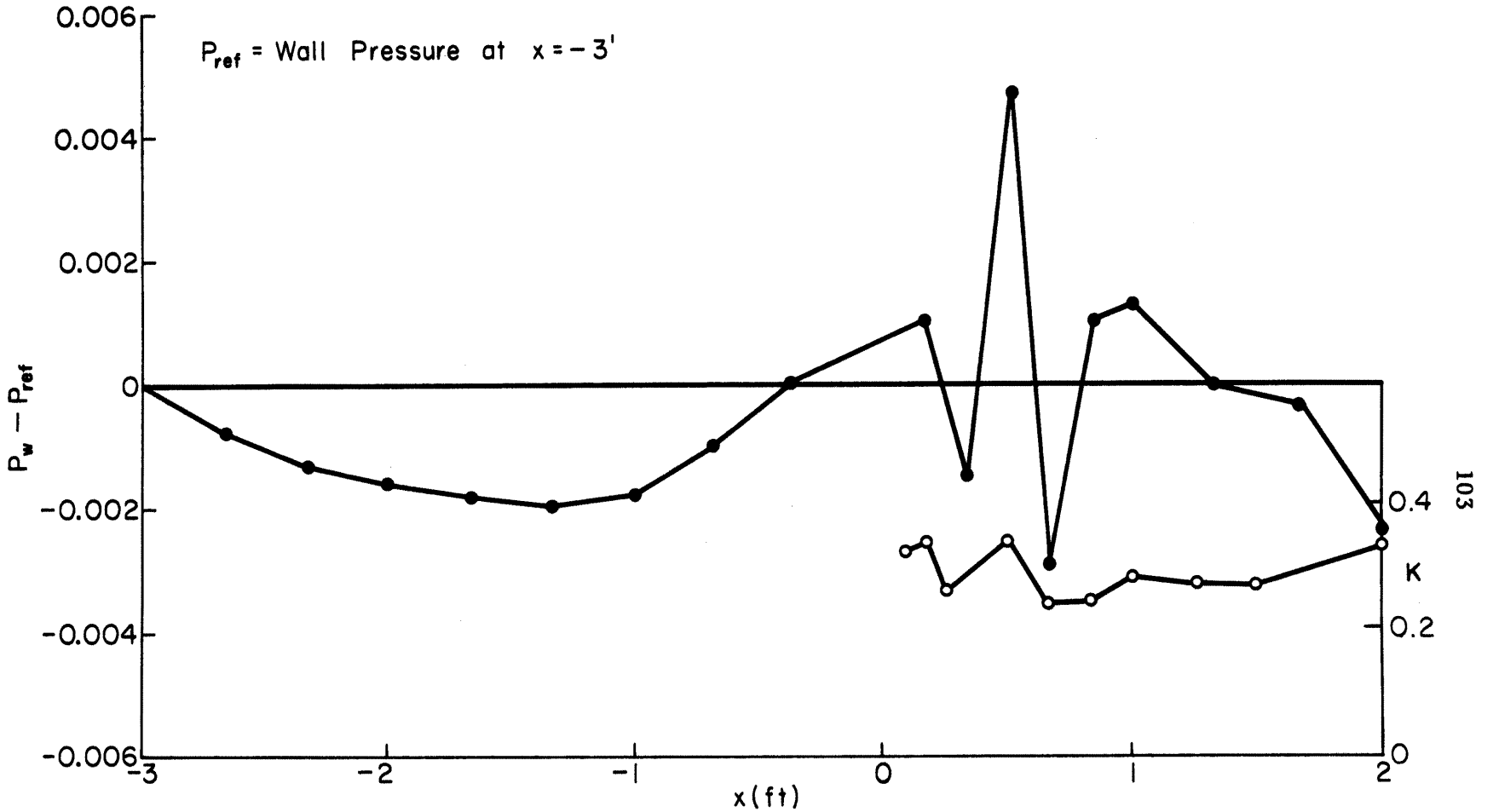

Figure 22. Kármán constant and wall pressure measurements for Case II.

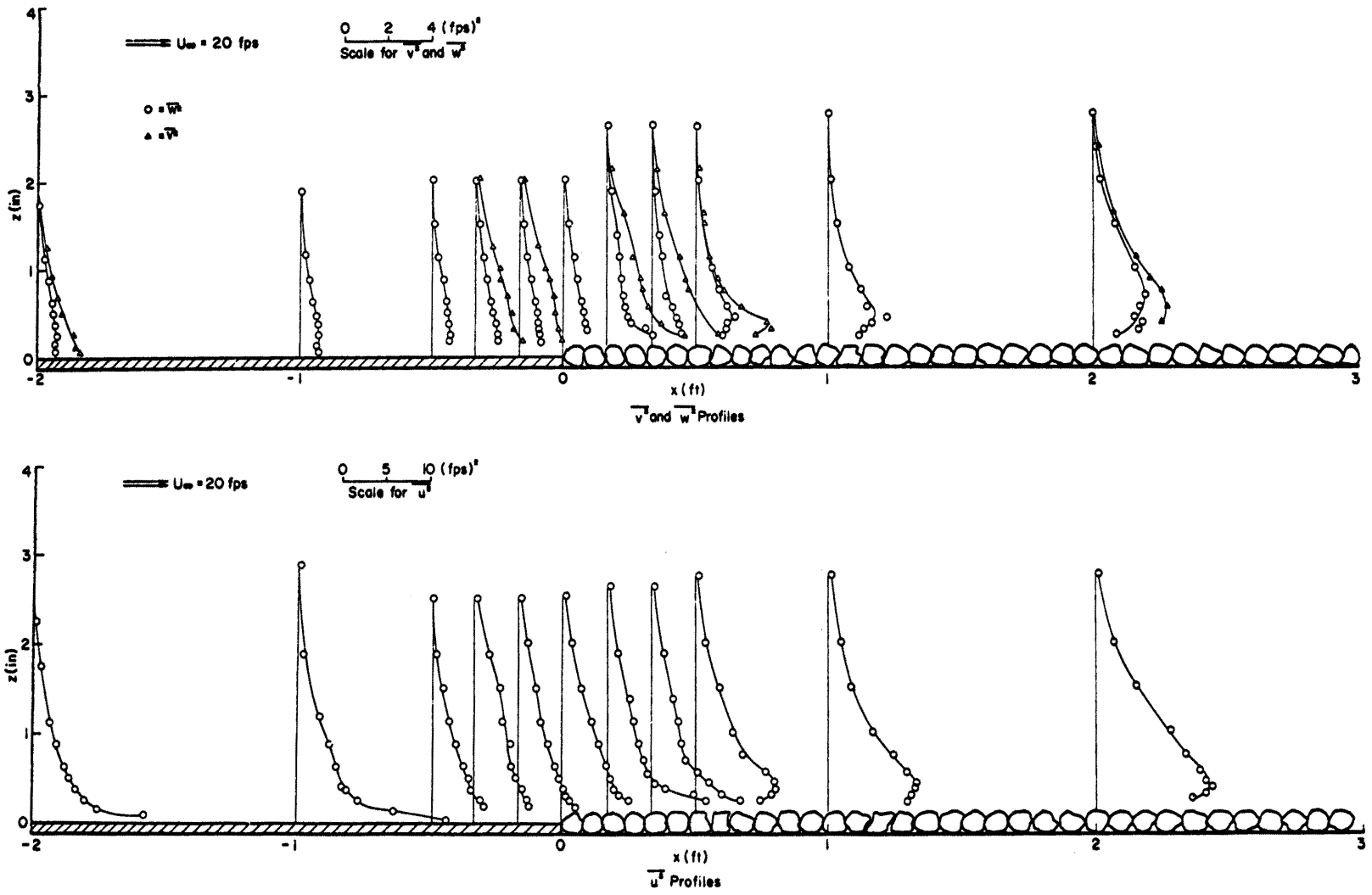

Figure 23. $\overline{u}^2$, $\overline{v}^2$, and $\overline{w}^2$ distributions for Case I.

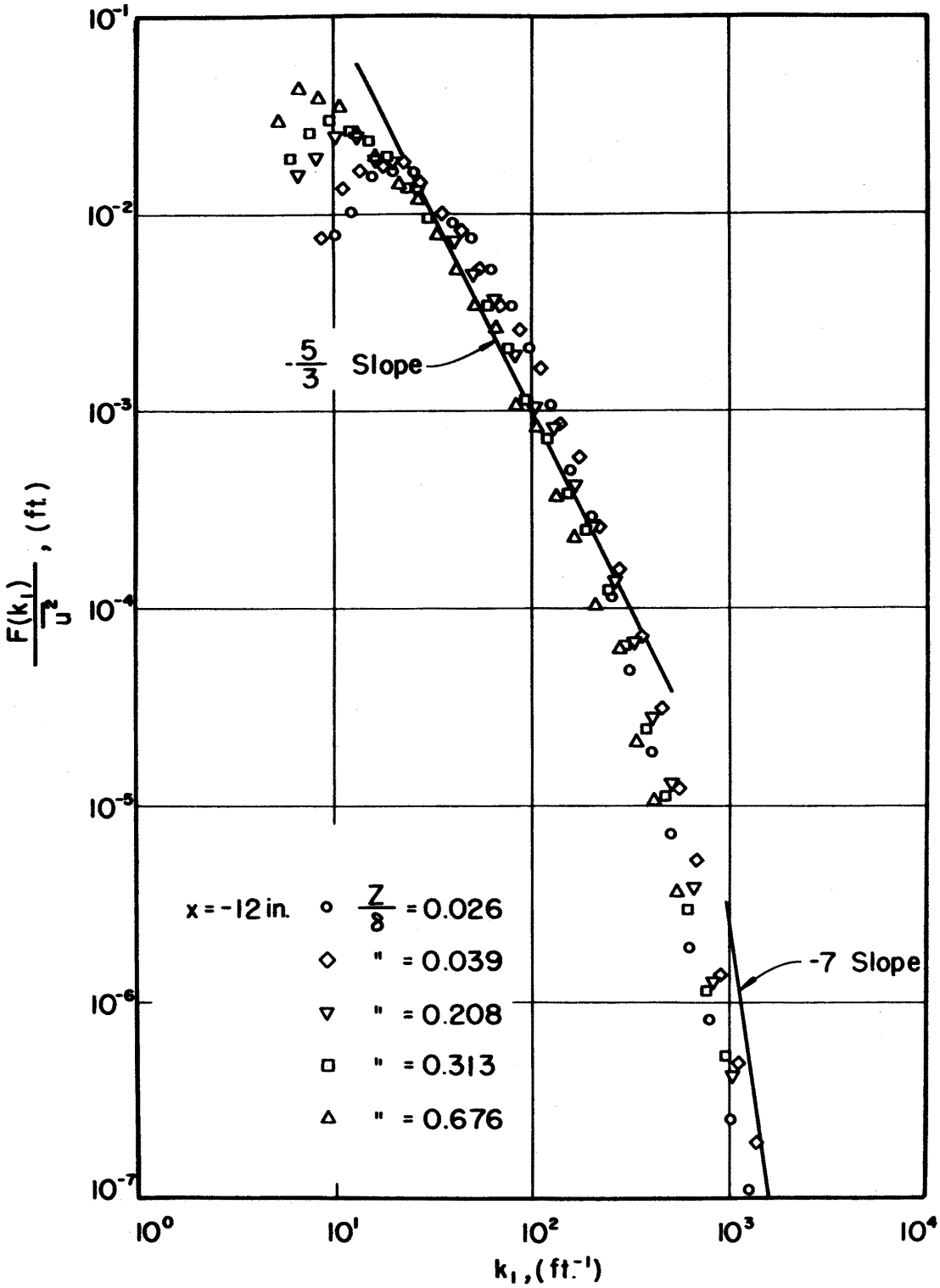

Figure 24. Normalized spectra of longitudinal velocity fluctuations at x=-12 in. for Case I.

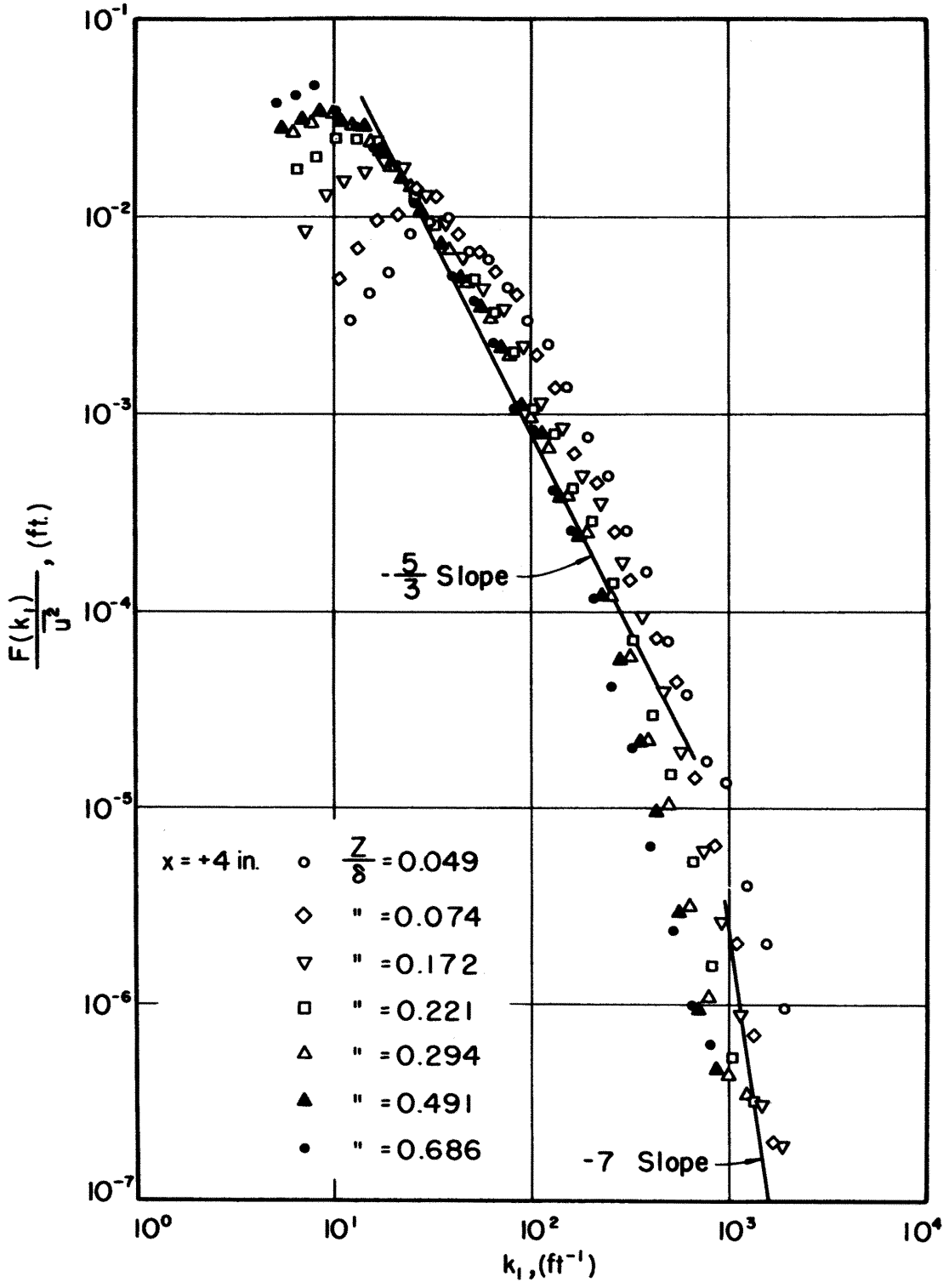

Figure 25. Normalized spectra of longitudinal velocity fluctuations at x=4 in. for Case I.

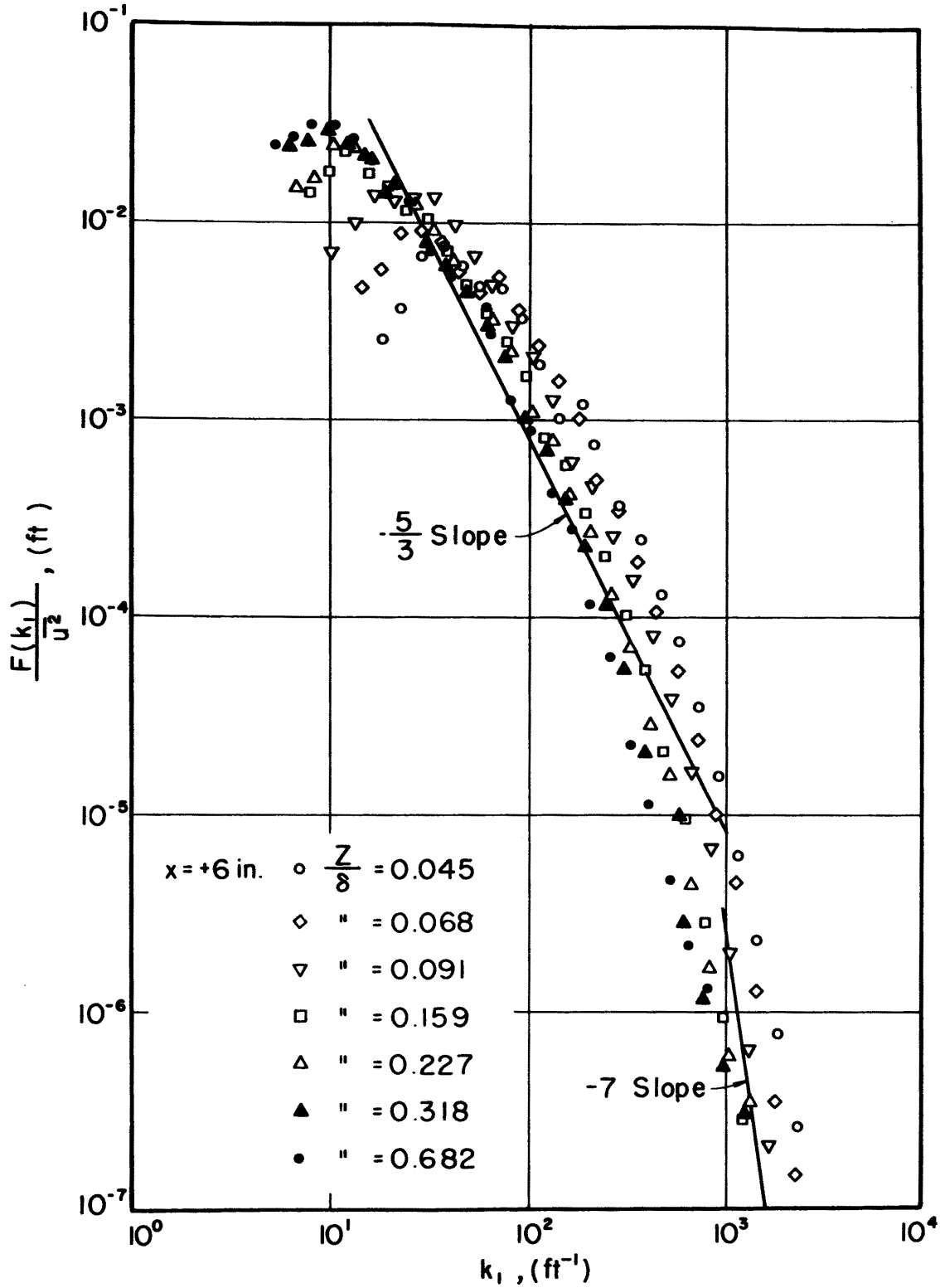

Figure 26. Normalized spectra of longitudinal velocity fluctuations at x=6 in. for Case I.

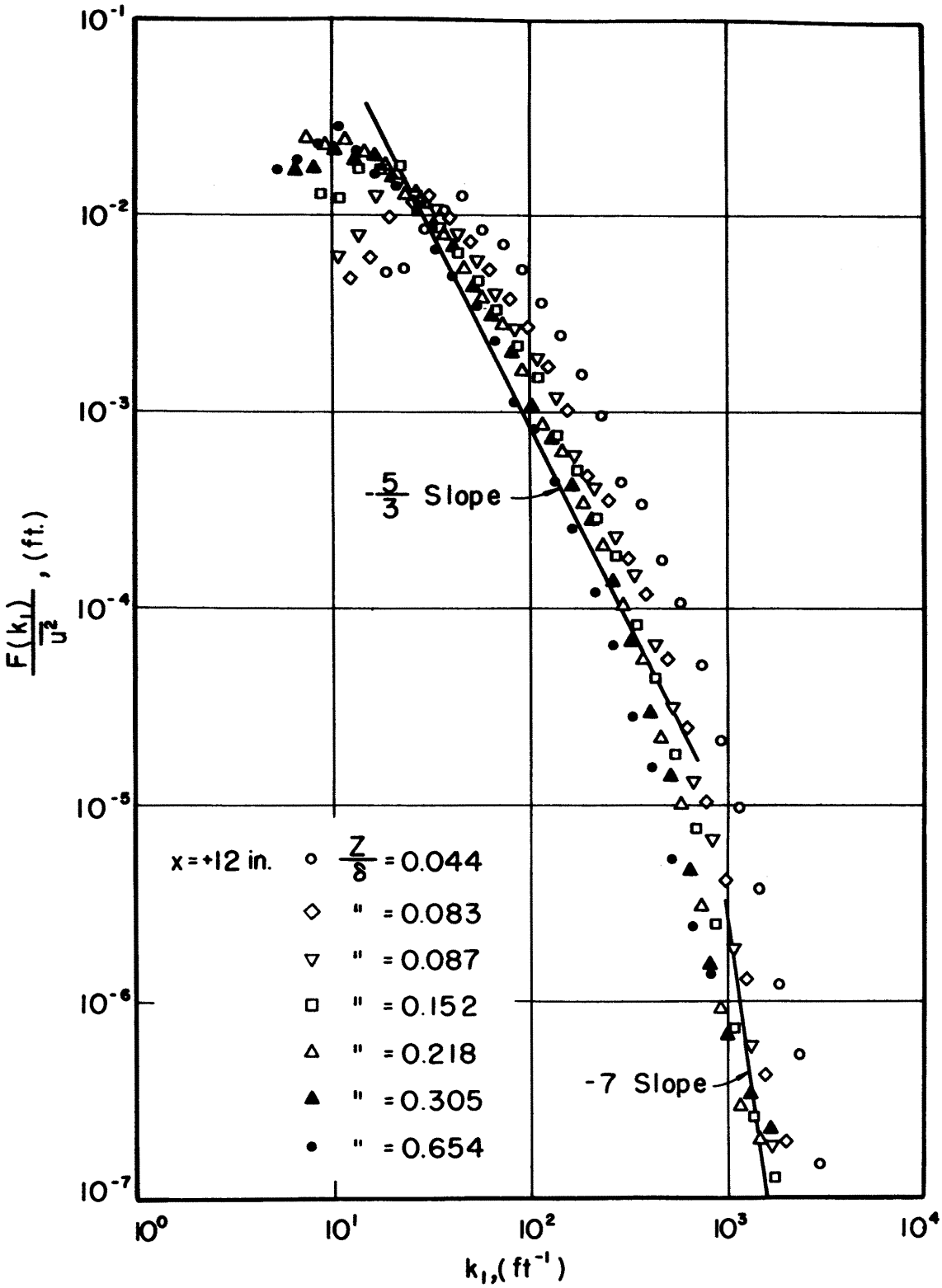

Figure 27. Normalized spectra of longitudinal velocity fluctuations at x=12 in. for Case I.

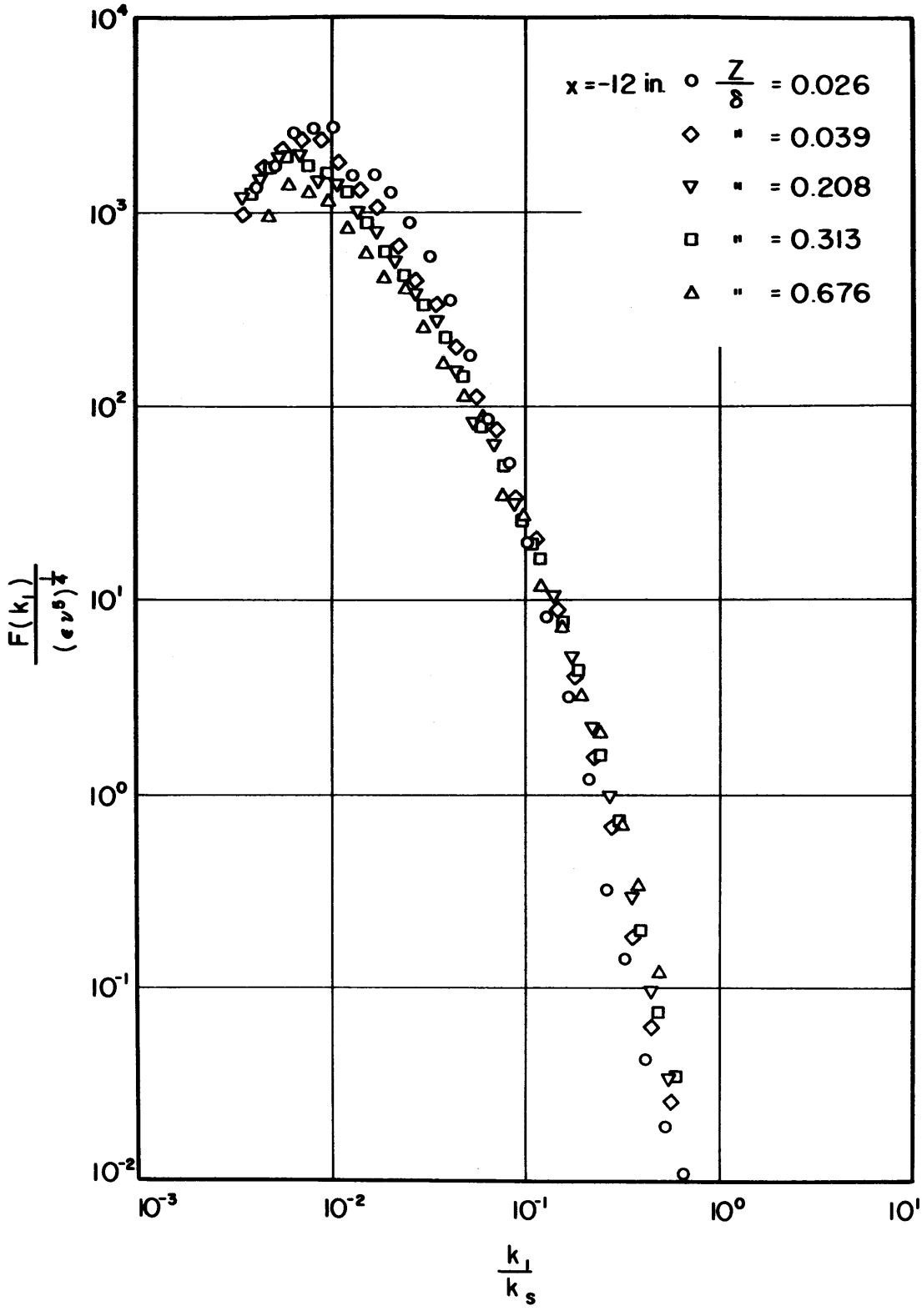

Figure 28. u'-spectra in the similarity coordinates at x=-12 in. Case I.

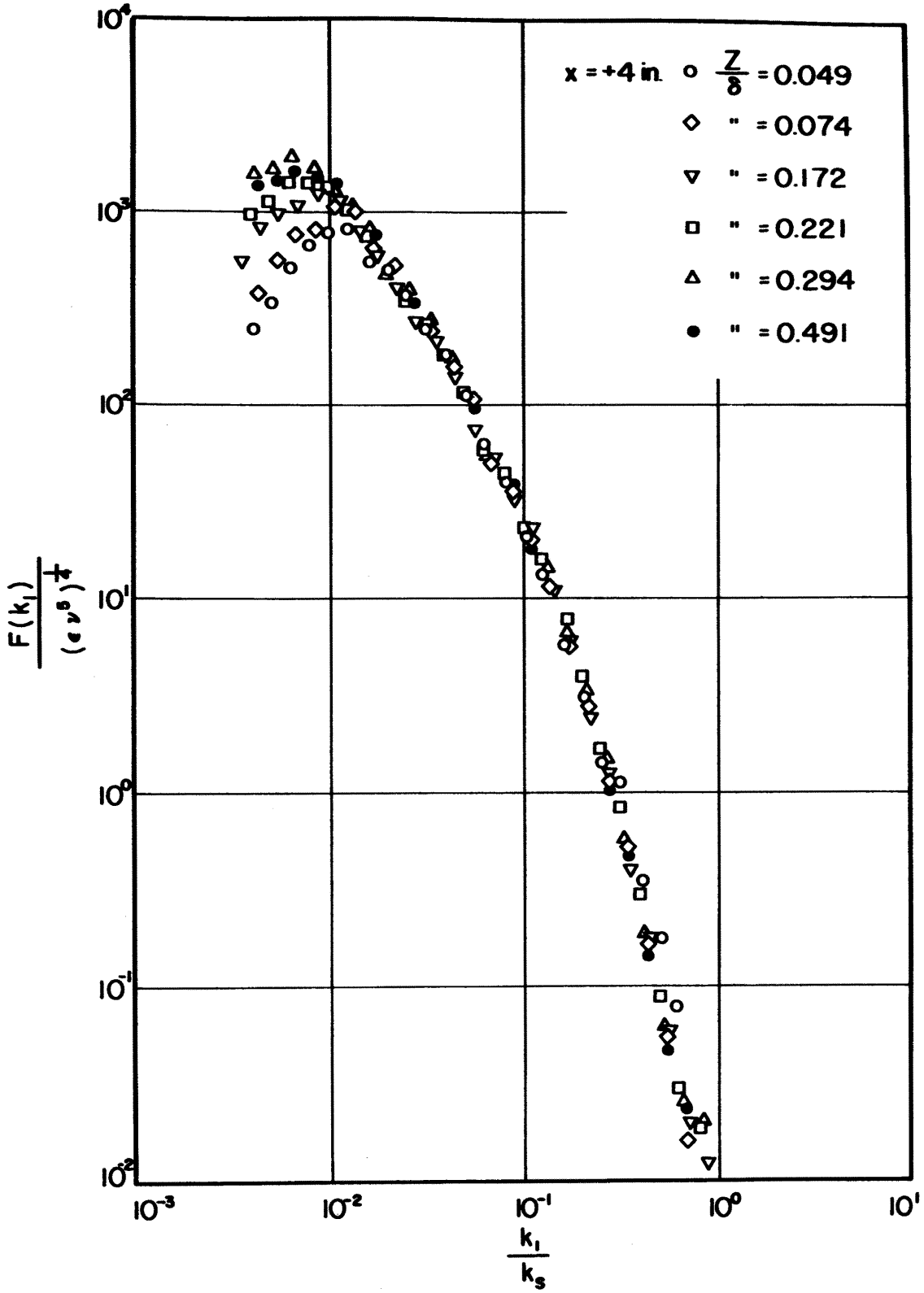

Figure 29. u'-spectra in the similarity coordinates at x=4 in. for Case I.

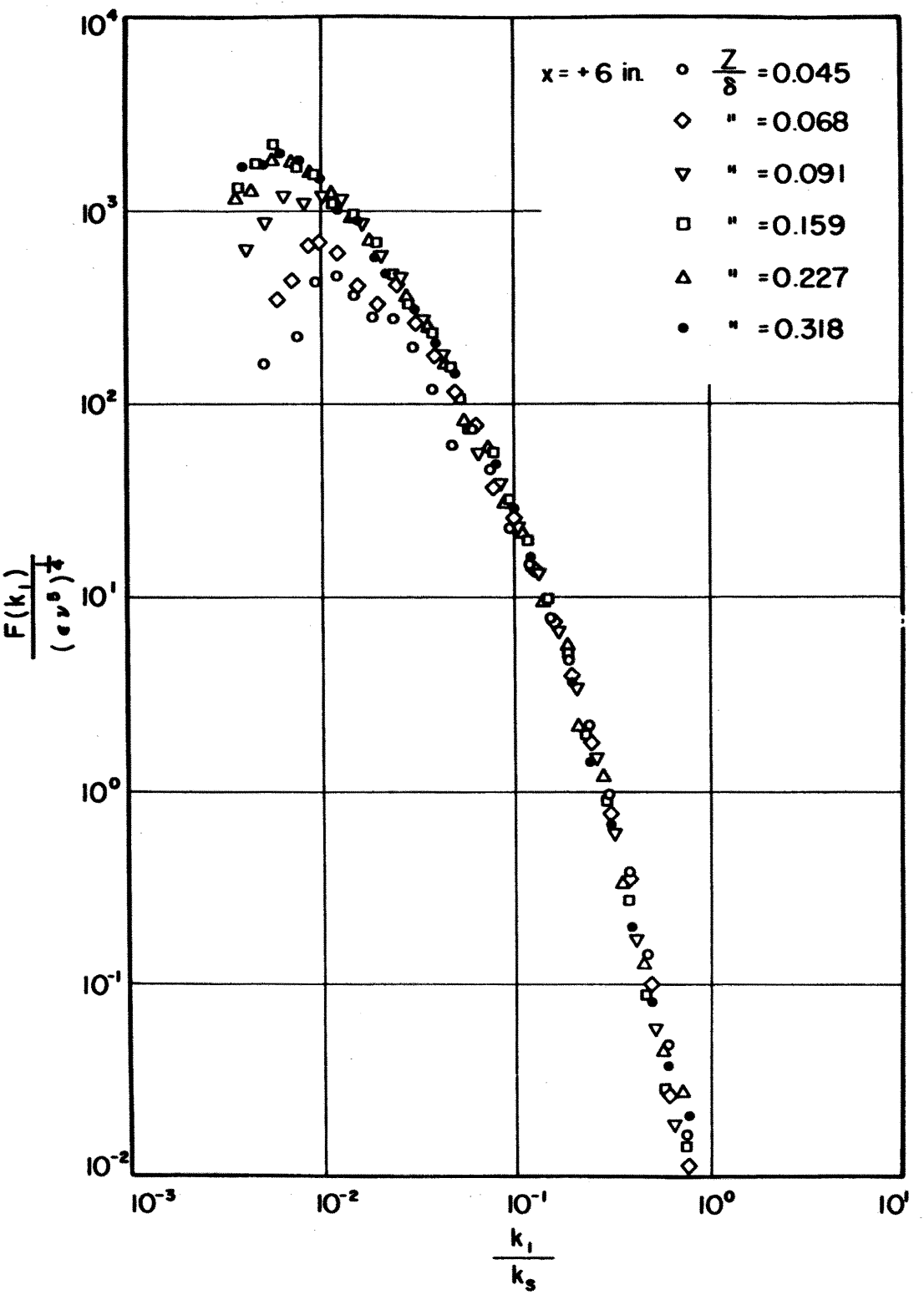

Figure 30. u'-spectra in the similarity coordinates at x=6 in. for Case I.

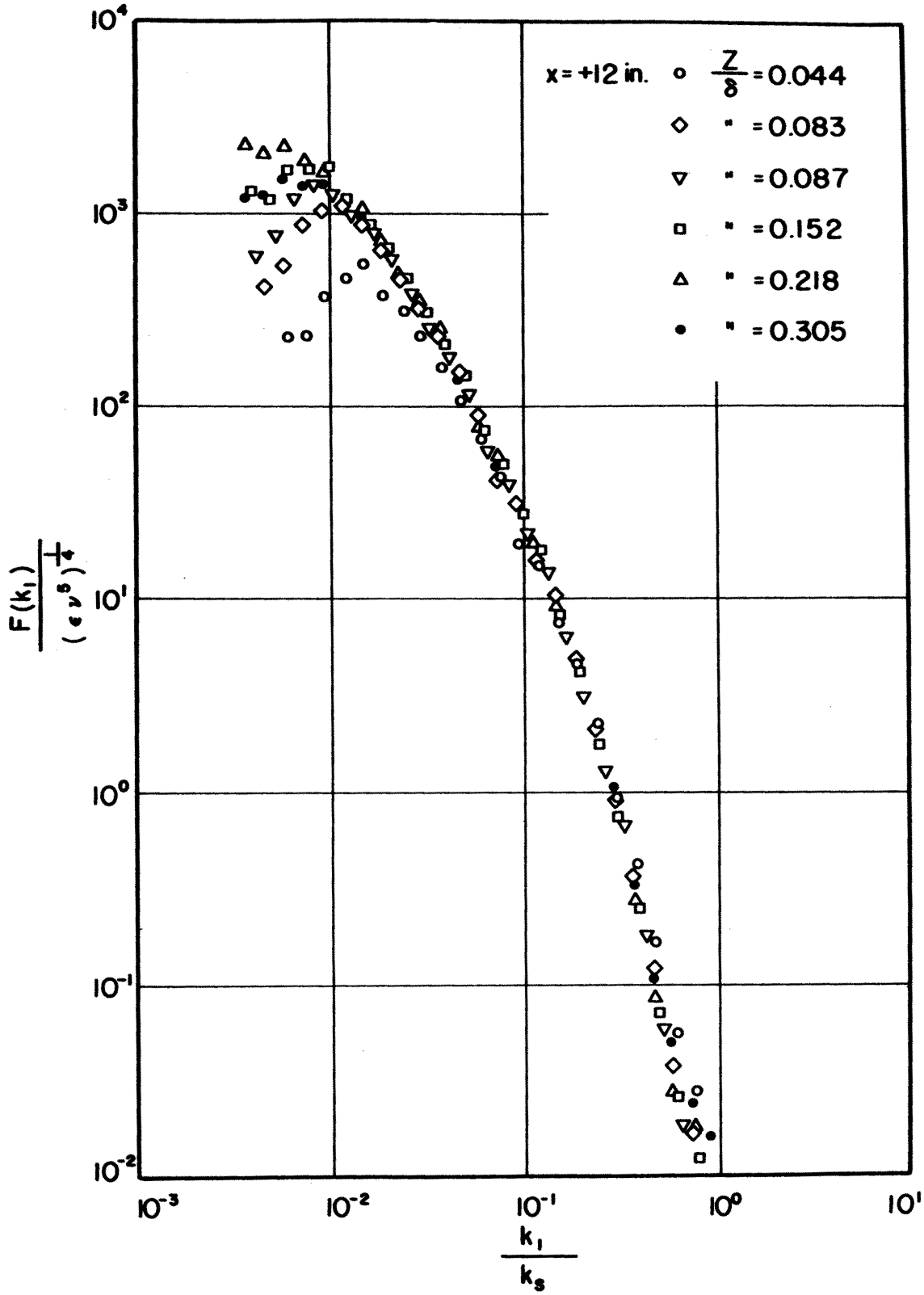

Figure 31. u'-spectra in the similarity coordinates at x=12 in. for Case I.

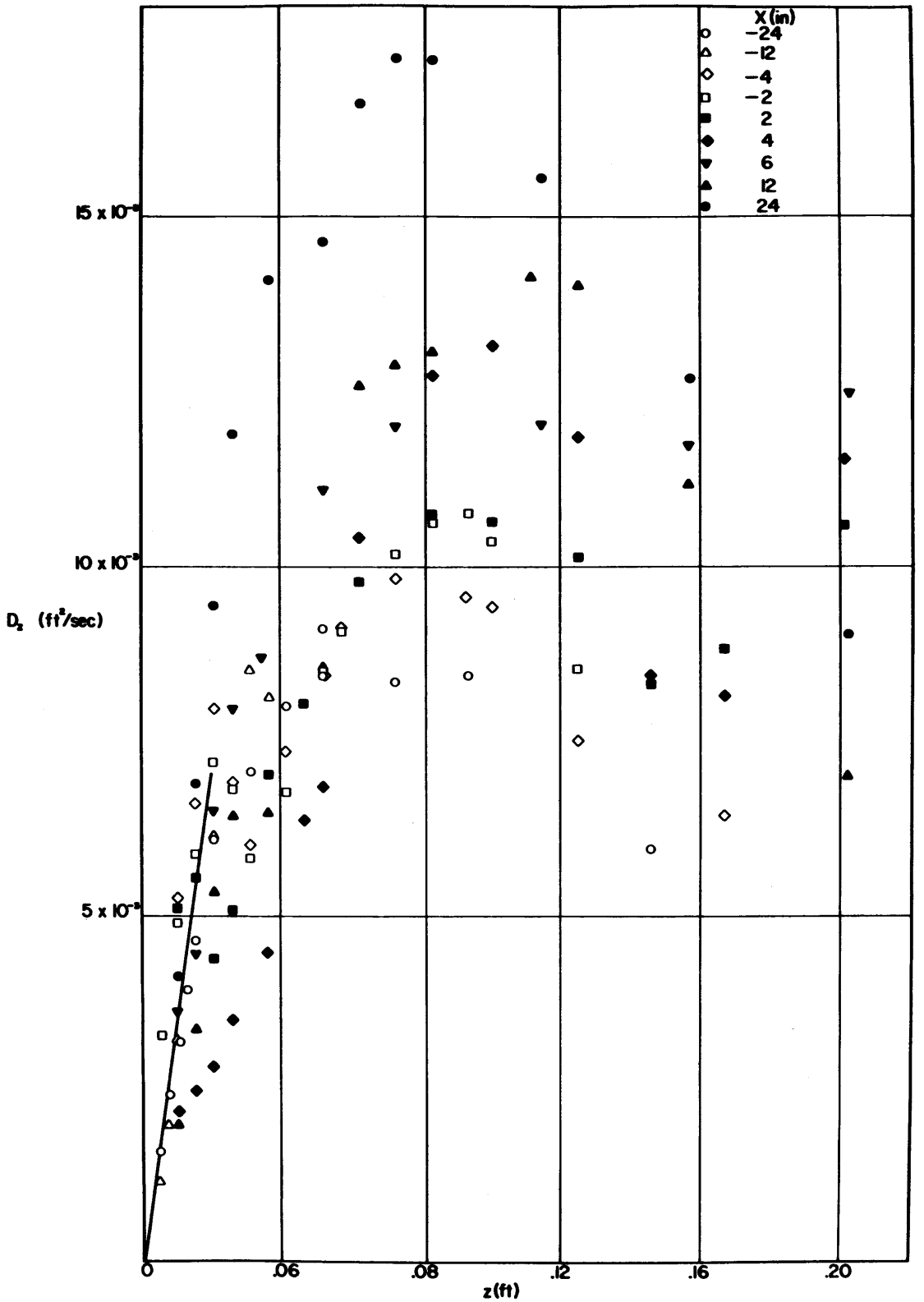

Figure 32. Distributions of the vertical turbulent diffusivity for Case I.

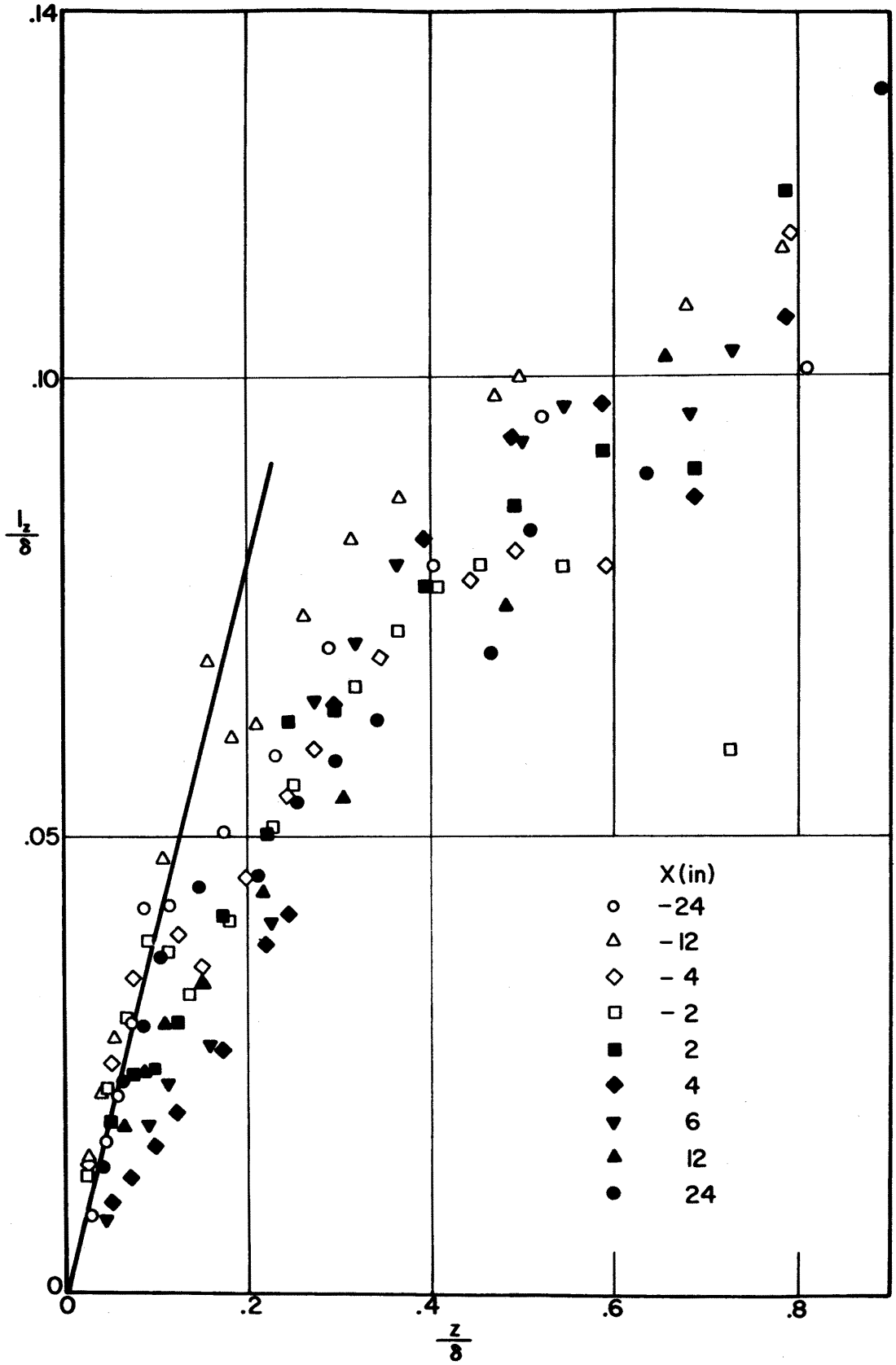

Figure 33. Distributions of the mixing length for Case I.

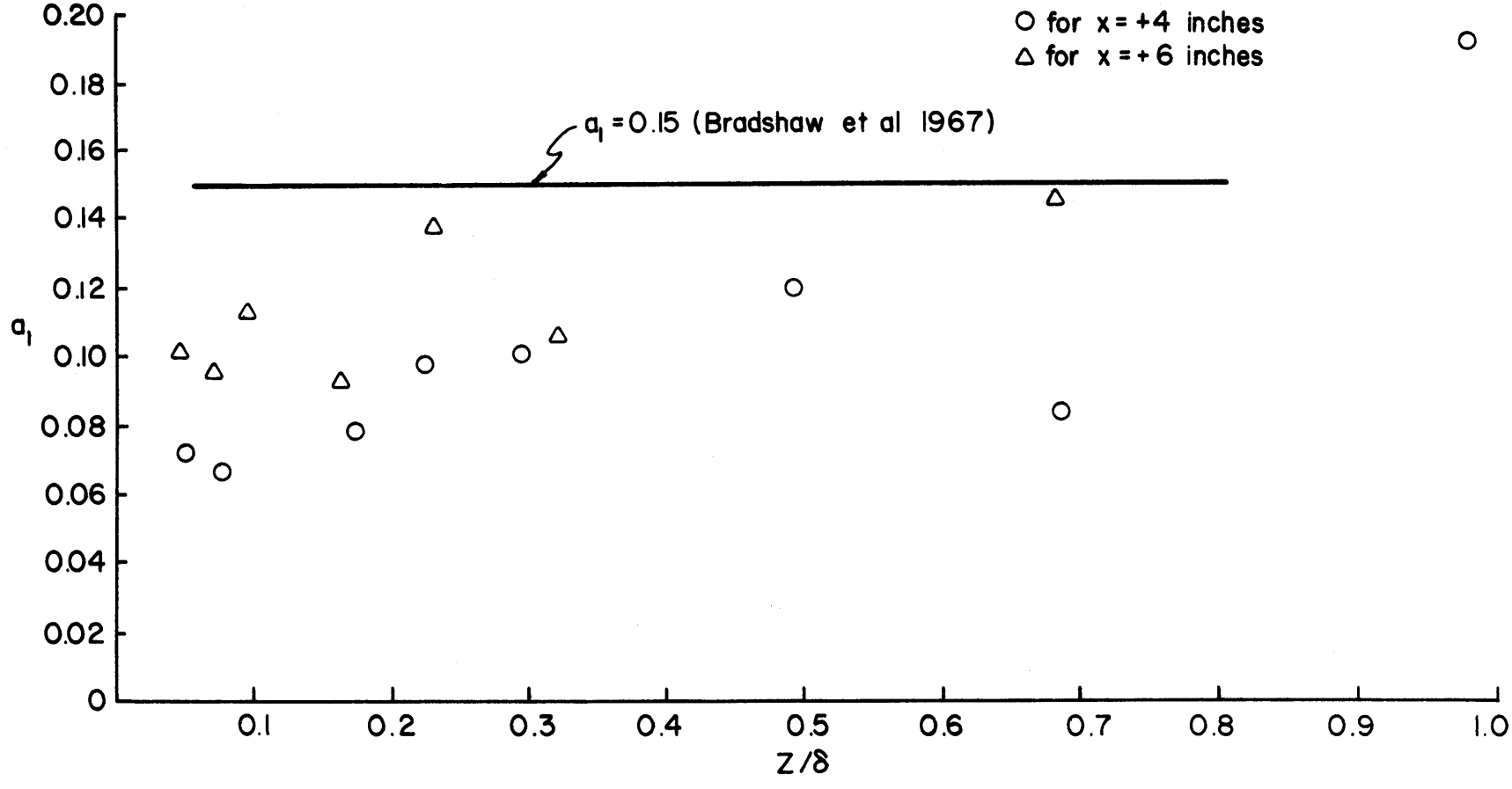

Figure 34. Distributions of $a_1 = \frac{\tau}{\rho \overline{q^2}}$ at x=4 in. and x=6 in. for Case I.

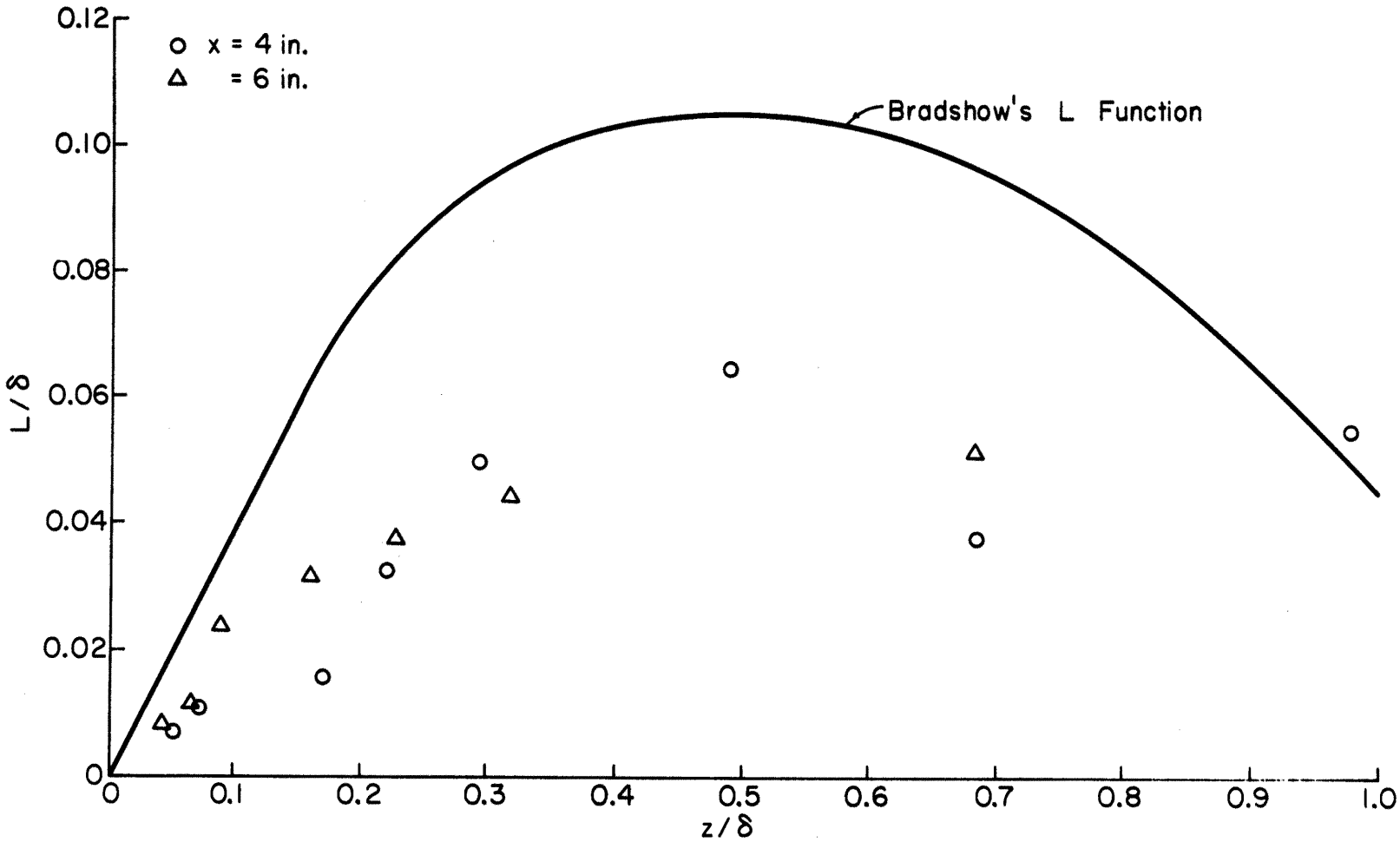

Figure 35. Non-dimensional distributions of $L=\frac{(\tau/\rho)^{3/2}}{\xi}$ at x=4 in. and x=6 in. for Case I.

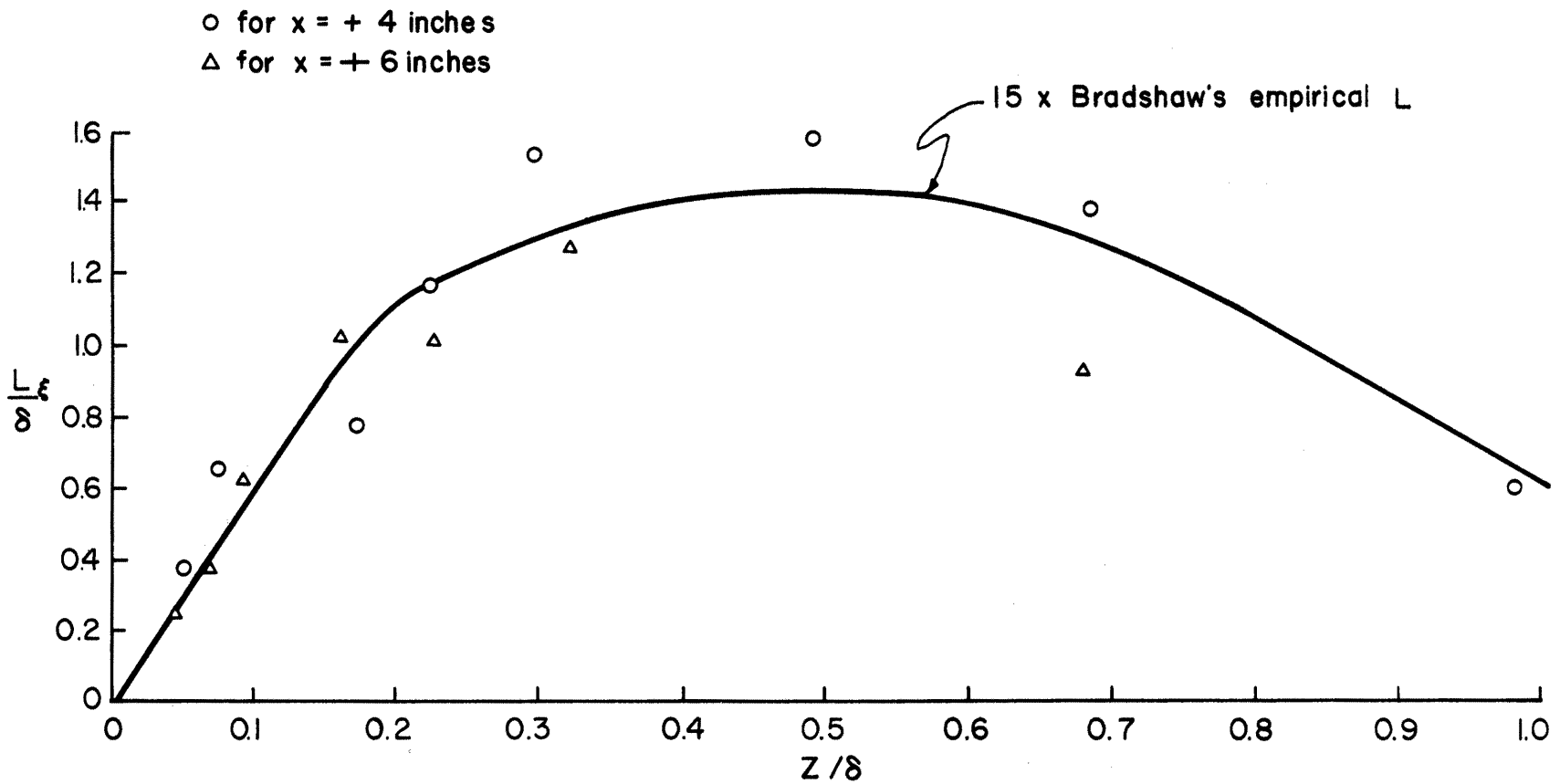

Figure 36. Non-dimensional distributions of $L_\xi = \frac{(\overline{q^2})^{3/2}}{\xi}$ at x=4 in. and x=6 in. for Case I.

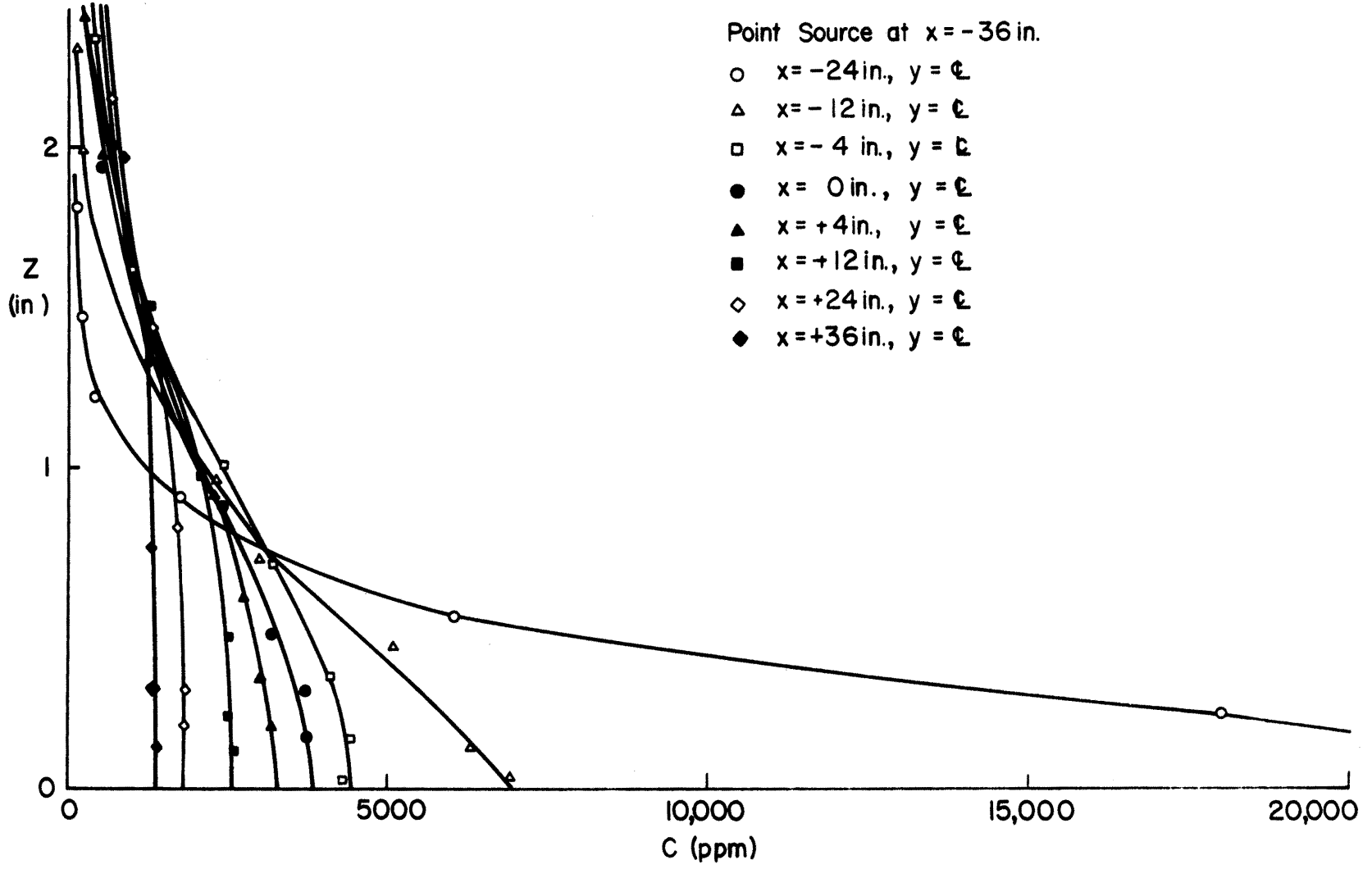

Figure 37. Typical profiles of the vertical mass concentration for Case I.

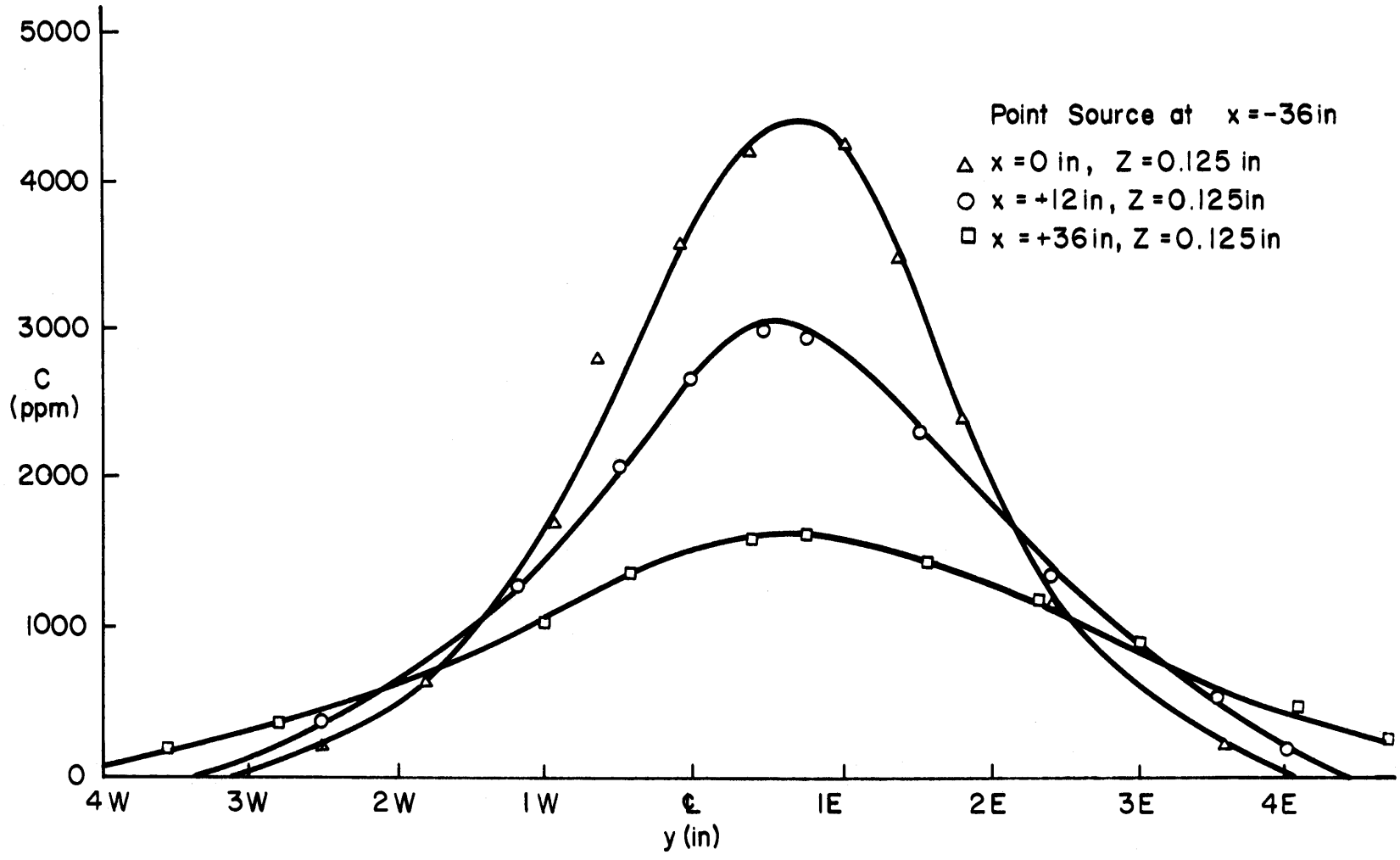

Figure 38. Typical profiles of the horizontal mass concentration for Case I.

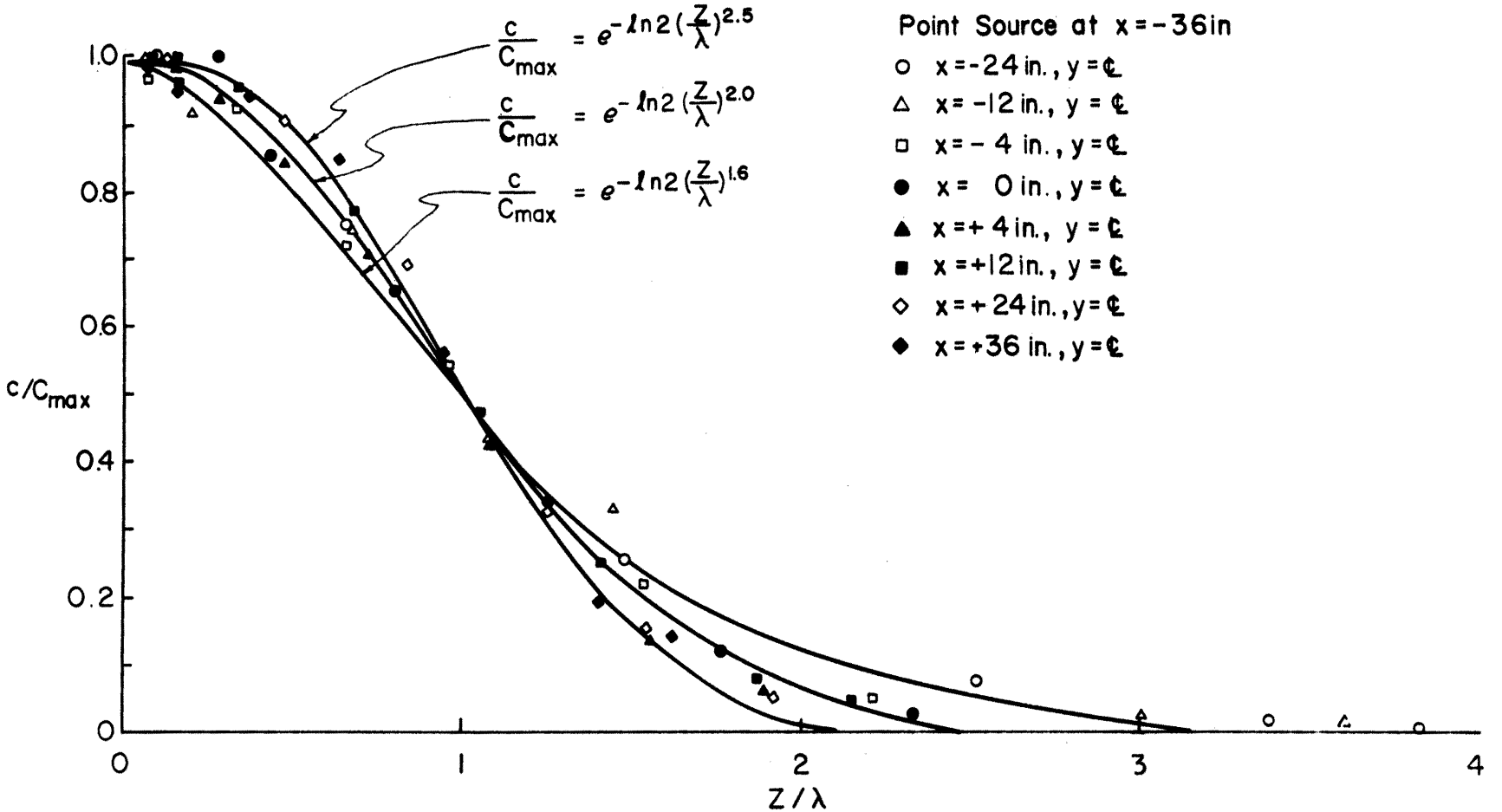

Figure 39. Non-dimensional plot of the vertical concentration profiles.

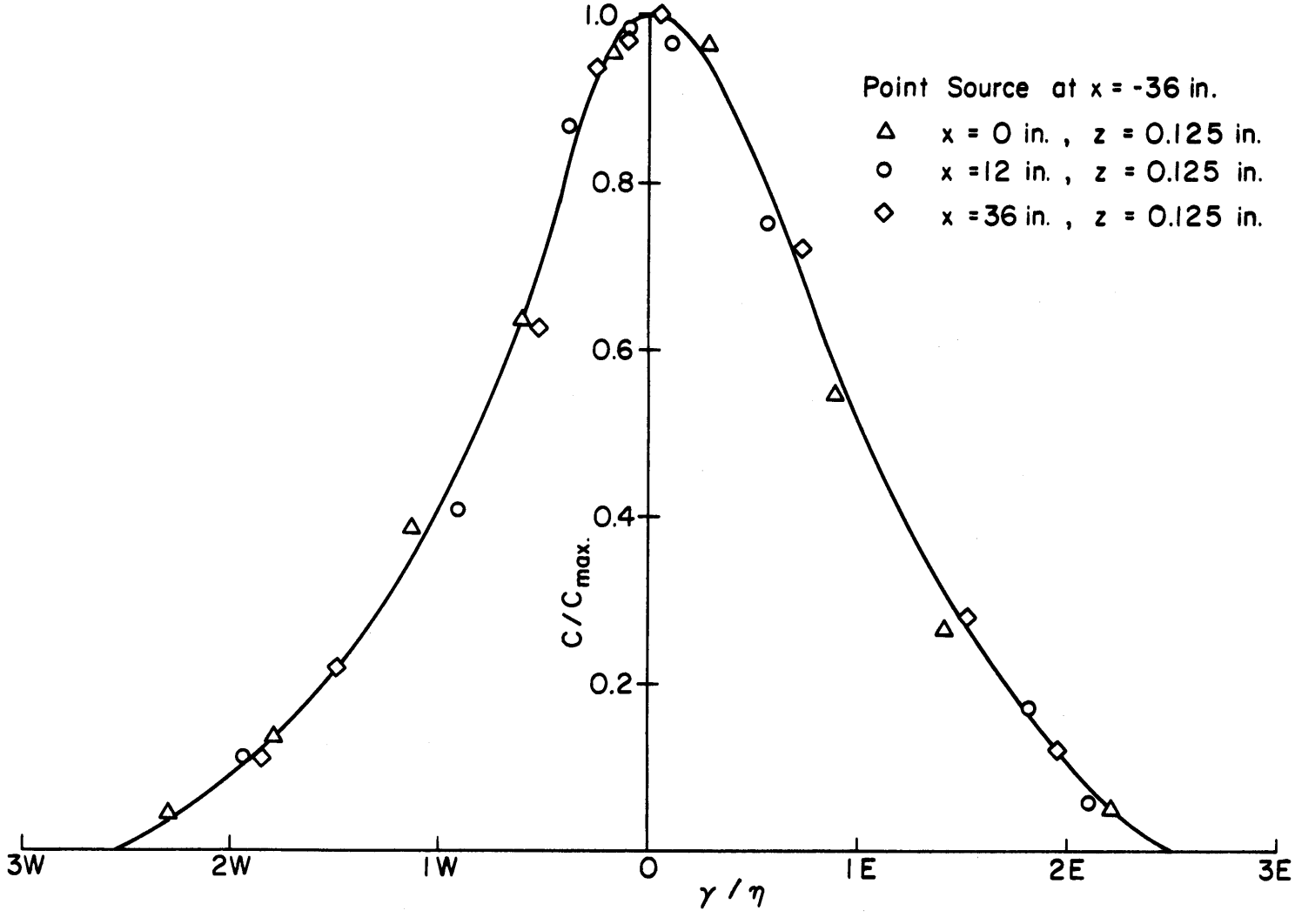

Figure 40. Non-dimensional plot of the horizontal concentration profiles.

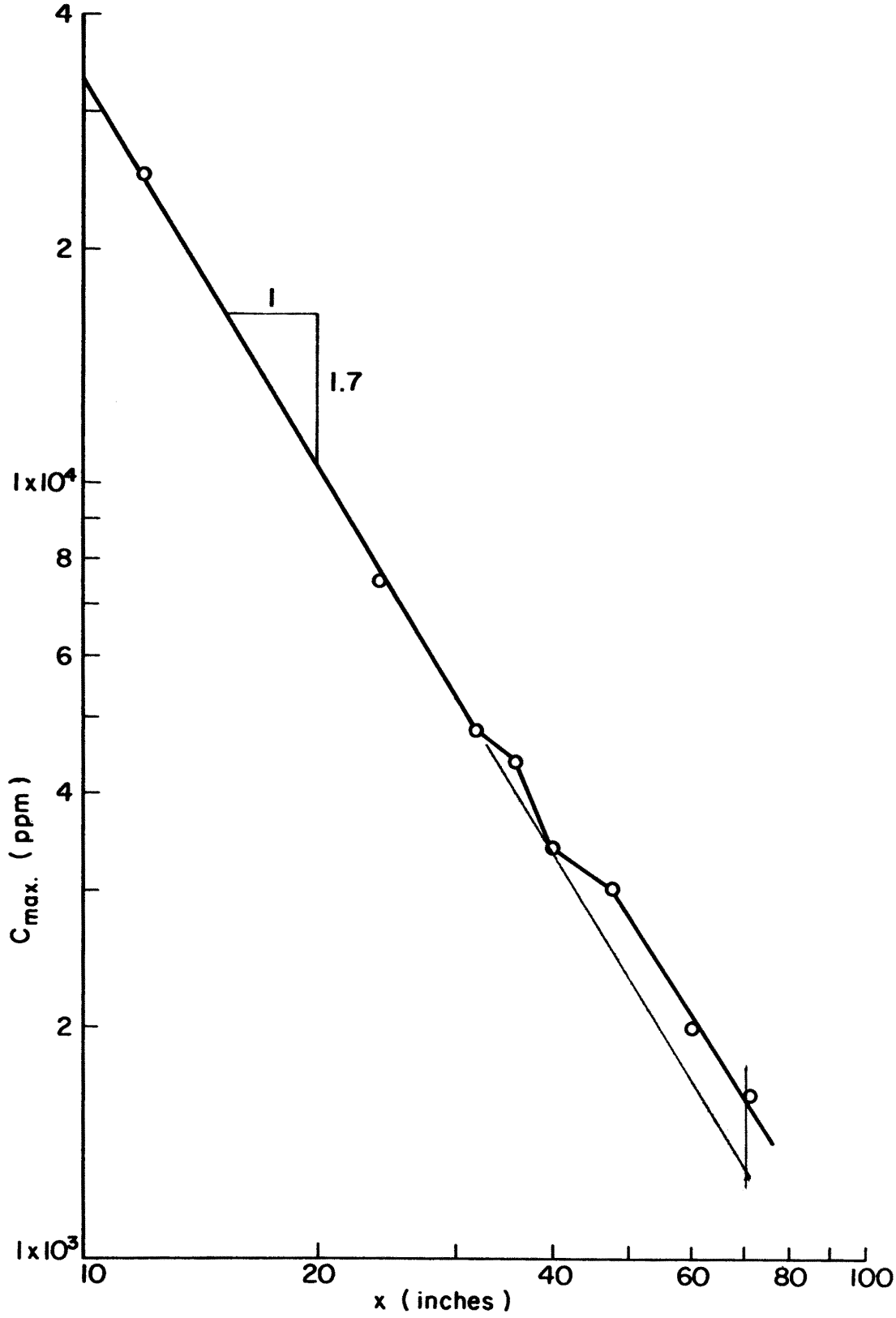

Figure 41. Decrease of C_{max} with x for Case I.

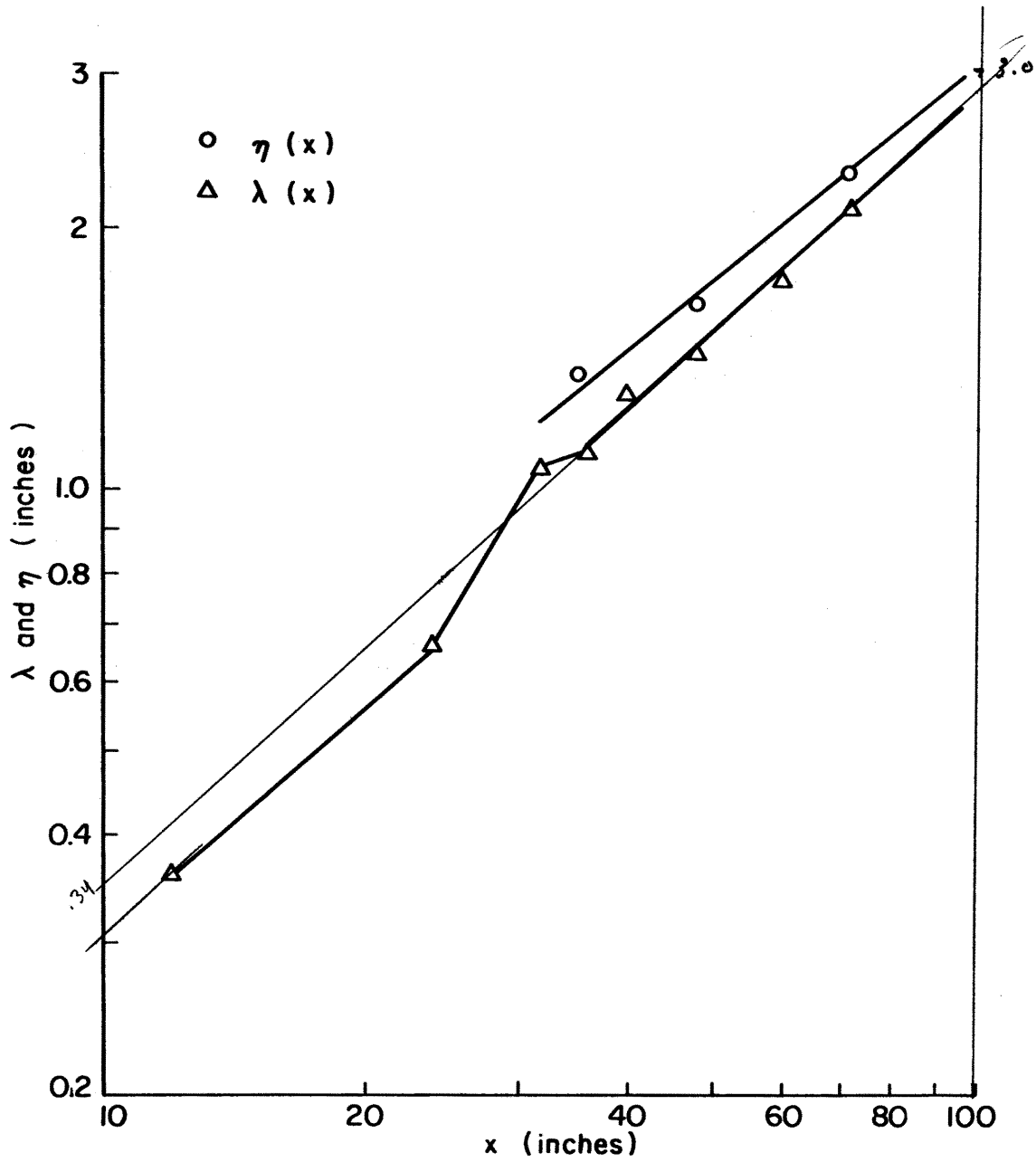

Figure 42. Growth of λ and η with x for Case I.

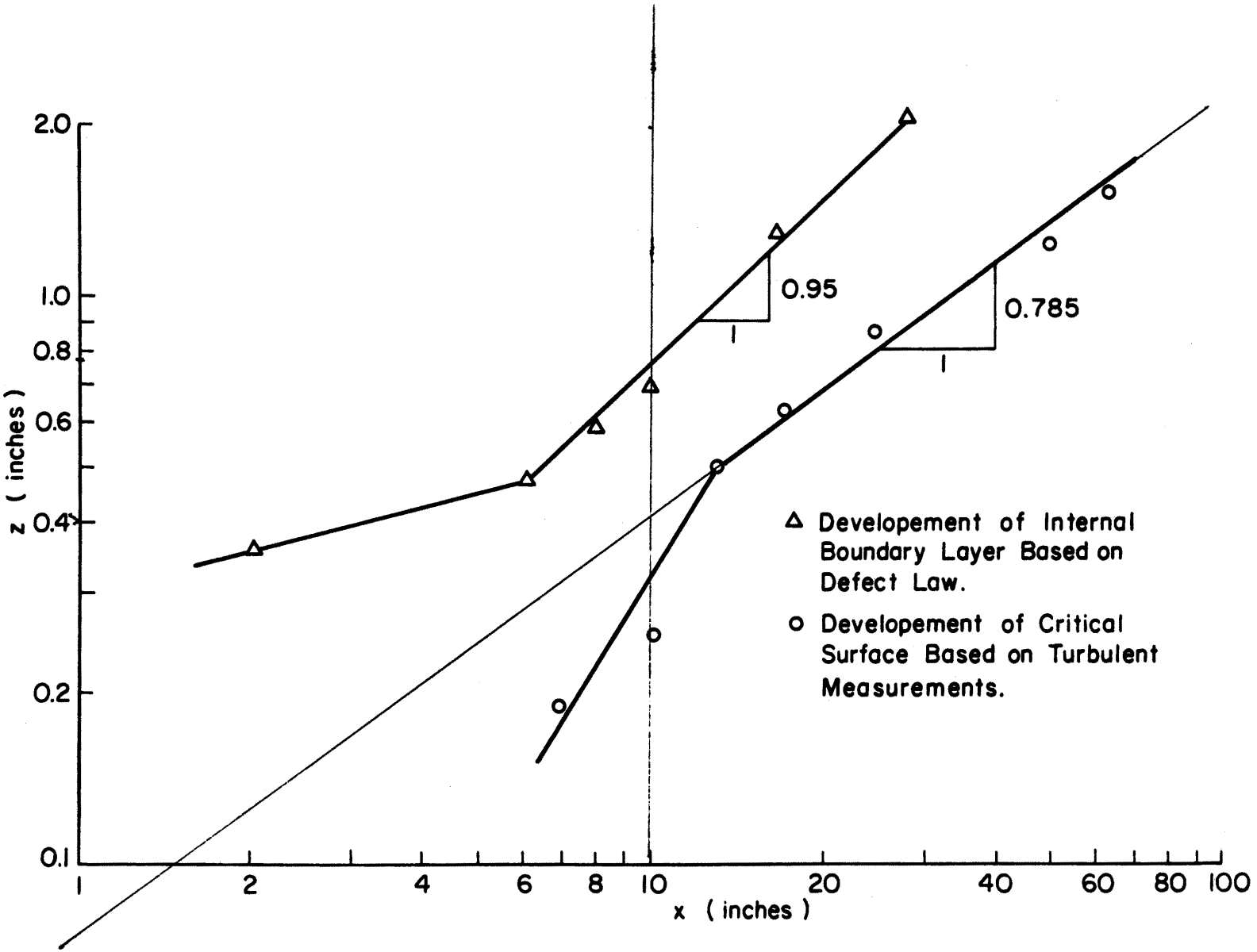

Figure 43. Growth of the surface of the internal boundary layer, compared with that of the critical surface velocity.

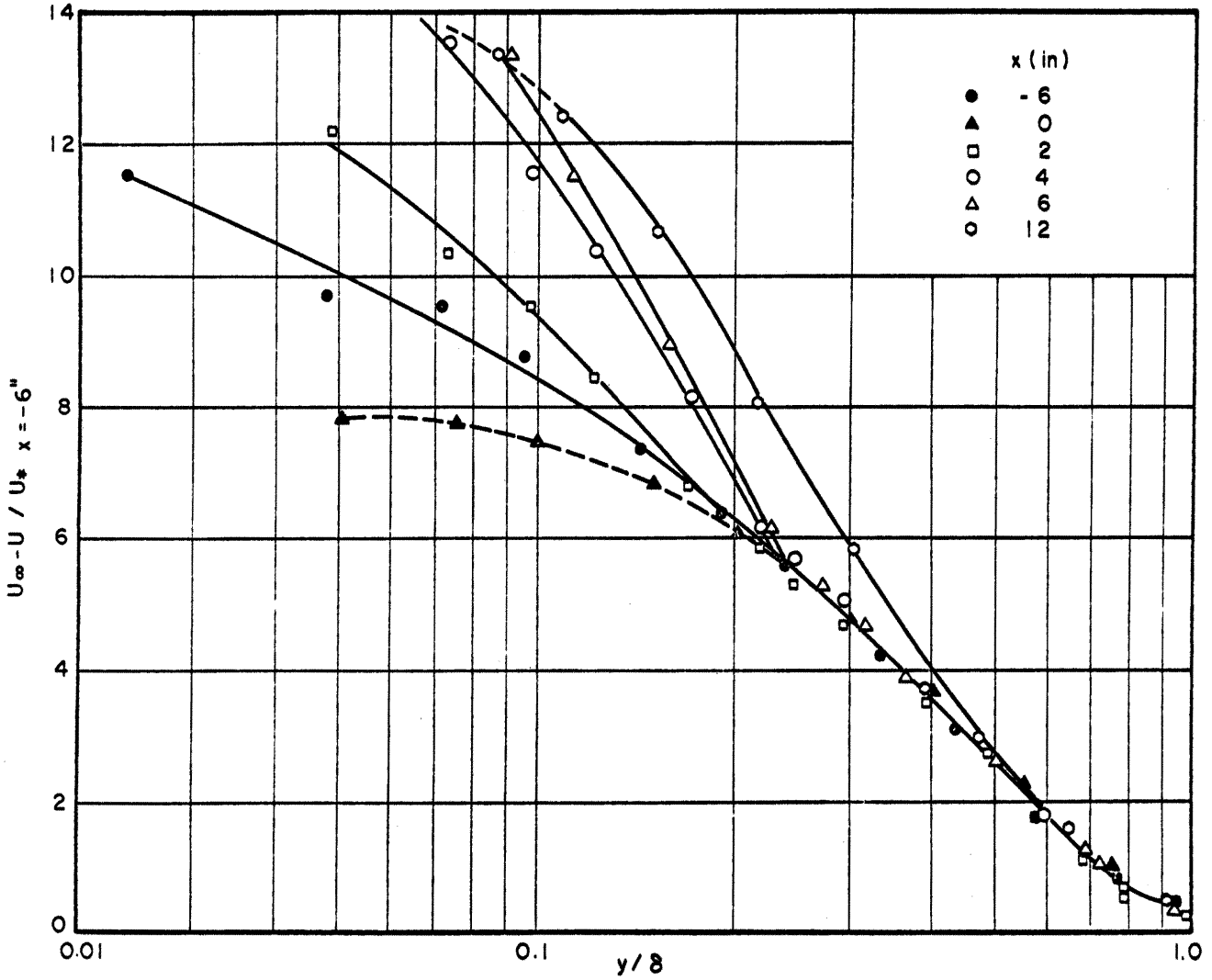

Figure 44. Non-dimensional plot of the defect law for Case. I.

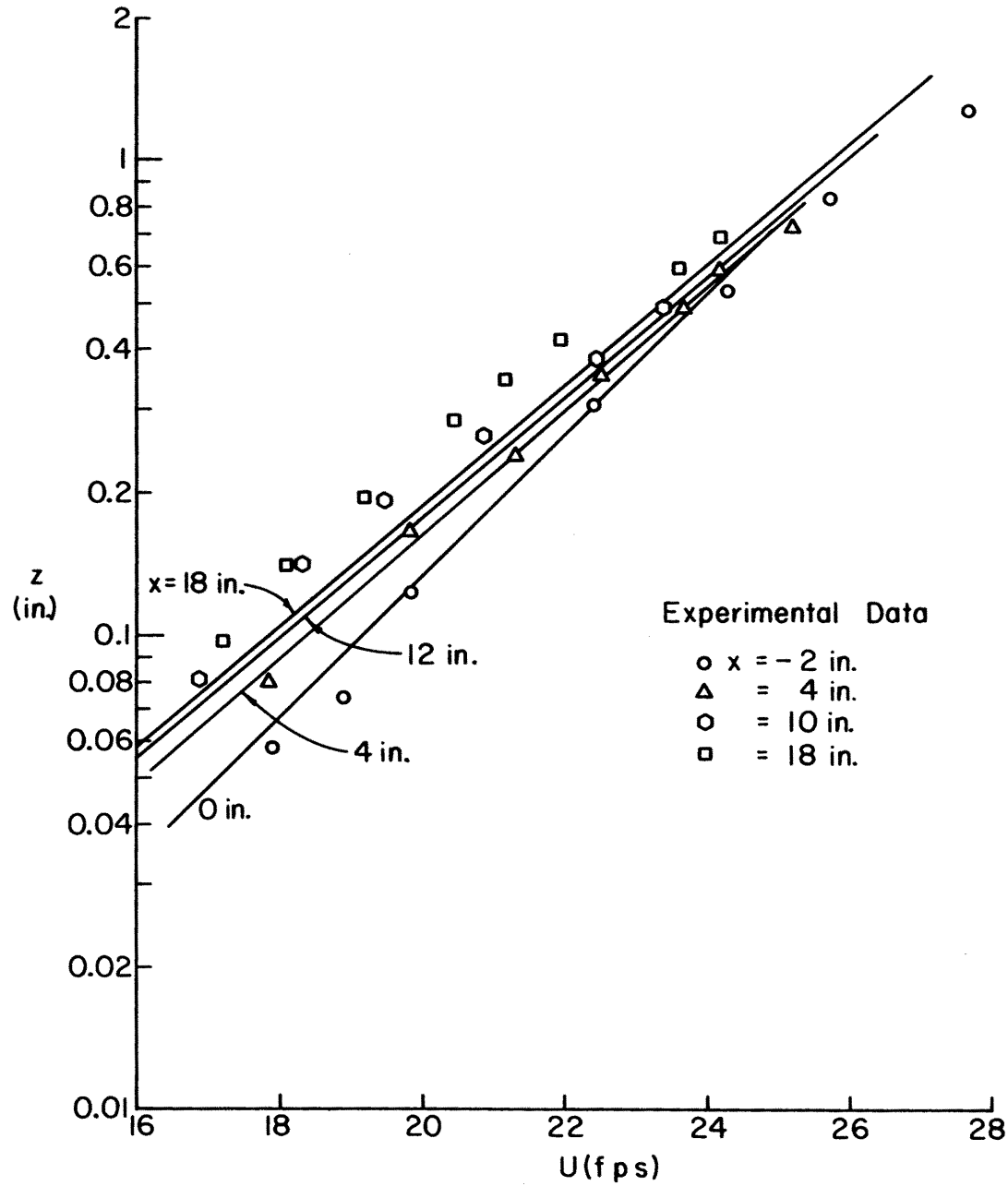

Figure 45. Mean velocity distributions for Case I compared with Nickerson's model.

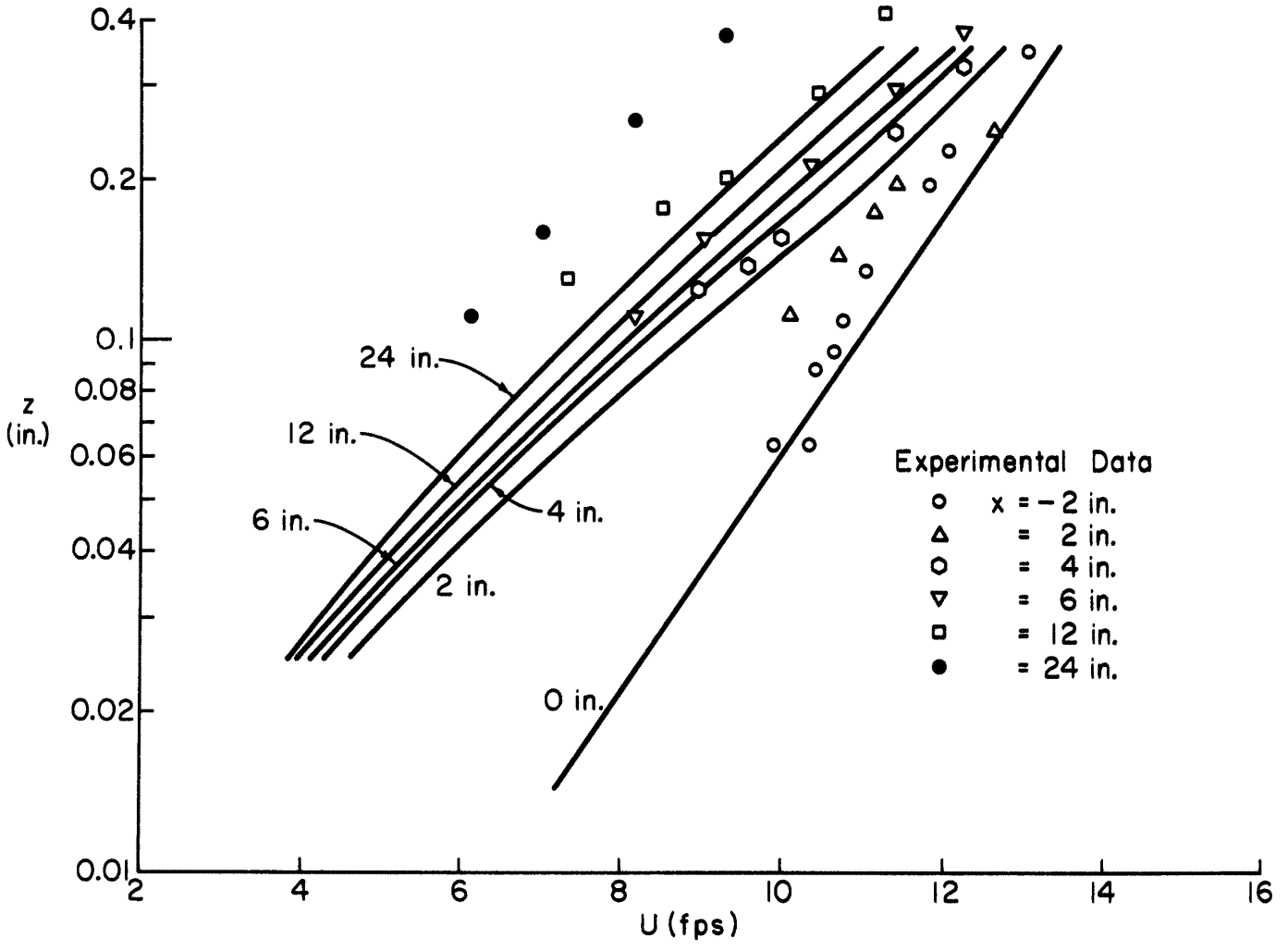

Figure 46. Mean velocity distributions for Case II compared with Nickerson's model.

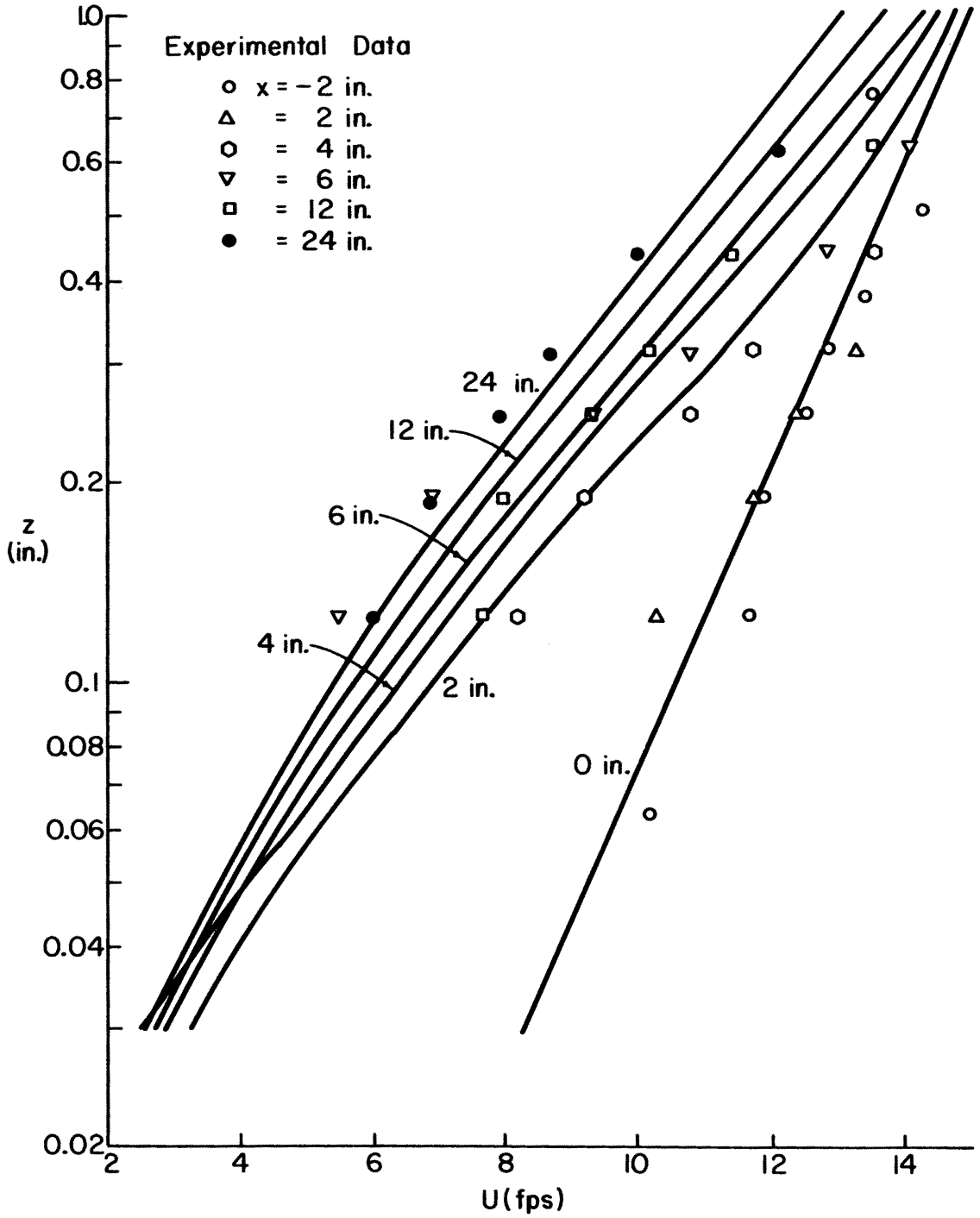

Figure 47. Mean velocity distributions for Case III compared with Nickerson's model

Security Classification

DOCUMENT CONTROL DATA - R&D

(Security classification of title, body of abstract and indexing annotation must be entered when the overall report is classified)

1. ORIGINATING ACTIVITY *(Corporate author)*
Fluid Dynamics & Diffusion Laboratory
College of Engineering, Colorado State University
Fort Collins, Colorado 80521

2a. REPORT SECURITY CLASSIFICATION
Unclassified

2b. GROUP

3. REPORT TITLE

Air Flow Over Roughness Discontinuity

4. DESCRIPTIVE NOTES *(Type of report and inclusive dates)*
Technical Report

5. AUTHOR(S) *(Last name, first name, initial)*
Yeh, Fei-Fan, and E. C. Nickerson

6. REPORT DATE
July 1970

7a. TOTAL NO. OF PAGES
139

7b. NO. OF REFS
53

8a. CONTRACT OR GRANT NO.
N00014-68-A-0493

b. PROJECT NO.
NR 062-414/6-6-68(Code 438)

c.

d.

9a. ORIGINATOR'S REPORT NUMBER(S)
CER70-71FFY-ECN6

9b. OTHER REPORT NO(S) *(Any other numbers that may be assigned this report)*
THEMIS TECHNICAL REPORT NO. 8

10. AVAILABILITY/LIMITATION NOTICES
Distribution of this report is unlimited

11. SUPPLEMENTARY NOTES

12. SPONSORING MILITARY ACTIVITY
Office of Naval Research
U. S. Department of Defense
Washington, D.C.

13. ABSTRACT

Measurements of mean velocity, mean-square turbulent velocity, turbulent shear stress, one-dimensional spectrum, and mass concentration distributions following a step increase in surface roughness of a wind-tunnel boundary-layer flow are presented. The mean velocity distributions agree well with Nickerson's (1968) numerical calculations for a small roughness change. The mixing-length distribution in the "transitory" region is not experimentally consistent with that established for fully-developed turbulent boundary layer. Turbulent intensity and shear stress are generated progressively towards the upper layer as one moves downstream from the roughness discontinuity. The high frequency end of the spectra in the "transitory" region can be exactly represented by the high frequency shape of the undisturbed turbulent boundary layer. Self-preserving mass concentration profiles are in general possible for both the vertical and horizontal distributions. The adjustment of the mean motion to the roughness change is more rapid than that of the turbulence.

DD FORM 1 JAN 64 1473

Unclassified
Security Classification

14. KEY WORDS	LINK A		LINK B		LINK C	
	ROLE	WT	ROLE	WT	ROLE	WT
Roughness Discontinuity Boundary Layer Mean Velocity Turbulent Velocity Shear Stress Transitory Turbulence						

INSTRUCTIONS

1. ORIGINATING ACTIVITY: Enter the name and address of the contractor, subcontractor, grantee, Department of Defense activity or other organization *(corporate author)* issuing the report.

2a. REPORT SECURITY CLASSIFICATION: Enter the overall security classification of the report. Indicate whether "Restricted Data" is included. Marking is to be in accordance with appropriate security regulations.

2b. GROUP: Automatic downgrading is specified in DoD Directive 5200.10 and Armed Forces Industrial Manual. Enter the group number. Also, when applicable, show that optional markings have been used for Group 3 and Group 4 as authorized.

3. REPORT TITLE: Enter the complete report title in all capital letters. Titles in all cases should be unclassified. If a meaningful title cannot be selected without classification, show title classification in all capitals in parenthesis immediately following the title.

4. DESCRIPTIVE NOTES: If appropriate, enter the type of report, e.g., interim, progress, summary, annual, or final. Give the inclusive dates when a specific reporting period is covered.

5. AUTHOR(S): Enter the name(s) of author(s) as shown on or in the report. Enter last name, first name, middle initial. If military, show rank and branch of service. The name of the principal author is an absolute minimum requirement.

6. REPORT DATE: Enter the date of the report as day, month, year; or month, year. If more than one date appears on the report, use date of publication.

7a. TOTAL NUMBER OF PAGES: The total page count should follow normal pagination procedures, i.e., enter the number of pages containing information.

7b. NUMBER OF REFERENCES: Enter the total number of references cited in the report.

8a. CONTRACT OR GRANT NUMBER: If appropriate, enter the applicable number of the contract or grant under which the report was written.

8b, 8c, & 8d. PROJECT NUMBER: Enter the appropriate military department identification, such as project number, subproject number, system numbers, task number, etc.

9a. ORIGINATOR'S REPORT NUMBER(S): Enter the official report number by which the document will be identified and controlled by the originating activity. This number must be unique to this report.

9b. OTHER REPORT NUMBER(S): If the report has been assigned any other report numbers *(either by the originator or by the sponsor)*, also enter this number(s).

10. AVAILABILITY/LIMITATION NOTICES: Enter any limitations on further dissemination of the report, other than those imposed by security classification, using standard statements such as:

(1) "Qualified requesters may obtain copies of this report from DDC."

(2) "Foreign announcement and dissemination of this report by DDC is not authorized."

(3) "U. S. Government agencies may obtain copies of this report directly from DDC. Other qualified DDC users shall request through _____."

(4) "U. S. military agencies may obtain copies of this report directly from DDC. Other qualified users shall request through _____."

(5) "All distribution of this report is controlled. Qualified DDC users shall request through _____."

If the report has been furnished to the Office of Technical Services, Department of Commerce, for sale to the public, indicate this fact and enter the price, if known.

11. SUPPLEMENTARY NOTES: Use for additional explanatory notes.

12. SPONSORING MILITARY ACTIVITY: Enter the name of the departmental project office or laboratory sponsoring *(paying for)* the research and development. Include address.

13. ABSTRACT: Enter an abstract giving a brief and factual summary of the document indicative of the report, even though it may also appear elsewhere in the body of the technical report. If additional space is required, a continuation sheet shall be attached.

It is highly desirable that the abstract of classified reports be unclassified. Each paragraph of the abstract shall end with an indication of the military security classification of the information in the paragraph, represented as *(TS)*, *(S)*, *(C)*, or *(U)*.

There is no limitation on the length of the abstract. However, the suggested length is from 150 to 225 words.

14. KEY WORDS: Key words are technically meaningful terms or short phrases that characterize a report and may be used as index entries for cataloging the report. Key words must be selected so that no security classification is required. Identifiers, such as equipment model designation, trade name, military project code name, geographic location, may be used as key words but will be followed by an indication of technical context. The assignment of links, rules, and weights is optional.

February 1969

APPROVED DISTRIBUTION LIST FOR UNCLASSIFIED TECHNICAL
REPORTS ISSUED UNDER CONTRACT N00014-68-A-0493-0001
NR 062-414

Technical Library, Building 313
Aberdeen Proving Ground
Aberdeen, Maryland 21005

Dr. F. D. Bennett
Exterior Ballistics Laboratory
Ballistics Research Laboratories
Aberdeen Proving Ground
Aberdeen, Maryland 21005

Mr. C. C. Hudson
Sandia Corporation
Sandia Base
Albuquerque, New Mexico 87115

Defense Documentation Center
Cameron Station
Alexandria, Virginia 22314 (20)

Professor Bruce Johnson
Engineering Department
Naval Academy
Annapolis, Maryland 21402

Library
Naval Academy
Annapolis, Maryland 21402

Professor W. W. Willmarth
Department of Aerospace Engineering
University of Michigan
Ann Arbor, Michigan 48108

Professor A. Kuethe
Department of Aeronautical Engineering
University of Michigan
Ann Arbor, Michigan 48108

AFOSR (SREM)
1400 Wilson Boulevard
Arlington, Virginia 22209

Dr. J. Menkes
Institute for Defense Analyses
400 Army-Navy Drive
Arlington, Virginia 22204

M. J. Thompson
Defense Research Laboratory
University of Texas
P. O. Box 8029
Austin, Texas 78712

Library
Aerojet-General Corporation
6352 N. Irwindale Avenue
Azusa, California 91702

Professor S. Corrsin
Department of Mechanics
Johns Hopkins University
Baltimore, Maryland 21218

Professor M. V. Morkovin
Aeronautics Building
Johns Hopkins University
Baltimore, Maryland 21218

Professor O. M. Phillips
Division of Mechanical Engineering
Institute for Cooperative Research
Johns Hopkins University
Baltimore, Maryland 21218

Geophysical Research Library
Air Force Cambridge Research Center
Bedford, Massachusetts 01731

Librarian
Department of Naval Architecture
University of California
Berkeley, California 94720

Professor Paul Lieber
Department of Mechanical Engineering
University of California
Berkeley, California 94720

Professor J. Johnson
412 Hesse Hall
University of California
Berkeley, California 94720

Professor A. K. Oppenheim
Division of Mechanical Engineering
University of California
Berkeley, California 94720

Professor M. Holt
Division of Aeronautical Sciences
University of California
Berkeley, California 94720

Dr. L. Talbot
Department of Engineering
Berkeley, California 94720

Professor R. J. Emrich
Department of Physics
Lehigh University
Bethlehem, Pennsylvania 18015

Engineering Library
Plant 25
Grumman Aircraft Engineering Corporation
Bethpage, Long Island, New York 11714

Mr. Eugene F. Baird
Chief of Dynamic Analysis
Grumman Aircraft Engineering Corporation
Bethpage, Long Island, New York 11714

Library
Naval Weapons Center
China Lake, California 93555

Library MS 60-3
NASA Lewis Research Center
21000 Brookpark Road
Cleveland, Ohio 44133

Professor J. M. Burgers
Institute for Fluid Dynamics and
Applied Mathematics
University of Maryland
College Park, Maryland 20742

Professor J. R. Weske
Institute for Fluid Dynamics and
Applied Mathematics
University of Maryland
College Park, Maryland 20742

Professor Pai
Institute for Fluid Dynamics and
Applied Mathematics
University of Maryland
College Park, Maryland 20742

NASA Scientific and Technical
Information Facility
Acquisitions Branch (S-AK/DL)
P. O. Box 33
College Park, Maryland 20740

Professor Loren E. Bollinger
The Ohio State University
Box 3113 - University Station
Columbus, Ohio 43210

Professor G. L. von Eschen
Department of Aeronautical and
Astronautical Engineering
Ohio State University
Columbus, Ohio 43210

Computations and Analysis Laboratory
Naval Weapons Laboratory
Dahlgren, Virginia 22448

Technical Library
Naval Weapons Laboratory
Dahlgren, Virginia 22418

Dr. J. Harkness
LTV Research Center
Ling-Temco-Vought Aerospace Corporation
P. O. Box 5907
Dallas, Texas 75222

Mr. Adolf Egli
Ford Motor Company
Engineering and Research Staff
P. O. Box 2053
Dearborn, Michigan 48123

School of Applied Mathematics
Indiana University
Bloomington, Indiana 47401

Commander
Boston Naval Shipyard
Boston, Massachusetts 02129

Director
Office of Naval Research Branch Office
495 Summer Street
Boston, Massachusetts 02210

Professor M. S. Uberoi
Department of Aeronautical Engineering
University of Colorado
Boulder, Colorado 80303

Technical Library
Naval Applied Science Laboratory
Building 1, Code 222
Flushing & Washington Avenues
Brooklyn, New York 11251

Professor J. J. Foody
Chairman, Engineering Department
State University of New York
Maritime College
Bronx, New York 10465

Mr. F. Dell'Amico
Cornell Aeronautical Laboratory
P. O. Box 235
Buffalo, New York 14221

Professor G. Birkhoff
Department of Mathematics
Harvard University
Cambridge, Massachusetts 02138

Professor B. Budiansky
Department of Mechanical Engineering
School of Applied Sciences
Harvard University
Cambridge, Massachusetts 02138

Dr. Ira Dyer
Bolt, Beranek and Newman, Inc.
50 Moulton Street
Cambridge, Massachusetts 02138

Department of Naval Architecture
and Marine Engineering
Massachusetts Institute of Technology
Cambridge, Massachusetts 02139

Professor Patrick Leehey
Department of Naval Architecture and
Marine Engineering
Massachusetts Institute of Technology
Cambridge, Massachusetts 02139

Professor E. Mollo-Christensen
Department of Aeronautics and Astronautics
Massachusetts Institute of Technology
Cambridge, Massachusetts 02139

Professor A. T. Ippen
Department of Civil Engineering
Massachusetts Institute of Technology
Cambridge, Massachusetts 02139

Professor C. C. Lin
Department of Mathematics
Massachusetts Institute of Technology
Cambridge, Massachusetts 02139

Professor H. C. Hottel
Department of Chemical Engineering
Massachusetts Institute of Technology
Cambridge, Massachusetts 02139

Commanding Officer
NROTC and Naval Administrative Unit
Massachusetts Institute of Technology
Cambridge, Massachusetts 02139

Professor R. F. Probstein
Department of Mechanical Engineering
Massachusetts Institute of Technology
Cambridge, Massachusetts 02139

Technical Library
Webb Institute of Naval Architecture
Glen Cove, Long Island, New York 11542

Library, MS185
NASA Langley Research Center
Langley Station
Hampton, Virginia 23365

Dr. B. N. Pridmore Brown
Northrop Corporation
Norair-Division
Hawthorne, California 90250

Dr. J. P. Breslin
Davidson Laboratory
Stevens Institute of Technology
Hoboken, New Jersey 07030

Mr. D. Savitsky
Davidson Laboratory
Stevens Institute of Technology
Hoboken, New Jersey 07030

Mr. S. Tsakonas
Davidson Laboratory
Stevens Institute of Technology
Hoboken, New Jersey 07030

Professor J. F. Kennedy, Director
Iowa Institute of Hydraulic Research
University of Iowa
Iowa City, Iowa 52240

Professor L. Landweber
Iowa Institute of Hydraulic Research
University of Iowa
Iowa City, Iowa 52240

Professor John R. Glover
Iowa Institute of Hydraulic Research
University of Iowa
Iowa City, Iowa 52240

Professor E. L. Resler
Graduate School of Aeronautical Engineering
Cornell University
Ithaca, New York 14851

Technical Library
Scripps Institution of Oceanography
University of California
La Jolla, California 92037

Professor S. R. Keim
University of California
Institute of Marine Resources
P. O. Box 109
La Jolla, California 92038

Dr. B. Sternlicht
Mechanical Technology Incorporated
968 Albany-Shaker Road
Latham, New York 12110

Mr. P. Eisenberg
HYDRONAUTICS, Incorporated
Pindell School Road
Howard County, Laurel, Maryland 20810

Technical Library
Charleston Naval Shipyard
Naval Base
Charleston, South Carolina 29408

Director
Office of Naval Research Branch Office
219 South Dearborn Street
Chicago, Illinois 60604

Technical Library
Puget Sound Naval Shipyard
Bremerton, Washington 98314

Technical Library
Annapolis Division
Naval Ship Research & Development Center
Annapolis, Maryland 21402

Code ESD-AROD
Army Research Office
Box CM, Duke Station
Durham, North Carolina 27706

Professor Ali Bulent Cambel
Chairman, Department of Mechanical Engineering
Northwestern University
Evanston, Illinois 60201

Professor A. Charnes
The Technological Institute
Northwestern University
Evanston, Illinois 60201

Barbara Spence Technical Library
AVCO-Everett Research Laboratory
2385 Revere Beach Parkway
Everett, Massachusetts 02149

Dr. Martin Bloom
Director of Dynamics Research
Department of Aerospace Engineering and Applied Mechanics
Polytechnic Institute of Brooklyn-Graduate Center
Route 110
Farmingdale, New York 11201

Professor J. E. Cermak
Professor-in-Charge, Fluid Mechanics Program
College of Engineering
Colorado State University
Fort Collins, Colorado 80521

Mr. Seymour Edelberg
Lincoln Laboratory
Massachusetts Institute of Technology
P. O. Box 73
Lexington, Massachusetts 02173

Technical Library
Long Beach Naval Shipyard
Long Beach, California 90801

Professor A. F. Charwat
Department of Engineering
University of California
Los Angeles, California 90024

Professor R. W. Leonard
University of California
Los Angeles, California 90024

Professor John Laufer
Department of Aerospace Engineering
University Park
University of California
Los Angeles, California 90007

Professor J. F. Ripkin
St. Anthony Falls Hydraulic Laboratory
University of Minnesota
Minneapolis, Minnesota 55414

Lorenz G. Straub Library
St. Anthony Falls Hydraulic Laboratory
University of Minnesota
Minneapolis, Minnesota 55414

Library
Naval Postgraduate School
Monterey, California 93940

Professor A. B. Metzner
Department of Chemical Engineering
University of Delaware
Newark, Delaware 19711

Technical Library
Navy Underwater Sound Laboratory
Fort Trumbull
New London, Connecticut 06320

Technical Library
Naval Underwater Weapons Research and Engineering Station
Newport, Rhode Island 02840

Professor W. J. Pierson, Jr.
Department of Meteorology and Oceanography
New York University
University Heights
New York, New York 10405

Professor J. J. Stoker
Courant Institute of Mathematical Sciences
New York University
251 Mercer Street
New York, New York 10003

Engineering Societies Library
345 East 47th Street
New York, New York 10017

Office of Naval Research
New York Area Office
207 W. 24th Street
New York, New York 10011

Commanding Officer
Office of Naval Research Branch Office
Box 39, FPO, New York 09510 (25)

Professor A. G. Strandhagen
Department of Engineering Mechanics
University of Notre Dame
Notre Dame, Indiana 46556

Miss O. M. Leach, Librarian
National Research Council
Aeronautical Library
Montreal Road
Ottawa 7, Canada

Lockheed Missiles and Space Company
Technical Information Center
3251 Hanover Street
Palo Alto, California 94301

Professor M. S. Plesset
Engineering Science Department
California Institute of Technology
Pasadena, California 91109

Professor H. W. Liepmann
Department of Aeronautics
California Institute of Technology
Pasadena, California 91109

Dr. Jack W. Hoyt (Code P2501)
Associate Head, Ocean Technology Department
Naval Undersea Warfare Center
3202 E. Foothill Blvd.
Pasadena, California 91107

Dr. F. R. Hama
Jet Propulsion Laboratory
4800 Oak Grove Drive
Pasadena, California 91103

Professor T. Y. Wu
Division of Engineering
California Institute of Technology
Pasadena, California 91109

Professor A. J. Acosta
Department of Mechanical Engineering
California Institute of Technology
Pasadena, California 91109

Director
Office of Naval Research Branch Office
1030 E. Green Street
Pasadena, California 91101

Professor F. Zwicky
Department of Physics
California Institute of Technology
Pasadena, California 91109

Dr. E. E. Sechler
Executive Officer for Aeronautics
California Institute of Technology
Pasadena, California 91109

Dr. R. H. Kraichnan
Dublin, New Hampshire 03444

Technical Library (Code 249b)
Philadelphia Naval Shipyard
Philadelphia, Pennsylvania 19112

Dr. Sinclaire M. Scala
Space Sciences Laboratory
General Electric Company
P. O. Box 8555
Philadelphia, Pennsylvania 19101

Dr. Paul Kaplan
Oceanics, Inc.
Technical Industrial Park
Plainview, L. I., New York 11803

Technical Library
Naval Missile Center
Point Mugu, California 93041

Technical Library
Portsmouth Naval Shipyard
Portsmouth, New Hampshire 03801

Technical Library
Norfolk Naval Shipyard
Portsmouth, Virginia 23709

Professor G. W. Duvall
Department of Physics
Washington State University
Pullman, Washington 99164

Chief, Document Section
Redstone Scientific Information Center
Army Missile Command
Redstone Arsenal, Alabama 35809

Professor M. Lessen, Head
Department of Mechanical Engineering
University of Rochester
College of Engineering, River
Campus Station
Rochester, New York 14627

Dr. H. N. Abramson
Southwest Research Institute
8500 Culebra Road
San Antonio, Texas 78228

Editor
Applied Mechanics Review
Southwest Research Institute
8500 Culebra Road
San Antonio, Texas 78206

Dr. S. L. Zieberg, Head
Gas Dynamics Section, Fluid Mechanics
Building B-1, Room 1320
Aerospace Corporation
San Bernardino, California 92402

Mr. Myles B. Berg
Aerospace Corporation
P. O. Box 1308
San Bernardino, California 92402

Mr. W. B. Barkley
General Dynamics Corporation
Electric Boat Division
Marine Technology Center, P. O. Box 911
San Diego, California 92112

Library (128-000)
CONVAIR - Division of General Dynamics
P. O. Box 12009
San Diego, California 92112

Technical Library
Pearl Harbor Naval Shipyard
Box 400, FPO, San Francisco 96610

Technical Library, Code H245C-3
Hunters Point Division
San Francisco Bay Naval Shipyard
San Francisco, California 94135

Office of Naval Research San Francisco
Area Office
1076 Mission Street
San Francisco, California 94103

Gail T. Flesher - 44
GM Defense Research Laboratory
Box T
Santa Barbara, California 93102

Library
The RAND Corporation
1700 Main Street
Santa Monica, California 90401

Dr. H. T. Nagamatsu
General Electric Company
Research and Development Center K-1
P. O. Box 8
Schenectady, New York 12301

Fenton Kennedy Document Library
The Johns Hopkins University
Applied Physics Laboratory
8621 Georgia Avenue
Silver Spring, Maryland 20910

Chief, Library Division
Naval Ordnance Laboratory
White Oak
Silver Spring, Maryland 20910

Dr. R. E. Wilson
Associate Technical Director
(Aeroballistics)
Naval Ordnance Laboratory
White Oak
Silver Spring, Maryland 20910

Aerophysics Division
Naval Ordnance Laboratory
White Oak
Silver Spring, Maryland 20910

Dr. A. E. Seigel
Naval Ordnance Laboratory
White Oak
Silver Spring, Maryland 20910

Dr. S. Kline
Mechanical Engineering 501 G
Stanford University
Stanford, California 94305

Engineering Library
Department 218, Building 101
McDonnel Aircraft Corporation
P. O. Box 516
St. Louis, Missouri 63166

Mr. R. W. Kermeen
Lockheed Missiles & Space Company
Department 57101, Building 150
Sunnyvale, California 94086

Professor S. Eskinazi
Department of Mechanical Engineering
Syracuse University
Syracuse, New York 13210

Professor J. Foa
Department of Aeronautical Engineering
Rensselaer Polytechnic Institute
Troy, New York 12180

Professor R. C. DiPrima
Department of Mathematics
Rensselaer Polytechnic Institute
Troy, New York 12180

Professor L. M. Milne-Thomson
Mathematics Department
University of Arizona
Tucson, Arizona 85721

Dr. E. J. Skudrzyk
Ordnance Research Laboratory
Pennsylvania State University
University Park, Pennsylvania 16801

Dr. M. Sevik
Ordnance Research Laboratory
Pennsylvania State University
University Park, Pennsylvania 16801

Dr. G. F. Wislicenus
Ordnance Research Laboratory
Pennsylvania State University
University Park, Pennsylvania 16801

Dr. A. S. Iberall, President
General Technical Services, Inc.
8794 West Chester Pike
Upper Darby, Pennsylvania 19082

Dr. J. M. Robertson
Department of theoretical and
Applied Mechanics
University of Illinois
Urbana, Illinois 61803

Shipyard Technical Library
Code 130L7, Building 746
San Francisco Bay Naval Shipyard
Vallejo, California 94592

Commander
Naval Ship Research and Development Center
Attn: Code 513 (1)
Code 901 (1)
Code 942 (1)
Code 01 (Dr. Powell) (1)
Code 042 (1)
Code 520 (1)
Code 800 (1)
Washington, D. C. 20007

Commander
Naval Ship System Command
Attn: Technical Library (2052) (1)
Washington, D. C. 20360

Director, Engineering Science Division
National Sciences Foundation
Washington, D. C. 20550

Chief of Naval Research
Department of the Navy
Attn: Code 438 (3)
Code 461 (1)
Code 463 (1)
Code 468 (1)
Code 421 (1)
Washington, D. C. 20360

Commander
Naval Air Systems Command
Department of the Navy
Attn: Code AIR 370 (1)
Code AIR 6042 (1)
Washington, D. C. 20360

Librarian Station 5-2
Coast Guard Headquarters
1300 E Street, N. W.
Washington, D. C. 20226

Division of Engineering
Maritime Administration
441 G Street, N. W.
Washington, D. C. 20235

Commander
Naval Oceanographic Office
Washington, D. C. 20390

Code 2027 (6)
Naval Research Laboratory
Washington, D. C. 20390

Science and Technology Division
Library of Congress
Washington, D. C. 20540

Commander
Naval Ordnance Systems Command
Attn: ORD 913 (Library) (1)
ORD 035 (1)
Washington, D. C. 20360

Library
National Bureau of Standards
Washington, D. C. 20234

Chief of Research and Development
Office of Chief of Staff
Department of the Army
The Pentagon, Washington, D. C. 20310

Dr. Frank Lane
General Applied Science Laboratory
Merrick and Stewart Avenues
Westbury, Long Island, New York 11590

Director
Woods Hole Oceanographic Institute
Woods Hole, Massachusetts 02543

Mr. W. J. Mykytow
AF Flight Dynamics Laboratory
Wright-Patterson Air Force Base
Ohio 45433

Dr. H. Cohen
IBM Research Center
P. O. Box 218
Yorktown Heights, New York 10598